Acoustic boundary value problems and their application to partial spherical microphone arrays

Hannes Pomberger

Institute of Electronic Music and Acoustics
University of Music and Performing Arts Graz, Austria

A thesis submitted for the degree of

Doktor der Naturwissenschaften

September 2017

Assesors:
Prof. Robert Höldrich (IEM, KUG)
Prof. Alois Sontacchi (IEM, KUG)

HANNES POMBERGER	0130905
(Name in Blockbuchstaben)	(Matrikelnummer)

Erklärung

Hiermit bestätige ich, dass mir der *Leitfaden für schriftliche Arbeiten an der KUG*

bekannt ist und ich diese Richtlinien eingehalten habe.

Graz, den …………………………………….

………………………………………………….
Unterschrift der Verfasserin/des Verfassers

to Katharina, Luis, and Conny

Abstract

This thesis develops a general concept for microphone arrays located on a partial spherical surface, which is enclosed by rigid angular boundaries. These partial spherical arrays inherently capture only sound sources from directions within the rigid boundaries. Thus they are especially suitable for scenarios where only sources within this directional range are of interest. The theoretical foundation of partial spherical microphone arrays is the solution of the Helmholtz equation in spherical coordinates, with boundary conditions in azimuth and zenith angle. The angular solutions form a complete set of orthonormal functions on the partial spherical surface. These allow for a modal decomposition of the sound field within the limited directional range, similar to the spherical harmonics decomposition used with spherical microphone arrays. Due to the lower number of basis functions for the partial spherical surface, a lower number of microphones is sufficient to achieve a similar spatial resolution as for a conventional spherical array over all directions. The challenges which come along with practical implementations of a partial spherical microphone arrays are discussed in detail. Based on acoustical measurements of a prototype array, the directivity of modal beamforming is investigated. To facilitate the reproduction on surrounding loudspeaker layouts with standard techniques, we present an approach to convert the modal representation of a partial spherical array into spherical harmonics. The performance of this conversion is evaluated using perceptually motivated error measures.

Kurzfassung

In dieser Dissertation wird ein allgemeines Konzept für Mikrofonarrays entwickelt, die auf einer Teilkugelfäche angeordnet und durch schallharte Berandungen im Winkel abgeschlossen sind. Solche Teilkugel-Mikrofonarrays erfassen nur Schallquellen aus dem von den Berandungen eingeschlossenen Winkelbereich. Sie sind daher besonders geeignet für Anwendungen, in welchen nur Quellen aus diesen Richtungen von Interesse sind. Die theoretische Grundlage für Teilkugel-Mikrofonarrays ist die Lösung der Helmholtz-Gleichung in Kugelkoordinaten mit Randbedingungen in Azimut und Zenitwinkel. Die winkelabhängigen Lösungsanteile ergeben einen vollständigen Satz von orthonormalen Funktionen auf der Teilkugelfläche und ermöglichen eine modale Zerlegung des Schallfeldes im eingeschränkten Winkelbereich, ähnlich der Schallfeldzerlegung in Kugelflächenfunktionen bei konventionellen Kugelmikrofonarrays. Durch die geringere Anzahl von Basisfunktionen auf der Teilkugelfläche ist mit weniger Mikrofonen eine ähnliche räumliche Auflösung erreichbar, wie bei Kugelmikrofonarrays über alle Richtungen. Die Herausforderungen, die sich bei der praktischen Umsetzung von Teilkugel-Mikrofonarrays ergeben, werden in dieser Arbeit ausführlich diskutiert. Anhand der akustischen Vermessung eines Prototyparrays wird die Richtchwirkung von modalem Beamforming untersucht. Für die einfache Wiedergabe von Schallszenen auf umgebenden Lautsprecheranordnungen mit Standardverfahren wird einen Ansatz gezeigt, mit dem die modale Repräsentation eines Teilkugelmikrofons in Kugelflächenfunktionen konvertiert werden kann. Die Eigenschaften dieser Konversion werden anhand von perzeptiv motivierten Fehlermaßen evaluiert.

x

Acknowledgements

I am very grateful for the employment at the Institute of Electronic Music and Acoustics (IEM), University of Music and Performing Arts Graz (KUG) within the projects AAP and ASD[1] during the research for my thesis.

I deeply thank my supervisor Robert Höldrich for his expertise, feedback and advise. Manny thanks go to Alois Sontacci for his great support and motivation. Special thanks go to Franz Zotter for his intellectual curiosity, the countless fruitful discussions, and the continuous collaboration. Above all, I thank the whole staff at IEM for the wonderful working atmosphere and the diverse support. For their efforts on exploring details of this research, I also thank Thomas Kössler, Florian Pausch, and Ben-Daniel Keller.

Finally, I would like express my gratitude to my parents Martha and Johann for their constant encouragement. My most heartfelt thanks go to my wife Cornelia, for her endless patience, incentive, and understanding as well as to my children Katharina and Luis, who always put a smile upon my face and take my mind off things.

Contents

Chapter 1

Introduction

Spatial audio recording and reproduction has a long and fascinating history[1], and today's cutting-edge spatial recording devices are compact spherical microphone arrays [ME02; Raf05]. Recordings with spherical microphone arrays allow for a modal, field-based representation of the sound scene, which originates from the mathematical formulation of acoustic waves in spherical coordinates. These modal components are the coefficients of the truncated spherical harmonics expansion of the microphone signals and also known as Ambisonics signals. The name Ambisonics and the idea of spatial audio recording and playback based on a spherical harmonics representation traces back to the 1970s [Ger73]. However, back then recording was limited to first order[2], which is achievable by coincident standard microphones, whereas capture of higher order components requires spherical microphone arrays.

The spatial resolution of spherical microphone arrays is uniform over all directions and directly related to its capable maximum order, whereby the number of spherical harmonics and thus the minimum number of required array elements grows quadratically with increasing order. A uniform resolution is clearly a desirable property, however, there are scenarios where not all directions are of interest. On the one hand, reproduction facilities are frequently not capable to reproduce sound from every direction, e.g. loudspeakers are very rarely positioned in the half-space below the audience as this requires costly constructions like a raised gridded floor. In this case, the superfluous information associated with sources from directions not covered by the playback facility is necessarily removed, either explicitly by regularization, e.g. [PZS09; ZPN12], or implicitly, e.g. by including a non-existing loudspeaker into the

---

[1]For a brief historical overview on spatial audio, the interested reader may revere to e.g. [Dav03].

[2]The spherical harmonics are categorized in orders, whereby the four components up to first order are represented by an omni-directional pattern and three perpendicular figure-of-eight patterns.

arrangement [ZF12]. On the other hand, within a recorded sound scene all relevant sound sources might be anyway withing a particular angular range, e.g. talking persons which are sitting or standing around the array. With these considerations, it seems worthwhile to investigate recording approaches which inherently capture only sound from a particular range of directions, while achieving a similar spatial resolution as with a spherical array, but with a reduced number of transducers.

It has been shown in [LD05], that the restriction of the angular range to a hemisphere can be achieved by using a hemispherical setup above a rigid surface at the horizontal plane. The rigid planar boundary restricts the physical wave field to those spherical harmonics components, which are even-symmetric with respect to the horizontal plane. In this simple case, the reflections due to the boundary can be regarded in terms of mirror sources. This thesis presents the generalization of this approach to partial spherical arrays bounded by arbitrary rigid boundary conditions in azimuth and zenith angle. In contrast to a boundary at the horizontal plane, the angular solutions of other angular boundary value problems are not a subset of the spherical harmonics. However, the solutions are of a similar structure and allow for a modal representation of a spatial sound field in a similar manner. The underlying theory for this generalization as well as its the practical issues are investigated in this thesis, which is organized as follows:

Chapter 2 reviews the theoretical foundations of spherical microphone arrays. Starting from the physics of sound waves, the solution of the Helmholtz equation in spherical coordinates naturally leads to modal sound field decomposition with spherical microphone arrays. The practical limitations using spherical microphone arrays are briefly discussed as well as beamforming and the reproduction of spatial sound scenes based on the modal representation captured by as spherical microphone array.

Chapter 3 develops the solutions of the angularly dependent differential equations, arising from the separation of the Helmholtz equation, with sound-soft or sound-hard boundary conditions. These solutions form a complete set of orthogonal basis functions on an interval in azimuth, respectively zenith angle, between the points where the boundary conditions are posed. This includes the solutions used in chapter 2 as special cases. To set the scene for these considerations, the Helmholtz equation in spherical coordinates is revisited, its general solution is discussed thoroughly, and a fundamental overview on the theory of Sturm-Liouville problems is given.

Chapter 4 shows the description of sound fields in regions of $\mathbb{R}^3$ bounded by rigid coordinate surfaces in spherical coordinates, such as cones and half-planes. Therefore

the orthogonal sets of basis functions for both angular variables, developed in chapter 3, are combined with the solutions of the radius depending differential equation. The angular dependent part of the solutions is combined to partial spherical harmonics yielding a complete orthogonal basis on the surface of the partial-sphere bounded by the rigid angular boundary conditions.

Chapter 5 addresses the practical application of the theoretical results from chapters 3 and 4. The concept of modal sound field decomposition and beamforming is generalized to microphone arrays located on partial spherical surfaces bounded by rigid angular boundary conditions. The issues and limitations of a practical implementation regarding spatial sampling and the regularization of the radial filters are investigated, and the results of a prototype array are shown. Furthermore an approach is presented to convert the modal representation captured by a partial spherical array into spherical harmonics, in order to allow for reproduction on conventional surrounding loudspeaker arrays.

Chapter 6 summarizes the findings of this work, draws a conclusion, and addresses open problems for future work.

Chapter 2

Capturing spatial sound scenes with spherical microphone arrays

This chapter starts with a brief review of the physics of sound waves and their time-independent description by the Helmholtz equation. The solution of the Helmholtz equation in spherical coordinates is the theoretical background for capturing spatial sound scenes with spherical arrays and naturally leads to modal sound field decomposition. Finally, a brief overview is given on beamforming and the reproduction of sound scenes based on their modal representation.

2.1 The Helmholtz equation

Consider the propagation of sound waves in a medium in $\mathbb{R}^3$, where the medium is an ideal, resting gas in a state of thermodynamic equilibrium, i.e. it possesses a static velocity of $\boldsymbol{v}_0 = 0$, a static pressure of $p_0 = \text{constant}$, and a static density of $\rho_0 = \text{constant}$. Furthermore, we assume the gas to be lossless, i.e. inviscid, that there is no heat transfer, i.e. an isentropic process, and that the perturbations of the static state are small. Under these conditions the motion of the gas can be described using the following equations, whereby we denote the perturbation of velocity, density and pressure at location $\boldsymbol{r} = [x, y, z]^{\mathrm{T}} \in \mathbb{R}^3$ and time t by $\boldsymbol{v}(\boldsymbol{r}, t)$, $\rho(\boldsymbol{r}, t)$, $p(\boldsymbol{r}, t)$, and the vector differential operator by $\boldsymbol{\nabla} = \left[\frac{\partial}{\partial x}, \frac{\partial}{\partial y}, \frac{\partial}{\partial z} \right]$. The governing equations are the linearized Euler's equation, cf. [CK13]

$$\rho_0 \frac{\partial \boldsymbol{v}(\boldsymbol{r}, t)}{\partial t} = -\boldsymbol{\nabla} p(\boldsymbol{r}, t), \tag{2.1}$$

which represents the conservation of momentum, the linearized equation of continuity, cf. [CK13]

$$\frac{\partial \rho(\boldsymbol{r}, t)}{\partial t} = -\rho_0 \boldsymbol{\nabla} \cdot \boldsymbol{v}(\boldsymbol{r}, t), \tag{2.2}$$

which represents the conservation of mass, and the linearized isentropic relation for an ideal gas, cf. [Mös09],

$$p(\boldsymbol{r}, t) = \kappa \frac{p_0}{\rho_0} \rho(\boldsymbol{r}, t), \tag{2.3}$$

where κ is the ratio of specific heats or also known as adiabatic index. Deriving eq. (2.2) with respect to time and inserting $\frac{\partial \boldsymbol{v}(r,t)}{\partial t}$ in terms of eq. (2.1) as well as $\rho(\boldsymbol{r}, t)$ in terms of eq. (2.3) yields the linear lossless wave equation,

$$\left(\Delta - \frac{1}{c^2} \frac{\partial^2}{\partial t^2} \right) p(\boldsymbol{r}, t) = 0, \tag{2.4}$$

where $\Delta := \boldsymbol{\nabla} \cdot \boldsymbol{\nabla} = \frac{\partial^2}{\partial x^2} + \frac{\partial^2}{\partial y^2} + \frac{\partial^2}{\partial z^2}$ is the Laplace operator and $c = \sqrt{\kappa \frac{p_0}{\rho_0}}$ is the speed of sound. The static pressure and density values are related by the equation of state of an ideal gas, $\frac{p_0}{\rho_0} = \frac{R}{M} T_0$, where $R \approx 8.234 \, \mathrm{JK^{-1} mol^{-1}}$ is the universal gas constant, M is the molar mass of the medium and T_0 is the static temperature. Hence, $c = \sqrt{\kappa \frac{R}{M} T_0}$ and depends on the material constants and the static temperature; at $20° \, \mathrm{C}$ for dry air with $\kappa = 1.4$ and $M = 28.97 \, \mathrm{g/mol}$ we get $c \approx 343 \, \mathrm{m/s}$.

Within this work we define the Fourier transform by

$$p(\boldsymbol{r}, \omega) := \int\limits_{-\infty}^{+\infty} p(\boldsymbol{r}, \omega) e^{-i\omega t} d\omega, \tag{2.5}$$

where $\omega = 2\pi f$, and f is the frequency. The Fourier transform of eq. (2.4) yields the frequency-domain equivalent of the wave equation,

$$\left(\Delta + k^2 \right) p(\boldsymbol{r}, \omega) = 0, \tag{2.6}$$

which is usually referred to as the Helmholtz equation and the abbreviation $k = \frac{\omega}{c}$ is called the wavenumber. A relation for pressure and velocity in the frequency domain is achieved by the Fourier transform of eq. (2.1) yielding

$$- i\rho_0 ck \, \boldsymbol{v}(\boldsymbol{r}, \omega) = -\boldsymbol{\nabla} p(\boldsymbol{r}, \omega). \tag{2.7}$$
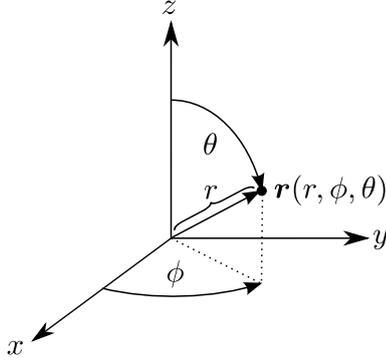
Figure 2.1: Definition of the spherical coordinate system as used within this work; radial distance r, azimuthal angle ϕ, and polar angle θ.

2.2 Solution of the Helmholtz equation in spherical coordinates

In spherical coordinates a point in $\mathbb{R}^3$ is specified by its distance to the origin r and two angles, the azimuth angle ϕ between the x-axis and the projection of the point onto the x-y plane, and the zenith angle θ between the z-axis and the point, cf. fig. 2.1. Expressing the position vector $\boldsymbol{r}$ in terms of the coordinate triple (r, ϕ, θ) yields

$$\boldsymbol{r} = r \left[\cos\phi\sin\theta, \sin\phi\sin\theta, \cos\theta \right]^{\mathrm{T}}. \tag{2.8}$$

In the following we will frequently use the abbreviation $\boldsymbol{\theta} := \left[\cos\phi\sin\theta, \sin\phi\sin\theta, \cos\theta \right]^{\mathrm{T}}$ for the direction vector of unit length. The unit sphere is therewith defined by

$$\mathbb{S}^2 := \{\boldsymbol{\theta}\}. \tag{2.9}$$

2.2.1 Homogeneous solution

The Helmholtz equation, cf. eq. (2.6), is separable in spherical coordinates. By a product ansatz the partial differential equation can be split in three ordinary differential equations, each of which depending on r, ϕ, or θ, only. Multiplying the solutions of these differential equations achieves a solution of the Helmholtz equation. The full details of deriving the solution are provided in chapter 3.

Assume a homogeneous region $\Omega := \{\boldsymbol{r} \in \mathbb{R}^3 : r_e \leq r \leq r_i\}$ where all sources are
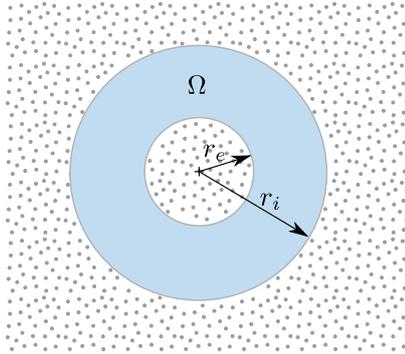
Figure 2.2: Sorce free spherical shell $\Omega := \left\{ \boldsymbol{r} \in \mathbb{R}^3 : r_e \leq r \leq r_i \right\}$

either located within an arbitrary small ball of radius r_e or outside an arbitrary large ball of radius r_i, see Figure 2.2, then any solution of eq. (2.6) can be expressed by,

$$p(\boldsymbol{r}) = \sum_{n=0}^{\infty} \sum_{m=-n}^{n} \left(b_{nm}\, j_n(kr) + c_{nm}\, h_n^{(2)}(kr) \right) Y_n^m(\boldsymbol{\theta}), \qquad (2.10)$$

whereby $Y_n^m(\boldsymbol{\theta})$ are the combined angular solutions, which are called spherical harmonics of order n and degree m; the radial solutions are the spherical Bessel functions $j_n(x)$ and spherical Hankel functions of the second kind $h_n^{(2)}(x)$, and b_{nm}, c_{nm} are coefficients that determine the solution. The functions involved in the solution are depicted in fig. 2.3.

The spherical harmonics may be equivalently defined either as real or complex valued functions and also their normalization can differ. We use the following real valued definition, normalized to the unit sphere,

$$Y_n^m(\boldsymbol{\theta}) = N_n^{|m|} \mathsf{P}_n^{|m|}(\cos\theta) \begin{cases} \cos(m\phi) & \text{for } m \geq 0, \\ \sin(m\phi) & \text{for } m < 0. \end{cases} \qquad (2.11)$$

whereby $\mathsf{P}_n^m(x)$ denotes the associated Legendre function of the first kind, and N_n^m is the normalization constant,

$$N_n^m = (-1)^m \sqrt{\tfrac{(2n+1)(2-\delta_{m0})(n-m)!}{4\pi(n+m)!}}. \qquad (2.12)$$

The spherical harmonics are orthonormal on the unit sphere, i.e.

$$\int_{\mathbb{S}^2} Y_n^m(\boldsymbol{\theta})\, Y_{n'}^{m'}(\boldsymbol{\theta})\, d\boldsymbol{\theta} = \delta_{nn'}\delta_{mm'}, \qquad (2.13)$$

where $\int\limits_{\mathbb{S}^2} d\boldsymbol{\theta} := \int\limits_{\phi=0}^{2\pi} \int\limits_{\theta=0}^{\pi} \sin\theta \, d\theta \, d\phi$ denotes the surface integral over the unit sphere

and δ_{ij} denotes the Kronecker delta, $\delta_{ij} := \begin{cases} 1 & \text{for } i = j \\ 0 & \text{for } i \neq j \end{cases}$. Furthermore, the set of

spherical harmonics is complete such that any square integrable function on $\mathbb{S}^2$ can be expressed by the series expansion

$$f(\boldsymbol{\theta}) = \sum_{n=0}^{\infty} \sum_{m=-n}^{n} \phi_{nm} Y_n^m(\boldsymbol{\theta}), \tag{2.14}$$

where the expansion coefficients are

$$\phi_{nm} = \int_{\mathbb{S}^2} f(\boldsymbol{\theta}) Y_n^m(\boldsymbol{\theta}) d\boldsymbol{\theta}. \tag{2.15}$$

Furthermore, orthogonality and completeness imply Parseval's relation,

$$\int_{\mathbb{S}^2} |f(\boldsymbol{\theta})|^2 = \sum_{n=0}^{\infty} \sum_{m=-n}^{n} |\phi_{nm}|^2, \tag{2.16}$$

and the closure relation

$$\sum_{n=0}^{\infty} \sum_{m=-n}^{n} Y_n^m(\boldsymbol{\theta}) Y_n^m(\boldsymbol{\theta'}) = \delta(\boldsymbol{\theta} - \boldsymbol{\theta'}). \tag{2.17}$$

Interior and exterior problems

There are two limiting cases of the above problem. For $r_i \to \infty$, the homogeneous region Ω is the exterior of a ball with radius r_e and thus a purely *exterior problem*, see fig. 2.4b. For $r_e \to 0$, Ω is the interior of a ball with radius r_i and thus this is a purely *interior problem*, see fig. 2.4a.

Interior problems. From fig. 2.3c it is seen that the spherical Hankel functions have a pole of order $n + 1$ at $kr = 0$, cf. the limiting form given in [DLMF, §10.52(i)]. Clearly, functions of the form eq. (2.10) involving $h_n^{(2)}(kr)$ do not fulfill eq. (2.6) at $kr = 0$. Thus for an interior problem the homogeneous solution reduces to

$$p(\boldsymbol{r}) = \sum_{n=0}^{\infty} j_n(kr) \sum_{m=-n}^{n} Y_n^m(\boldsymbol{\theta}) b_{nm}. \tag{2.18}$$
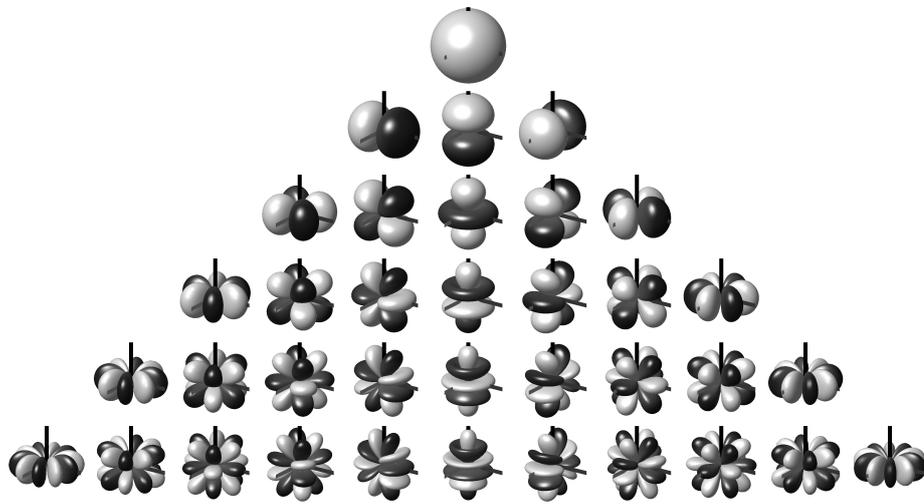
(a)
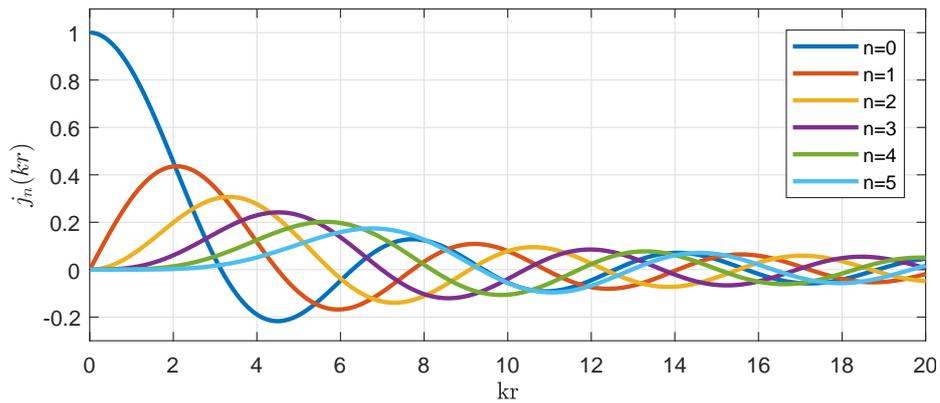
(b)
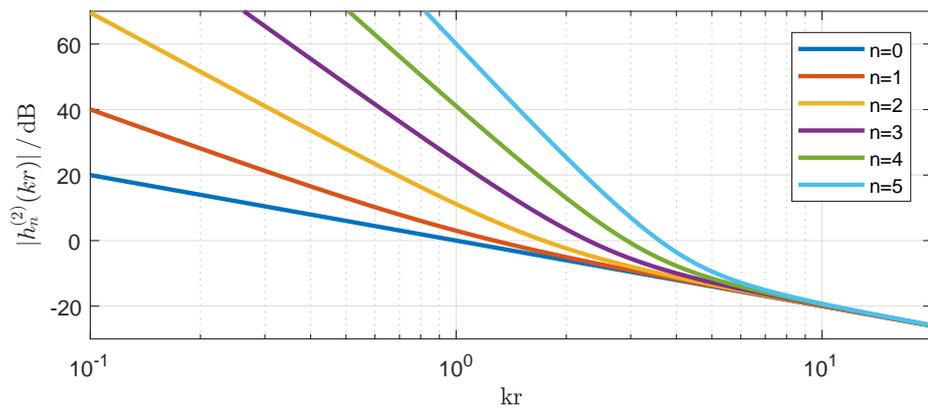
(c)

Figure 2.3: Functions involved in the solution of the Helmholtz equation in spherical coordinates: (a) balloon plots of spherical harmonics, (b) spherical Bessel functions, and (c) magnitude of the spherical Hankel function; for $n = 0 \ldots 5$.
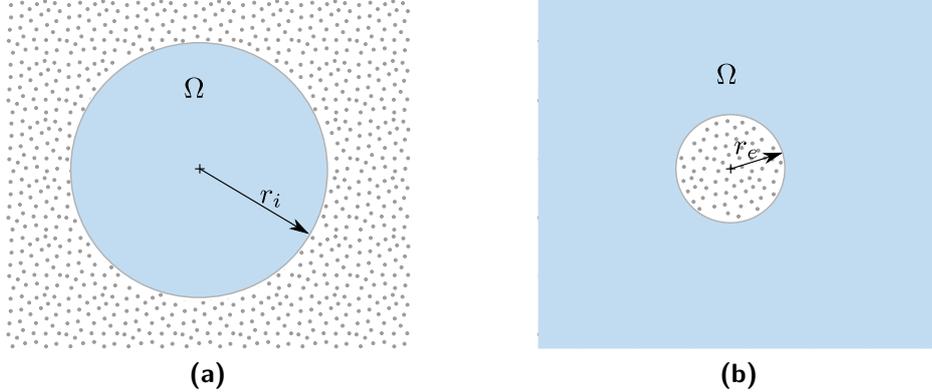
Figure 2.4: Special cases: (a) interior problem and (b) exterior problem.

Exterior problems. From a physical view point, a solution to such a problem must be purely radiating, meaning that it consist of traveling waves only, which propagate and diverge for $r \to \infty$. These solutions are singled out by Sommerfeld's radiation condition, [Som49, §28]. For $\mathbb{R}^3$ and the time dependency as defined in eq. (2.5), the radiation condition takes the form

$$\lim_{r \to \infty} r \left(\frac{\partial}{\partial r} + ik \right) p(\boldsymbol{r}) = 0. \tag{2.19}$$

In eq. (2.10) only the terms involving $h_n^{(2)}(kr)$ fulfill the above condition, whereas the terms involving $j_n(kr)$ do not. This can be easily proofed inserting the limiting forms of the spherical Bessel and Hankel functions, cf. [DLMF, §10.52(i)], in eq. (2.19). Thus for an exterior problem the homogeneous solution reduces to

$$p(\boldsymbol{r}) = \sum_{n=0}^{\infty} h_n^{(2)}(kr) \sum_{m=-n}^{n} Y_n^m(\boldsymbol{\theta}) c_{nm}. \tag{2.20}$$

Considering the general homogeneous solution, cf. eq. (2.10), as a superposition of these two special cases, it is obvious that the homogeneous field inside of a source-free spherical shell Ω with $r_i < \infty, r_e > 0$ consists of two components: the incident field due sources located outside a ball of radius r_i, which is represented by the coefficients b_{nm} and the radiating field due to sources located within a ball of radius r_e, which is represented by the coefficients c_{nm}.

2.2.2 Inhomogeneous solution, Green's function and plane waves

The inhomogeneous Helmholtz equation writes as

$$\Delta p(\boldsymbol{r}, \omega) + k^2 p(\boldsymbol{r}, \omega) = -f(\boldsymbol{r}), \tag{2.21}$$

where $f(\boldsymbol{r})$ is the force distribution exciting the field. One may solve the above equation directly for a particular excitation. However, it is more convenient to use Green's function. Green's function of a differential equation is the particular solution to the inhomogeneous equation excited by Dirac's delta distribution. In case of the Helmholtz equation in spherical coordinates, the problem writes as

$$\Delta G(\boldsymbol{r}, \boldsymbol{r}_0) + k^2 G(\boldsymbol{r}, \boldsymbol{r}_0) = \delta(\boldsymbol{r} - \boldsymbol{r}_0), \tag{2.22}$$

where Dirac's delta distribution in $\mathbb{R}^3$ expressed by spherical coordinates is $\delta(\boldsymbol{r} - \boldsymbol{r}_0) = \delta(\phi - \phi_0)\delta(\theta - \theta_0)\sin^{-1}(\theta)\delta(r - r_0)r^{-2}$, such that $\int_{\mathbb{R}^3} \delta(\boldsymbol{r} - \boldsymbol{r}_0)d\boldsymbol{r} = 1$.

Knowing $G(\boldsymbol{r}, \boldsymbol{r}_0)$, the solution for the inhomogeneous Helmholtz equation, Eq.(2.21), with an arbitrary excitation $f(\boldsymbol{r})$ is determined by[1]

$$p(\boldsymbol{r}) = \int_{\mathbb{R}^3} G(\boldsymbol{r}, \boldsymbol{r}_0)f(\boldsymbol{r}_0)\,d\boldsymbol{r}_0, \tag{2.23}$$

where $\int_{\mathbb{R}^3} u(\boldsymbol{r})\,d\boldsymbol{r} = \int_{\phi=0}^{2\pi}\int_{\theta=0}^{\pi}\int_{r=0}^{\infty} u(r, \phi, \theta)\,r^2\sin\theta\,dr\,d\theta\,d\phi$ denotes the volume integral over $\mathbb{R}^3$ in spherical coordinates.

Green's function. Green's function is not uniquely defined by the differential equation and requires additional boundary conditions. As we consider a free-field problem there are no boundaries in the literal sense. However, the solution is implicitly required to be physically feasible. Thus, $G(\boldsymbol{r}, \boldsymbol{r}_0)$ has to fulfill eq. (2.22) at the origin, where the differential equation is singular, and Sommerfeld's radiation condition, cf.

---

[1] This is easily proofed considering that the Helmholtz differential operator $\mathcal{L}_H := \Delta + k^2$ with respect to $\boldsymbol{r}$ can be interchanged with the integral operator over $\boldsymbol{r}_0$,

$$\mathcal{L}_H\, p(\boldsymbol{r}) = \mathcal{L}_H \int_{\mathbb{R}^3} G(\boldsymbol{r}, \boldsymbol{r}_0)f(\boldsymbol{r}_0)\,d\boldsymbol{r}_0 = \int_{\mathbb{R}^3} \underbrace{\mathcal{L}_H\, G(\boldsymbol{r}, \boldsymbol{r}_0)}_{=\delta(\boldsymbol{r} - \boldsymbol{r}_0)} f(\boldsymbol{r}_0)\,d\boldsymbol{r}_0 = f(\boldsymbol{r}).$$

eq. (2.19). With these conditions Green's function yields,

$$G(\boldsymbol{r}, \boldsymbol{r}_0) = -ik \sum_{n=0}^{\infty} \sum_{m=-n}^{n} Y_n^m(\boldsymbol{\theta}) Y_n^m(\boldsymbol{\theta}_0) \begin{cases} j_n(kr) h_n^{(2)}(kr_0) & \text{for } r \leq r_0, \\ j_n(kr_0) h_n^{(2)}(kr) & \text{for } r \geq r_0. \end{cases} \tag{2.24}$$

A detailed derivation is given in appendix A.

Evaluating the above equation at the origin yields $G(\boldsymbol{r}, \boldsymbol{0}) = \frac{e^{-ikr}}{4\pi r}$, as all spherical Bessel functions are zero at $r = 0$, except $j_0(0) = 1$, cf. fig. 2.3b, and $h_0^{(2)}(kr) = \frac{-ie^{-ikr}}{kr}$, $Y_0^0(\boldsymbol{\theta}) = \frac{1}{\sqrt{4\pi}}$. Due to the free field condition, the solution of the Helmholtz equation is invariant for a shifted origin of the coordinate system, i.e. $G(\boldsymbol{r}, \boldsymbol{r}_0) = G(\boldsymbol{r} + \boldsymbol{r}', \boldsymbol{r}_0 + \boldsymbol{r}')$, and it follows

$$G(\boldsymbol{r}, \boldsymbol{r}_0) = \frac{e^{-ik\|\boldsymbol{r} - \boldsymbol{r}_0\|}}{4\pi\|\boldsymbol{r} - \boldsymbol{r}_0\|}. \tag{2.25}$$

Plane waves. Expanding $\|\boldsymbol{r} - \boldsymbol{r}_0\|$ into a Taylor series[2] yields the asymptotic expressions[3] $\|\boldsymbol{r} - \boldsymbol{r}_0\| \sim r_0$ and $e^{-ik\|\boldsymbol{r} - \boldsymbol{r}_0\|} \sim e^{-ik(r_0 - \boldsymbol{\theta}_0^{\mathrm{T}} \boldsymbol{r})}$ for $r_0 \to \infty$. Therewith, from eq. (2.25) follows the asymptotic expression for Green's function

$$G(\boldsymbol{r}, \boldsymbol{r}_0) \sim \frac{e^{-ikr_0}}{4\pi r_0} e^{ik\boldsymbol{\theta}_0^{\mathrm{T}} \boldsymbol{r}}, \quad r_0 \to \infty. \tag{2.26}$$

The sound pressure of a plane wave from direction $\boldsymbol{\theta}_0$ yields, cf. [Wil99, p. 23],

$$p(\boldsymbol{r}) = e^{ik\boldsymbol{\theta}_0^{\mathrm{T}} \boldsymbol{r}}. \tag{2.27}$$

Comparing the above equation to eq. (2.26) shows that the expression of a plane wave is achieved by taking the limiting form of Green's function for $r_0 \to \infty$ multiplied by $4\pi r_0 e^{ikr_0}$. Hence, from eq. (2.24) and the asymptotic equivalent of the spherical Hankel function, $h_n^{(2)}(x) \sim i^{n+1} x^{-1} e^{-ix}$ as $x \to \infty$, cf. [DLMF, §10.52(ii)], eq. (2.27) is equivalently expressed by

$$p(\boldsymbol{r}) = 4\pi \sum_{n=0}^{\infty} i^n j_n(kr) \sum_{m=-n}^{n} Y_n^m(\boldsymbol{\theta}) Y_n^m(\boldsymbol{\theta}_0). \tag{2.28}$$

---

[2]From the Taylor series of $\sqrt{1+x}$ follows

$$\|\boldsymbol{r} - \boldsymbol{r}_0\| = r_0 \sqrt{1 + \frac{r^2}{r_0^2} - 2\frac{\boldsymbol{\theta}_0^{\mathrm{T}} \boldsymbol{r}}{r_0}} = \sum_{n=0}^{\infty} \frac{(-1)^n (2n)!}{(1-2n)(n!)^2 4^n} r_0^{1-n} \left(\frac{r^2}{r_0} - 2\boldsymbol{\theta}_0^{\mathrm{T}} \boldsymbol{r}\right)^n$$

[3]A function $g(x)$ is asymptotically equivalent to $f(x)$ for $x \to b$ if $\lim_{x \to b} \frac{f(x)}{g(x)} = 1$. We denote asymptotic equivalence by $f(x) \sim g(x)$ for $x \to b$.

2.3 Modal sound field decomposition using spherical microphone arrays

The solution of an interior problem, cf. eq. (2.18), shows that the sound field due to surrounding sources is uniquely determined by the modal coefficients b_{nm}. Each of these coefficients can be determined formally from the pressure distribution on a spherical surface, as long as the radial solution is non-zero. This follows from the orthogonality of the spherical harmonics.

In practical applications, the sound pressure is well accessible by microphones, so that it seems natural to use a spherical microphone array to capture surrounding sound scenes. Clearly, using a microphone array, the pressure data is only accessible on discrete points. In the following subsections we will consider how this discretization affects the decomposition.

Note that in a similar fashion eq. (2.20) suggest to determine the field of radiating sources by a surrounding microphone array. This is applicable in radiation analysis of musical instruments [Zot09a] or sound power measurements [PSB+16].

2.3.1 Formulation of the problem

A spherical microphone array consists of a number of M microphones located on the surface of a sphere with radius r_m, and a surrounding sound scene is the field produced by an arbitrary number of sources which are all located outside of the volume enclosed by the array. As discussed in section 2.2.1, this constitutes an interior problem, cf. fig. 2.4(a), and hence the sound pressure distribution at the location of the array yields, cf. eq. (2.18),

$$p(r_m\boldsymbol{\theta}) = \sum_{n=0}^{\infty} j_n(kr_m) \sum_{m=-n}^{n} Y_n^m(\boldsymbol{\theta})\, b_{nm}. \tag{2.29}$$

For notational convenience we express the infinite sum in the above equation by the infinite matrix product,

$$p(r_m\boldsymbol{\theta}) = \boldsymbol{y}^{\mathrm{T}}(\boldsymbol{\theta})\, diag\{\boldsymbol{j}(kr_m)\}\, \boldsymbol{b}, \tag{2.30}$$

whereby

$$\boldsymbol{y}(\boldsymbol{\theta}) := [Y_0^0(\boldsymbol{\theta}), \ldots, Y_n^m(\boldsymbol{\theta}), \ldots]^{\mathrm{T}},$$

$$\boldsymbol{j}(kr_m) := [j_0(kr_m), \ldots, \underbrace{j_n(kr_m), \ldots, j_n(kr_m)}_{2n+1}, \ldots]^{\mathrm{T}}, \tag{2.31}$$

$$\boldsymbol{b} := [b_{00}, \ldots, b_{nm}, \ldots]^{\mathrm{T}}.$$

The array microphones sample the sound pressure pattern $p(r_m\boldsymbol{\theta})$ at M discrete positions $\boldsymbol{\theta}_i$, $i = 1, \ldots, \mathrm{M}$. We denote the discretized pressure pattern by the vector $\boldsymbol{p} := [p(r_m\boldsymbol{\theta}_1), \ldots, p(r_m\boldsymbol{\theta}_{\mathrm{M}})]^{\mathrm{T}}$ yielding

$$\boldsymbol{p} = \boldsymbol{Y} \, diag\{\boldsymbol{j}(kr_m)\}\boldsymbol{b}, \tag{2.32}$$

whereby

$$\boldsymbol{Y} := [\boldsymbol{y}(\boldsymbol{\theta}_1), \ldots, \boldsymbol{y}(\boldsymbol{\theta}_i), \ldots, \boldsymbol{y}(\boldsymbol{\theta}_{\mathrm{M}})]^{\mathrm{T}}. \tag{2.33}$$

A sound scene is fully represented by the coefficient vector $\boldsymbol{b}$, however it is more convenient for most applications to characterize the sound scene in terms of a continuous spherical source distribution $f(\boldsymbol{\theta})$ located at some radius $r_s > r_m$. Plugging this source distribution as an excitation $f(\boldsymbol{r}) = f(\boldsymbol{\theta})\delta(r - r_s)\, r^{-2}$ in eq. (2.23) and using eq. (2.24) yields for $r < r_s$,

$$p(\boldsymbol{r}) = -ik \sum_{n=0}^{\infty} j_n(kr)h_n^{(2)}(kr_s) \sum_{m=-n}^{n} Y_n^m(\boldsymbol{\theta}) \int_{\mathbb{S}^2} Y_n^m(\boldsymbol{\theta}_0) f(\boldsymbol{\theta}_0) d\boldsymbol{\theta}_0. \tag{2.34}$$

The remaining integral $\int_{\mathbb{S}^2} Y_n^m(\boldsymbol{\theta})f(\boldsymbol{\theta})d\boldsymbol{\theta} = \phi_{nm}$ in the above equation represents the expansion coefficients of the spherical harmonics series expansion of the source distribution, cf. eqs. (2.14) and (2.15). Comparing the above equation with the solution of the interior problem, cf. eq. (2.18), shows the connection between the coefficients of the incident field and the spherical source distribution,

$$b_{nm} = -ikh_n^{(2)}(kr_s)\, \phi_{nm}. \tag{2.35}$$

This allows to express eq. (2.32) in terms of the source distribution,

$$\boldsymbol{p} = \boldsymbol{Y} \, diag\{\boldsymbol{w}(k, r_m, r_s)\}\boldsymbol{\phi}, \tag{2.36}$$

whereby

$$\boldsymbol{\phi} := [\phi_{00}, \ldots, \phi_{nm}, \ldots],$$

$$\boldsymbol{w}(k, r_m, r_s) := [w_0(k, r_m, r_s), \ldots, \underbrace{w_n(k, r_m, r_s), \ldots, w_n(k, r_m, r_s)}_{2n+1}, \ldots]^{\mathrm{T}}, \quad (2.37)$$

$$w_n(k, r_m, r_s) := -ikj_n(kr_m) \, h_n^{(2)}(kr_s).$$

We assume that the spherical source distribution is in the far field, as this is appropriate in most practical applications and so we get rid of the dependency of r_s. In this case, the $h_n^{(2)}(kr_s)$ can be replaced by its large argument equivalent $h_n^{(2)}(x) \sim i^{n+1}x^{-1}e^{-ix}$; furthermore we omit the common delay and gain factor $\frac{e^{-ikr_s}}{r_s}$. Therewith $w_n(k, r_m, r_s)$ reduces to

$$w_n(kr_m) = i^n j_n(kr_m). \quad (2.38)$$

Clearly, eq. (2.36) is formally highly underdetermined due to the infinite length of $\boldsymbol{\phi}$, which prevents a direct inversion without further assumptions. As the degrees of freedom of the array are limited by the number of microphones, and considering all practical imperfections, the maximum achievable result is an optimal estimate $\hat{\boldsymbol{\phi}}_{\mathrm{N}} := [\hat{\phi}_{00}, \ldots, \hat{\phi}_{\mathrm{NN}}]^{\mathrm{T}}$ of the first $(\mathrm{N}+1)^2$ coefficients $\boldsymbol{\phi}$ from the sampled pressure distribution $\boldsymbol{p}$, where $(\mathrm{N}+1)^2 \leq \mathrm{M}$. Thereby we assume that only these components of the spherical source distribution contribute to the pressure pattern at the array surface, i.e. $p(r_m\boldsymbol{\theta})$ is spatially band-limited with a maximum order of N. To simplify the following considerations, we choose $\mathrm{M} = (\mathrm{N}+1)^2$. In this case eq. (2.36) has formally a unique solution,

$$\boldsymbol{\phi}_{\mathrm{N}} = diag\{\boldsymbol{w}_{\mathrm{N}}(kr_m)\}^{-1}\boldsymbol{Y}_{\mathrm{N}}^{-1}\boldsymbol{p}, \quad (2.39)$$

whereby $\boldsymbol{Y}_{\mathrm{N}} := [\boldsymbol{y}_{\mathrm{N}}(\boldsymbol{\theta}_1), \ldots, \boldsymbol{y}(\boldsymbol{\theta}_{\mathrm{M}})]^{\mathrm{T}}$ with $\boldsymbol{y}_{\mathrm{N}}(\boldsymbol{\theta}) := [Y_0^0(\boldsymbol{\theta}), \ldots, Y_{\mathrm{N}}^{\mathrm{N}}(\boldsymbol{\theta})]^{\mathrm{T}}$, and $\boldsymbol{w}_{\mathrm{N}}(kr_m) := [w_0(kr_m), \ldots, w_{\mathrm{N}}(kr_m)]^{\mathrm{T}}$. However, the data in $\boldsymbol{p}$ is likely corrupted by errors such as gain mismatch and self-noise in the microphones, positioning errors, etc. Hence, $\boldsymbol{Y}_{\mathrm{N}}$ and $diag\{\boldsymbol{w}_{\mathrm{N}}(kr_m)\}$ are both required to be well-conditioned, as otherwise the huge amplification of errors renders the result useless.

2.3.2   Design and implementations issues

The practical applicability of eq. (2.39) depends to a great extent on the design of a spherical microphone array. Typical design parameters are the radius of the sphere,

type and number of microphones as well as their distribution, and the configuration of spherical surface.

Array surface and microphone type. If one implements a spherical microphone array on an open spherical surface, a mayor drawback is that $w_n(kr_m)$ is proportional to $j_n(kr_m)$ and thus has zeros for some frequencies, depending on the array radius. Thus for $kr_m > 2$ the inversion of eq. (2.39) is problematic, as illustrated in fig. 2.5a. This problem can be avoided either by using directive microphones, e.g. cardioid capsules [Ple09], or by using a rigid material for the array surface. In both cases the design change alters the solution of the Helmholtz equation in a way that $w_{nm}(kr_m)$ is free of zeros. The problem with cardioid microphones is, however that their directivity patterns are rarely ideal and frequency independent. Therefore we focus within this work on the simple and robust solution using rigid spherical microphone arrays.

The pressure field due to a spherical source distribution in the presence of a sound hard sphere, centered at the origin, is obtained in the same way as eq. (2.34), using Green's functions fulfilling the respective boundary condition. If we require $\frac{\partial G(\boldsymbol{r}, \boldsymbol{r_0})}{\partial r} = 0$ at $r = r_m$ we get for $r \leq r_0$, cf. appendix A,

$$ G(\boldsymbol{r}, \boldsymbol{r_0}) = -ik \sum_{n=0}^{\infty} h_n^{(2)}(kr_0) \left(j_n(kr) - \frac{j_n'(kr_m)}{h_n'^{(2)}(kr_m)} h_n^{(2)}(kr) \right) \sum_{m=-n}^{n} Y_n^m(\boldsymbol{\theta}) Y_n^m(\boldsymbol{\theta_0}). \tag{2.40} $$

Using the above equation in eq. (2.23), excited by a spherical source distribution, results in an equation similar to eq. (2.36), where only the radius depending part is changed to $w_n(k, r_m, r_s) = -ikh_n^{(2)}(kr_s) \left(j_n(kr_m) - \frac{j_n'(kr_m)}{h_n'^{(2)}(kr_m)} h_n^{(2)}(kr_m) \right)$. Using the Wronskian relation $\mathscr{W}\left\{ j_\nu(kr), h_\nu^{(2)}(kr) \right\} = j_\nu(kr) h_\nu'^{(2)}(kr) - h_\nu^{(2)}(kr) j_\nu'(kr) = -i(kr)^{-2}$, the radius depending part simplifies to

$$ w_n(k, r_m, r_s) = -\frac{h_n^{(2)}(kr_s)}{(kr_m)^2 h_n'^{(2)}(kr_m)}. \tag{2.41} $$

Assuming the sources to be in the far field, $r_s \to \infty$, and omitting the common delay and gain factor $\frac{e^{-ikr_s}}{r_s}$, the above equation further reduces to

$$ w_n(kr_m) = \frac{i^{n-1}}{(kr_m)^2 h_n'^{(2)}(kr_m)}. \tag{2.42} $$

This function has no zeros and hence is less problematic in the inversion, see fig. 2.5b.
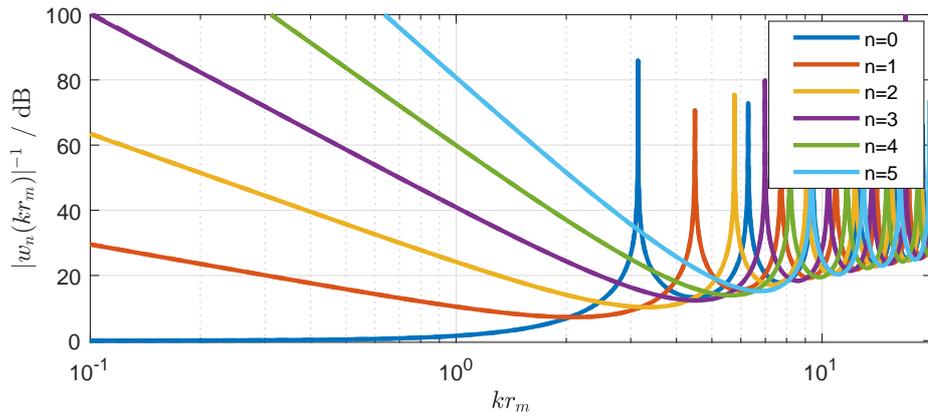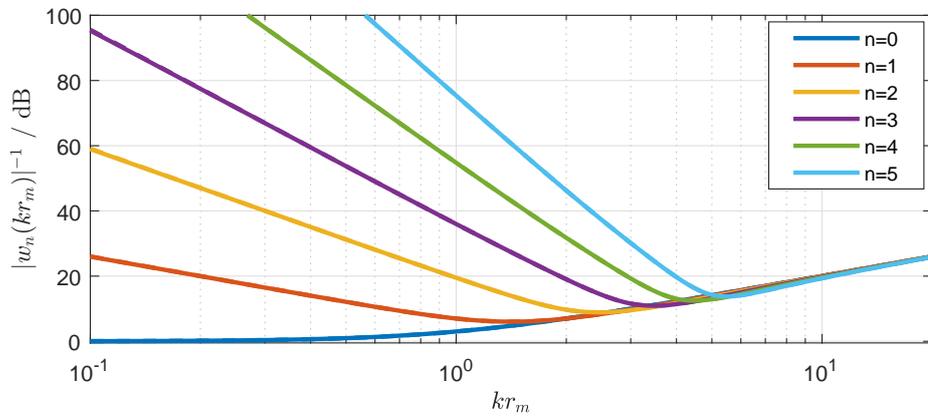
Figure 2.5: Magnitude of the inverted radial function for (a) an open spherical array, according to eq. (2.38), and (b) a rigid spherical array, according to eq. (2.42).

Frequency limits. Another critical aspect concerning the inversion of the radial functions is evident from the plots in fig. 2.5: For high orders n and low frequencies the inversion would require huge gains. Using the asymptotic equivalent $h_n^{(2)}(x) \sim i(2n-1)!!x^{-n-1}$ for $x \to 0$, cf. [DLMF, §10.52(i)], shows that $w_n^{-1}(kr_m)$ grows towards low frequencies asymptotically with $w_n^{-1}(kr_m) \sim i^{-n}(2n-1)!!(n+1)(kr_m)^{-n}$. In practical applications, this problem is usually considered by defining a maximum gain for the filters that implement the inverted radial functions to avoid inadequately high error amplification. This maximum filter gain, together with the array radius, determines the lower frequency limit, down to which modal sound field decomposition with a certain maximum order is applicable. Clearly, the lower frequency limit shifts down by reducing the maximum order and therewith the spatial resolution, see e.g. [Lös14; BPSW11].

The upper frequency limit is usually estimated by the rule of thumb $kr_m = N$, cf. [Raf05]. Beyond this limit higher order components of the source distribution start to contribute significantly to the pressure distribution at the array surfaces. Thus the decomposition problem becomes underdetermined and this leads to a misinterpretation. The modal components of order $n > N$ cannot be resolved by the array and are mapped into lower order components, whereby the particular mapping depends on the sampling distribution, cf. [RWB07]. These errors are referred to as spatial aliasing. For far field sources the contribution of higher orders is similar to the error of plane wave sound fields reproduced by loudspeakers, cf.[WA01], which leads to the approximate rule of thumb stated above.

Spherical sampling. The values in the matrix $\boldsymbol{Y}_N$, and hence its numerical condition, are determined by the location of the microphones. A well-conditioned matrix is crucial for modal sound field decomposition. Therefore the choice of the sampling points deserves particular attention. A sampling configuration shall be efficient in terms of the number of sampling points, and robust to additive errors arising from measuring the sampled quantity, e.g. microphone self-noise. The robustness is usually measured in terms of the condition number of the matrix, which is the ratio of the largest to the smallest singular value of the matrix. The condition number of $\boldsymbol{Y}_N$ represents the upper bound of the relative error amplification in $\boldsymbol{p}$, caused by multiplication with $\boldsymbol{Y}_N^{-1}$ in eq. (2.39). For a comprehensive overview on sampling strategies for the sphere see [Zot09b], where also many references to available literature are found.

2.4 Beamforming and reproduction of sound scenes

The modal representation of a sound scene, achieved from a spherical microphone array using modal sound field decomposition, is usually used either for beamforming or to reproduce the captured sound scene with an surrounding spherical loudspeaker array. A brief description of these applications is given in the following subsections.

2.4.1 Beamforming

In general, the goal of beamforming is to capture sources arriving from a desired target direction and to optimally suppress sources from all other directions. We assume that all sources are far away from the array and arrive as plane waves, i.e. far-field beamforming. Furthermore we assume an ideal spherical microphone array operating in its feasible frequency range, i.e. it gives access to the modal coefficients of the spatially band-limited source distribution $\boldsymbol{\phi}_{\mathrm{N}}$.

Beamforming is accomplished simply by a weighted sum of the modal coefficients. In matrix notation this yields

$$s = \boldsymbol{\gamma}^{\mathrm{T}}(\boldsymbol{\theta}_b)\boldsymbol{\phi}_{\mathrm{N}}, \tag{2.43}$$

whereby $\boldsymbol{\gamma}(\boldsymbol{\theta}_b)$ is a vector containing the weights for a desired target direction $\boldsymbol{\theta}_b$. To deduce suitable beamforming weights, we first consider how these affect the directivity of the beamformer. Comparing eq. (2.28) and eq. (2.18) shows that for a plane wave from direction $\boldsymbol{\theta}$ the modal coefficients are $b_{nm} = 4\pi i^n Y_n^m(\boldsymbol{\theta})$. Using eq. (2.35) and the far field equivalent of the Hankel function leads to the coefficients of a spherical source distribution. Omitting constant delay and gain factors this yields $\boldsymbol{\phi} = \boldsymbol{y}(\boldsymbol{\theta})$. Inserting this in eq. (2.43) yields a function, which represents the direction dependent far-field gain of the beamformer, i.e. its directivity pattern,

$$d(\boldsymbol{\theta}) = \boldsymbol{\gamma}^{\mathrm{T}}(\boldsymbol{\theta}_b)\boldsymbol{y}_{\mathrm{N}}(\boldsymbol{\theta}). \tag{2.44}$$

The above equation shows that the beamformer weights are the coefficients of the spherical harmonics expansion of the directivity pattern, cf. eq. (2.14). Based on this relation, the beamforming weights are determined by specifying some optimization criterion. For example, the maximum directivity beamformer results in, cf. [SYS+10]

$$\boldsymbol{\gamma}(\boldsymbol{\theta}_b) = \boldsymbol{y}_{\mathrm{N}}(\boldsymbol{\theta}_b). \tag{2.45}$$

Optimizing the beam pattern due to other criteria, e.g. minimum side lobes [SYS11]

or parametric designs like Dolph-Chebyshev [KR09], result simply in direction-independent additional order weights,

$$\boldsymbol{\gamma}(\boldsymbol{\theta}_b) = diag\{a_\mathrm{N}\}\boldsymbol{y}_\mathrm{N}(\boldsymbol{\theta}_b),$$ (2.46)

where $\boldsymbol{a}_\mathrm{N} = [a_0, \ldots, \underbrace{a_n, \ldots, a_n}_{2n+1}, \ldots, a_\mathrm{N}]^\mathrm{T}$.

2.4.2   Reproduction of sound scenes

For simplification, we assume the excitation force due to a loudspeaker being concentrated in a single point. Therewith, the force distribution of a surrounding spherical loudspeaker setup yields $f(\boldsymbol{r}) = f(\boldsymbol{\theta})\,\delta(r - r_s)\,r^{-2}$, where

$$f(\boldsymbol{\theta}) = \sum_{l=1}^{\mathrm{L}} g_l\,\delta(\boldsymbol{\theta} - \boldsymbol{\theta}_l),$$ (2.47)

is the spherical source distribution representing the loudspeaker setup, and g_l are the driving gains of the loudspeakers. Inserting the above equation in eq. (2.15), and expressing the delta function by the closure relation, cf. eq. (2.17), yields the expansion coefficients $\phi_{nm} = \sum_{l=1}^{\mathrm{L}} g_l Y_n^m(\boldsymbol{\theta_l})$, which is equivalent expressed in matrix notation by

$$\boldsymbol{\phi} = \sum_{l=1}^{\mathrm{L}} g_l\,\boldsymbol{y}(\boldsymbol{\theta}_l).$$ (2.48)

Stacking the loudspeaker gains in a vector, $\boldsymbol{g} = [g_1, \ldots, g_\mathrm{L}]^\mathrm{T}$, we get $\boldsymbol{\phi} = \boldsymbol{Y}\boldsymbol{g}$. From a spherical microphone array we expect only the spatially band-limited part of a surrounding source distribution. Hence for the loudspeaker side, we also consider only the lower order components with the same spatial band-limit,

$$\boldsymbol{\phi}_\mathrm{N} = \boldsymbol{Y}_\mathrm{N}\,\boldsymbol{g}.$$ (2.49)

To simplify the following consideration, we assume that the number of loudspeakers equals the number of modal components, i.e. $\mathrm{L} = (\mathrm{N} + 1)^2$. In this case the driving gains for the loudspeakers, which achieve the same excitation pattern as captured by the spherical microphone array, can be formally determined by inverting the above equation,

$$\boldsymbol{g} = \boldsymbol{Y}_\mathrm{N}^{-1}\boldsymbol{\phi}_\mathrm{N}.$$ (2.50)

Note that we silently assume here that the radius of the spherical loudspeaker distribution is equal to the radius of the surrounding source distribution used in the modal sound field decomposition.

In practice, there are several potential weaknesses when applying eq. (2.50) to reproduce captured sound scenes. First of all, the inversion requires a good condition of the matrix $\boldsymbol{Y}_{\mathrm{N}}$, as otherwise large loudspeaker gains due to errors render the result useless. A good condition is here much harder to achieve as for a microphone array. Arranging loudspeakers in a room is subject to many restrictions, e.g. doors, windows, ect., and in many cases only hemispherical setups are achievable as a fully spherical distribution is not manageable.

As shown in [WA01], for the spatially band-limited approximation of a plane wave, i.e. omitting all terms for which $n > \mathrm{N}$ in eq. (2.28), the normalized mean squared error on a sphere of radius $r = \frac{N}{k}$ is about 4% and rapidly increases with r. This clearly shows that an accurate reproduction is only achieved in rather small area around the origin, even for a good condition of $\boldsymbol{Y}_{\mathrm{N}}$. The size of this area depends on frequency and the particular spatial band-limit.

Approaches similar to eq. (2.50) are nonetheless used for 3D audio reproduction with moderate numbers of loudspeakers, i.e. a spatial band-limit of typically $\mathrm{N} = 1$ to 5. These reproduction approaches are usually referred to as *Ambisonics* [Ger73; Fel75]. In Ambisonics terminology, the mapping from the modal signals to driving the signals of the loudspeakers is referred to as decoding,

$$\boldsymbol{g} = \boldsymbol{D}\boldsymbol{\phi}_{\mathrm{N}}, \tag{2.51}$$

where $\boldsymbol{D}$ is called the decoder matrix. Obviously, eq. (2.50) is achieved for setting $\boldsymbol{D} = \boldsymbol{Y}^{-1}$. This type of decoding is referred to as mode-matching, cf. [ZPF09]. Carefully designed decoders are able to provide a plausible and convincing perception, also for larger audience areas and irregular loudspeaker distributions. Naturally, such decoding strategies require to disengage the problem from a physically accurate synthesis of the sound field.

In the last decade, several decoding strategies have been presented, which aim at a perceptually optimal reproduction and cope with non-uniform loudspeaker distributions. In [EJZ14; BHL10; MW10], non-linear optimization techniques are used to minimize cost functions in terms of perceptual relevant parameters [Ger92]. The energy-preserving decoder proposed in [ZPN12] achieves a regularization of eq. (2.50) by reducing the number of basis functions, similar to spherical Slepian functions, cf.

[ZP12]. This is especially applicable for loudspeaker layouts covering only a part of the sphere, e.g. hemispherical setups. The all-round Ambisonics decoder (AllRAD), cf. [ZF12], achieves decoding to virtually any loudspeaker distribution by a two-step approach. First, an ideal virtual loudspeaker setup is considered, i.e. a discrete source distribution with a high number of sampling points located such that $\boldsymbol{Y}^{\mathrm{T}} = \boldsymbol{Y}^{-1}$, and the modal signals are decoded to these virtual loudspeakers. In a second step, the virtual loudspeaker signals are distributed to the real loudspeakers by vector based amplitude panning (VBAP), cf. [Pul97]. A comparison of the latter two approaches and their particularities is shown in [ZFP13].

Chapter 3

Helmholtz equation revisited

The modal decomposition of a sound field, as discussed in the previous chapters, is based on spherical harmonics. These functions form a complete, orthonormal set of functions on the two-dimensional sphere $\mathbb{S}^2$. Hence, any square integrable function on $\mathbb{S}^2$ can be expanded in a series of spherical harmonics. However, if one considers not the entire surface of the sphere, but only a partial spherical surface, the spherical harmonics loose this important property.

As we will show within this chapter, there are complete sets of orthonormal functions for certain partial spherical surfaces. Similarly to the spherical harmonics, these functions are based on the solution of the Helmholtz equation in spherical coordinates and are combinations of orthogonal functions in azimuth and zenith angle. For example, reducing the set of spherical harmonics to those, which are either even- or odd-symmetric with respect to the horizontal plane, yields a complete orthogonal set of functions on the hemisphere. In fact, the even- and odd-symmetric spherical harmonics are the eigenfunctions of the angular part of the Helmholtz equation for a Neumann respectively a Dirichlet boundary condition at the horizontal plane. The fundamental theory behind this is known as Sturm-Liouville theory. Its main tenet states that the eigenfunctions of certain second-order differential equations, which fulfill a two-point boundary condition, form a complete orthogonal sequence. Beyond many other classical differential equations, the differential equations resulting from the separation of the Helmholtz equation in spherical coordinates are of this form. Also the full set of spherical harmonics is covered by the Sturm-Liouville theory as a special case. It shows that the trigonometric functions result from a periodic boundary condition, claiming continuity and periodicity in the azimuth. The associated Legendre functions of the first kind, with integer degree and order, are the eigenfunctions of the associated Legendre differential equation for singular boundary conditions in the

zenith angle, claiming that the solution does not diverge at $\theta = 0°$, $\theta = 180°$.

The aim of this chapter is to provide the theoretical foundations of complete orthogonal function sets resulting from solutions of the Helmholtz equations in spherical coordinates. First, we discuss the general solution of the Helmholtz equation, which, by separation of variables, splits up in three ordinary differential equations of second order. In the second section provides an introduction to the Sturm-Liouville theory. Finally, the application of the Sturm-Liouville theory to the Helmholtz equation is show and the respective orthogonal function sets are established.

Chapter 4 shows the combination of the solution in azimuth and zenith angle to complete sets of orthogonal functions for partial spherical surfaces. These orthogonal function sets, together with the corresponding radial solutions, yield the solutions of the Helmholtz equation in regions bounded by sound-hard coordinate surfaces in ϕ and θ. Modal sound field decompositions based on these solutions is discussed in chapter 5.

3.1 General solution of the Helmholtz equation in spherical coordinates

The Helmholtz equation is the partial differential equation, cf. section 2.1,

$$\Delta p(\boldsymbol{r}) + k^2 p(\boldsymbol{r}) = 0 , \tag{3.1}$$

whereby in spherical coordinates, as defined in section 2.2, the Laplace-Operator Δ yields, cf. [BSMM07, p. 658],

$$\Delta = \frac{1}{r^2} \frac{\partial}{\partial r} \left(r^2 \frac{\partial}{\partial r} \right) + \frac{1}{r^2 \sin\theta} \frac{\partial}{\partial \theta} \left(\sin\theta \frac{\partial}{\partial \theta} \right) + \frac{1}{r^2 \sin^2\theta} \frac{\partial^2}{\partial \phi^2} . \tag{3.2}$$

We assume that the solution is of the form

$$p(r, \phi, \theta) = R(r)\Phi(\phi)\Theta(\theta). \tag{3.3}$$

As shown in appendix B, with the above ansatz the Helmholtz equation in spherical coordinates splits into the following three homogeneous second order ordinary differential equations (ODE),

$$\frac{d^2\Phi}{d\phi^2} + \mu^2\Phi = 0 , \tag{3.4}$$

$$\frac{1}{\sin\theta}\frac{d}{d\theta}\left(\sin\theta\frac{d\Theta}{d\theta}\right) + \left[\nu\left(\nu+1\right) - \frac{\mu^2}{\sin^2\theta}\right]\Theta = 0 \,, \tag{3.5}$$

$$\frac{1}{r^2}\frac{d}{dr}\left(r^2\frac{dR}{dr}\right) + k^2R - \frac{\nu(\nu+1)}{r^2}R = 0 \,, \tag{3.6}$$

whereby ν and μ are arbitrary constants resulting from the separation. As we will see later in sections 3.2 and 3.3, the values of the parameters ν and μ are determined by the choice of boundary conditions and are real-valued for all types of boundary conditions considered within this thesis. It is easy to see that the above differential equations are unchanged when replacing μ by $-\mu$ or ν by $-\nu-1$. Accordingly, without loss of generality, the parameter ranges can be restricted to

$$\mu \geq 0,\ \mu \in \mathbb{R}, \tag{3.7}$$

$$\nu \geq -\tfrac{1}{2},\ \nu \in \mathbb{R}. \tag{3.8}$$

Equation (3.4) is a second order ODE with constant coefficients, eq. (3.5) is called the *associated Legendre* equation, and eq. (3.6) is known as the *spherical Bessel* equation. Since eqs. (3.4) to (3.6) are a second order ODEs, the general solution for each ODE is formed by a weighted sum of two linearly independent solutions, cf. [Kre99, Ch.2]. The choice of basis solutions is obviously not unique, as any pair of linearly independent solutions serves as a basis. However, there are certain pairs of standard solutions that are usually adopted as a basis.

General solution of eq. (3.4).   As a general solution of eq. (3.4) we choose

$$\Phi_\mu(\phi) = A\,\sin(\mu\phi) + B\,\cos(\mu\phi) \,, \tag{3.9}$$

where A, B, are the weights for a particular solution. Another popular choice is $\Phi_\mu(\phi) = A\,e^{i\mu\phi} + B\,e^{-i\mu\phi}$, however it is convenient to adopt real valued functions as a basis.

General solution of the associated Legendre equation.   The substitution $x := \cos(\theta)$ in eq. (3.5) yields the associated Legendre equation in standard form,

$$\left(1 - x^2\right)\frac{d^2\Theta}{dx^2} - 2x\frac{d\Theta}{dx} + \left(\nu(\nu+1) - \frac{\mu^2}{1 - x^2}\right)\Theta = 0. \tag{3.10}$$

Note that in general this differential equation is solved for unrestricted, complex-valued x, ν, μ, and the standard solutions are called associated Legendre functions, cf. [Olv74,

27

Ch.12; EMO+53, Ch.3]. We are interested in solutions of eq. (3.10), which are real valued on the interval $x \in [-1, 1]$, i.e. $\theta \in [0, \pi]$, for $\mu, \nu \in \mathbb{R}$. This is not necessarily the case for the associated Legendre functions. The standard solutions defined to fulfill these requirements are called *Ferrers functions* or *associated Legendre functions on the cut*, [Olv74, p. 186; DLMF, §14.3(i)], and yield

$$\mathsf{P}_\nu^\mu (x) = \left(\frac{1+x}{1-x}\right)^{\frac{\mu}{2}} \mathbf{F} \left(\begin{matrix} \nu+1, -\nu \\ 1-\mu \end{matrix}; \frac{1-x}{2}\right), \tag{3.11}$$

$$\mathsf{Q}_\nu^\mu (x) = \frac{\pi}{2\sin(\mu\pi)} \left[\cos(\mu\pi) \left(\frac{1+x}{1-x}\right)^{\frac{\mu}{2}} \mathbf{F} \left(\begin{matrix} \nu+1, -\nu \\ 1-\mu \end{matrix}; \frac{1-x}{2}\right) \right.$$
$$\left. - \frac{\Gamma(\nu+\mu+1)}{\Gamma(\nu-\mu+1)} \left(\frac{1-x}{1+x}\right)^{\frac{\mu}{2}} \mathbf{F} \left(\begin{matrix} \nu+1, -\nu \\ 1+\mu \end{matrix}; \frac{1-x}{2}\right)\right], \tag{3.12}$$

where $\Gamma(x)$ is the gamma function, and $\mathbf{F}\left(\begin{smallmatrix} a,b \\ c \end{smallmatrix}; x\right) = \frac{F\left(\begin{smallmatrix} a,b \\ c \end{smallmatrix}; x\right)}{\Gamma(c)}$ is Olver's hypergeometric function. Thereby $F\left(\begin{smallmatrix} a,b \\ c \end{smallmatrix}; x\right) = \sum_{l=0}^{\infty} \frac{(a)_l (b)_l}{(c)_l l!} x^l$ is Gauß' hypergeometric function, and *Pochhammer's symbol* (or *rising factorial*) is defined as $(a)_l = a(a+1)\dots(a+l-1) = \frac{\Gamma(a+l)}{\Gamma(a)}$, with $(a)_0 := 1$ and $l \in \mathbb{Z}^+$.

However, the Ferrers functions are not applicable as a pair of standard solutions for all possible values of ν and μ. On the one hand, $\mathsf{Q}_\nu^\mu (x)$ is undefined for $\nu + \mu = -1, -2, -3, \dots$, which is due to the gamma function in the denominator in eq. (3.12). This case is avoided by restricting the parameter values as in eqs. (3.7) and (3.8). On the other hand, $\mathsf{P}_\nu^\mu (x)$ and $\mathsf{Q}_\nu^\mu (x)$ are linearly dependent for $\nu - \mu = -1, -2, -3, \dots$, as their Wronskian is zero, cf. [DLMF, eq. 14.2.4],

$$\mathscr{W}\{\mathsf{P}_\nu^\mu(x), \mathsf{Q}_\nu^\mu(x)\} = \frac{\Gamma(\nu+\mu+1)}{\Gamma(\nu-\mu+1)(1-x^2)}. \tag{3.13}$$

As eq. (3.5) is unchanged by replacing μ with $-\mu$, clearly $\mathsf{P}_\nu^{-\mu}(x)$ is further solution. From the Wronskians, cf. [DLMF, eq. 14.2.6, eq. 14.2.7],

$$\mathscr{W}\left\{\mathsf{P}_\nu^{-\mu}(x), \mathsf{Q}_\nu^\mu(x)\right\} = \frac{\cos(\mu\pi)}{1-x^2}, \tag{3.14}$$

$$\mathscr{W}\left\{\mathsf{P}_\nu^{-\mu}(x), \mathsf{P}_\nu^\mu(x)\right\} = \frac{2\sin(\mu\pi)}{\pi(1-x^2)}, \tag{3.15}$$

it follows that $\mathsf{P}_\nu^{-\mu}(x)$, $\mathsf{Q}_\nu^\mu(x)$ are linearly independent for $\mu \neq \frac{1}{2}, \frac{3}{2}, \frac{5}{2}, \dots$, and $\mathsf{P}_\nu^{-\mu}(x)$, $\mathsf{P}_\nu^\mu(x)$ linearly independent for $\mu \neq 0, 1, 2, 3, \dots$

There is no single pair of standard solutions that can be used for all values of ν and μ. However it is feasible to let the choice of standard solutions for eq. (3.5) depend

on μ only. Therefore, we choose $\mathsf{P}_\nu^{-\mu}(\cos\theta)$ as one standard solution and, depending on μ, either $\mathsf{Q}_\nu^\mu(\cos\theta)$ or $\mathsf{P}_\nu^\mu(\cos\theta)$ as a second standard solution. Hence, the general solution of eq. (3.5) yields

$$\Theta_\nu^\mu(\theta) = C\,\mathsf{P}_\nu^{-\mu}(\cos\theta) + D \begin{cases} \mathsf{Q}_\nu^\mu(\cos\theta) & \text{for } \mu \neq \frac{1}{2}, \frac{3}{2}, \frac{5}{2}, \ldots, \\ \mathsf{P}_\nu^\mu(\cos\theta) & \text{for } \mu = \frac{1}{2}, \frac{3}{2}, \frac{5}{2}, \ldots, \end{cases} , \qquad (3.16)$$

where C, D, are the weights for a particular solution.

General solution of the spherical Bessel-equation. As a general solution of eq. (3.6) we choose

$$R_\nu(r) = E\,j_\nu(kr) + F\,h_\nu^{(2)}(kr), \qquad (3.17)$$

where E, F are the weights for a particular solution, and $j_\nu(kr)$, $h_\nu^{(2)}(kr)$ are the spherical Bessel function and the spherical Hankel function of the second kind, respectively.

Other popular choices are $R_\nu(r) = E\,j_\nu(kr) + F\,y_\nu(kr)$, with $y_\nu(kr)$ being the spherical Neumann function, or $R_\nu(r) = E\,h_\nu^{(1)}(kr) + F\,h_\nu^{(2)}(kr)$, with $h_\nu^{(1)}(kr)$ being the spherical Hankel function of the first kind. The choice of eq. (3.17) is convenient, as for an interior problem we achieve $F = 0$, and for a radiating problem we achieve $E = 0$, see section 2.2.1. A detailed derivation of the solution of eq. (3.6) is given in Appendix C.

3.2 Sturm-Liouville theory

The purpose of this section is to provide the reader with the basic properties of Sturm-Liouville problems. We will discuss the problems as far as they are relevant for this thesis. A more elaborate introduction into the theory of Sturm-Liouville problems can be found in the monograph by Anton Zettl [Zet05].

3.2.1 Sturm-Liouville problems

A Sturm-Liouville problem with self adjoint boundary conditions possesses mathematical properties similar to a Hermitian (or self-adjoint) matrix:

- The eigenvalues are all real.

- The eigenfunctions associated with distinct eigenvalues are orthogonal.

- The set of eigenfunctions forms a complete orthogonal basis

The Sturm-Liouville equation. Many second order ODEs can be written in Sturm-Liouville form,

$$\frac{d}{dx}\left[p(x)\frac{dy}{dx}\right] + \left[\lambda w(x) - q(x)\right] y = 0, \quad x \in (a,b), \tag{3.18}$$

where (a,b) is an open interval on $\mathbb{R}$, $\{p,q,w\}$ are the Sturm-Liouville coefficients and λ is a spectral parameter. We assume that the set of coefficients satisfies the following conditions[1], cf.[BEZ01]:

$$p, p', q, w \in C(a,b) \quad \text{and} \quad p(x), w(x) > 0 \quad \text{for all } x \in (a,b), \tag{3.19}$$

where $C(a,b)$ is the space of continuous functions on (a,b). Obviously, any solution y of eq. (3.18) has to be a two-times continuously differentiable function, i.e. $y(x) \in C^2(a,b)$. Furthermore, we require the solution to be square integrable[2], i.e. $y \in L^2(a,b)$ where $\int_a^b |f(x)|^2 dx < +\infty$ for all $f \in L^2(a,b)$.

The differential equations resulting from the separation of the Helmholtz equation in spherical coordinates, eqs. (3.4), (3.5) and (3.6) are put into Sturm-Liouville form by a simple variable substitution. These substitutions, the Sturm-Liouville coefficients p, q, w and the spectral parameter λ are listed in table 3.1 below.

equation	substitution	$p(x)$	$q(x)$	$w(x)$	λ
(3.4)	$x = \phi$	1	0	1	μ^2
(3.5)	$x = \cos(\theta)$	$1 - x^2$	$\mu^2/(1-x^2)$	1	$\nu(\nu+1)$
(3.6)	$x = r$	x^2	$\nu(\nu+1)$	x^2	k^2

Table 3.1: Transformation of eqs. (3.4), (3.5) and (3.6) in Sturm-Liouville form.

Self-adjoint problems. A self-adjoint Sturm-Liouville problem is determined by eq. (3.18) and a self-adjoint homogeneous two-point boundary condition at the endpoints a and b. A solution $y_i(x)$ of eq. (3.18) satisfying the boundary condition is called an *eigenfunction* and the according λ_i is called an *eigenvalue* of the problem.

---

[1] Note that there are weaker conditions, cf. [BEZ01], but the differential equations within this work fulfill eq. (3.19). The positive sign restriction on p and w is not necessary in general, but with this condition the eigenvalues are necessarily real.

[2] This requirement is necessary for self-adjoint problems. The concept of self-adjoint operators requires a inner product space, as shown in the next paragraph. Beyond mathematics, this requirement complies with the general assumption in physics that any system is of finite energy.

Defining the Sturm-Liouville differential operator as

$$\mathcal{L} := \frac{d}{dx}\left(p(x)\frac{d}{dx}\right) - q(x), \tag{3.20}$$

eq. (3.18) is denote in compact form by

$$\mathcal{L}y + \lambda w y = 0. \tag{3.21}$$

The adjoint operator of $\mathcal{L}$, denote by $\mathcal{L}^{\mathrm{H}}$, fulfills by definition [WA03; AlG08],

$$\langle \mathcal{L}f, g \rangle = \langle f, \mathcal{L}^{\mathrm{H}}g \rangle \quad \text{for all } f, g \in C^2(a,b) \cap L^2(a,b), \tag{3.22}$$

where $\langle f, g \rangle = \int_a^b f(x)\bar{g}(x)dx$ denotes the inner product, and the bar denotes the complex conjugate. The operator is said to be self adjoint if $\mathcal{L}^{\mathrm{H}} = \mathcal{L}$. With eq. (3.20) and applying integration by parts to the left side of eq. (3.22), it shows that

$$\langle \mathcal{L}f, g \rangle = \langle f, \mathcal{L}g \rangle + p\left[f'\bar{g} - f\bar{g}'\right]\Big|_a^b. \tag{3.23}$$

Hence, the operator is self-adjoint if $p\left[f'\bar{g} - f\bar{g}'\right]\Big|_a^b$ vanishes for all $f, g \in C^2(a,b) \cap L^2(a,b)$. Defining $[f,g](x) := p(x)\left[f'(x)\bar{g}(x) - f(x)\bar{g}'(x)\right]$, this condition can be written in compact form

$$[f,g](a) - [f,g](b) = 0. \tag{3.24}$$

In general, the above condition does not hold for all $f, g \in C^2(a,b) \cap L^2(a,b)$. This condition depends only on the behavior of the solutions f, g, their derivatives, and p at the endpoints a, b. It shows that eq. (3.24) is satisfied if f, g fulfill adequate boundary conditions. Such boundary conditions, under which the problem is self-adjoint, are called self-adjoint boundary conditions.

Orthogonality of eigenfunctions. The eigenfunctions of a self-adjoint Sturm-Liouville problem associated with distinct eigenvalues are orthogonal on the interval $x \in (a,b)$ with respect to the weight function $w(x)$ [WA03, p. 498],

$$\int_a^b y_i(x)\bar{y}_j(x)w(x)\,dx = 0, \text{ for } i \neq j. \tag{3.25}$$

It is a simple matter to verify the above equation. Inserting two distinct eigenfunctions $y_i(x) \neq y_j(x)$ in eq. (3.23) yields $\int_a^b (\mathcal{L}y_i \, \bar{y}_j - y_i \mathcal{L}\bar{y}_j) \, dx = 0$. Applying eq. (3.21) gives $(\lambda_i - \lambda_j) \int_a^b y_i \bar{y}_j w \, dx = 0$, and thus for $\lambda_i \neq \lambda_j$ the integral must vanish.

The eigenfunction y_i corresponding to the eigenvalue λ_i is unique, up to a scalar multiple. So we choose the eigenfunctions to be normalized

$$\int_a^b |y_i(x)|^2 w(x) \, dx = 1. \tag{3.26}$$

With this normalization, the sequence of eigenfunctions (y_i) forms an orthonormal set with respect to $w(x)$.

Note that in case of periodic boundary conditions two distinct eigenfunctions may correspond to the same eigenvalue. These two functions are not necessarily orthogonal but can always be orthogonalized, e.g. by Gram-Schmidt orthogonalization [WA03].

Completeness of eigenfunctions. The sequence of orthonormal eigenfunctions (y_i) forms a complete set in the weighted Hilbert space $L_w^2(a, b)$ with the weighted inner product $\langle f, g \rangle_w = \int\limits_a^b f(x)\bar{g}(x)w(x) \, dx$. Thus, for any $f \in L_w^2(a, b)$ the following relation holds,

$$\lim_{l \to \infty} \int_a^b \left[f - \sum_{i=0}^l \langle f, y_i \rangle_w \, y_i \right]^2 w \, dx = 0. \tag{3.27}$$

Proofs of the completeness relation are given e.g. in [AlG08, p.79; CH24, p.342; CL55, p.197; MF53, p. 738]. The above relation is equivalent to the identity

$$f = \sum_{i=0}^\infty \langle f, y_i \rangle_w \, y_i, \tag{3.28}$$

where equality holds in the sense of convergence in $L_w^2(a, b)$. Furthermore, eq. (3.27) is equivalent to Parseval's relation,

$$\int_a^b |f|^2 w \, dx = \sum_{i=0}^\infty |\langle f, y_i \rangle_w|^2. \tag{3.29}$$

If we denote the weighted inner product in integral form and interchange the order of summation and integration, eq. (3.28) writes as

$$f(x) = \int_a^b f(x') \left[\sum_{i=0}^\infty \bar{y}_i(x')y_i(x)w(x') \right] dx'. \tag{3.30}$$

Comparing this to the fundamental property of Dirac's delta distribution, i.e. $f(x) = \int_a^b f(x')\delta(x - x')dx'$, the following relation is evident,

$$w(x')\sum_{i=0}^{\infty} \bar{y}_i(x')y_i(x) = \delta(x - x').\tag{3.31}$$

Endpoint classification. The form of suitable self-adjoint boundary conditions depends on the interval (a, b) and the behavior of the Sturm-Liouville coefficients at the endpoints a and b. The following classification of endpoints for Sturm-Liouville problems is standard in literature, see e.g. [Zet05, p. 145], and useful for discussing distinct cases of possible self-adjoint boundary conditions.

Regular endpoint. The endpoint a is regular (R) if the Sturm-Liouville coefficients satisfy for any $c \in (a, b)$

$$p^{-1}, q, w \in L^1(a, c],\tag{3.32}$$

where $L^1(I)$ is the space of integrable functions on the interval I. It can be shown, cf. [Zet05, p. 27], that all solutions have finite limits at a regular endpoint and are bounded in the neighborhood. The endpoint a is singular (S) if it is not R. If a is S it is further classified in the following sub-cases.

Limit-circle endpoint. The endpoint a is *limit-circle* (LC) if a is S, and all solutions $y_i(x)$ of eq. (3.18) are square integrable towards a weighted by $w(x)$,

$$\int_a^c |y_i(x)|^2 w(x)dx < +\infty \quad \text{for all } c \in (a, b).\tag{3.33}$$

Limit-point endpoint. The endpoint a is *limit-point* (LP) if it is not LC, i.e. there exists at least one solutions $y_i(x)$ of eq. (3.18) such that

$$\int_a^c |y_i(x)|^2 w(x)dx = +\infty.\tag{3.34}$$

Let f, g be two arbitrary solutions of eq. (3.18), then if a is LP following equation holds

$$[f, g](a) = 0 \quad \text{for all } f, g \in L^2((a, b); w).\tag{3.35}$$

A proof is given in [Nai68, p. 78].

The endpoint b of the interval (a, b) is classified similarly into R, LC, and LP. Table 3.2 contains the endpoint classification for the differential equations resulting from the separation of the Helmholtz equation in spherical harmonics, eqs. (3.4) to (3.6). Classifications for many other classical differential equations are given e.g. in [Eve05].

Endpoint	Classification
$-\infty$	LP
$+\infty$	LP

(a)

Endpoint	Parameter	Classification
-1	$0 \le \mu < 1$	LC
-1	$1 \le \mu$	LP
$+1$	$0 \le \mu < 1$	LC
$+1$	$1 \le \mu$	LP

(b)

Endpoint	Parameter	Classification
0	$0 \le \nu < \frac{1}{2}$	LC
0	$\frac{1}{2} \le \nu$	LP
$+\infty$	$0 \le \nu < +\infty$	LP

(c)

Table 3.2: Endpoint classification for (a) the Fourier equation in $L^2(-\infty, +\infty)$, (b) the associated Legendre equation in $L^2(-1, +1)$, and (c) the spherical Bessel equation in $L^2(0, +\infty)$.

3.2.2 Boundary conditions for regular problems

In general, a boundary condition for a regular Sturm-Liouville problem is expressed by

$$
\begin{aligned}
\alpha_1 y(a) + \alpha_2 y'(a) + \alpha_3 y(b) + \alpha_4 y'(b) = 0, \\
\beta_1 y(b) + \beta_2 y'(b) + \beta_3 y(a) + \beta_4 y'(a) = 0,
\end{aligned}
\tag{3.36}
$$

where α_i, $\beta_i \in \mathbb{R}$ and $\sum_i |\alpha_i|^2 > 0$, $\sum_i |\beta_i|^2 > 0$, cf. [Rab72; AlG08, p. 44].

The necessary condition for the problem to be self-adjoint, eq. (3.24), can be reformulated in terms of the coefficients involved in the boundary condition. Inserting eq. (3.36) in eq. (3.24), we get after some rearrangements

$$
p(a)\,(\alpha_3\beta_2 - \alpha_4\beta_1) = p(b)\,(\alpha_1\beta_4 - \alpha_2\beta_3)\,.
\tag{3.37}
$$

The general form of regular boundary conditions, eq. (3.36), has several special

cases. In the following we will discuss two of those, which are of special interest for this work. These are separated and periodic boundary conditions. A more detailed discussion of self-adjoint boundary conditions can be found in [BEZ01; Zet05].

Separated boundary conditions. The general boundary condition, eq. (3.36), reduces to a separated one by setting $\alpha_3 = \alpha_4 = \beta_3 = \beta_4 = 0$,

$$\alpha_1 \, y(a) + \alpha_2 \, y'(a) = 0,$$
$$\beta_1 \, y(b) + \beta_2 \, y'(b) = 0, \tag{3.38}$$

Such boundary conditions are called separated as one condition involves values of y and y' at the endpoint $x = a$, only, while the other condition involves only values at the endpoint $x = b$. Otherwise the boundary conditions are called coupled. A problem with separated boundary conditions satisfies eq. (3.24) for arbitrary choices of the coefficients $\alpha_{1,2}$, $\beta_{1,2}$ and is hence self-adjoint.

A Sturm-Liouville problem with separated boundary conditions possesses an infinite, but discrete, sequence of eigenvalues, which is bounded below. The eigenvalues can be ordered and index to satisfy $-\infty < \lambda_0 < \lambda_1 < \ldots < \lambda_i < \ldots$, with $\lambda_i \to \infty$ as $i \to \infty$, cf. [Zet05, p. 209]. Hence, there is only a finite number of negative eigenvalues.

Each eigenvalue λ_i is simple, i.e. it is associated with a single eigenfunction y_i, which is uniquely determined up to a constant factor. This eigenfunction has exactly i zeros in the open interval $x \in (a, b)$. Furthermore, the eigenvalues are all nonnegative if the following conditions are satisfied, cf. [Rab72, p.258]:

$$\alpha_1\alpha_2 \leq 0, \qquad \beta_1\beta_2 \geq 0,$$
$$q(x) \geq 0 \quad \text{for } x \text{ in } [a, b]. \tag{3.39}$$

A proof is given in appendix D.

Homogeneous Dirichlet and Neumann boundary conditions. There are two special cases of separated boundary conditions, which are of particular interest within this work. The *Dirichlet* boundary condition specifies solely the values of the solution at endpoint a or b, i.e. $\alpha_2 = 0$ or $\beta_2 = 0$ in eq. (3.38). The *Neumann* boundary condition solely specifies the values of the derivative of the solution at endpoint a or b, i.e. $\alpha_1 = 0$ or $\beta_1 = 0$ in eq. (3.38). If $q(x) \geq 0$ for x in $[a, b]$ then eq. (3.39) holds for both, *Dirichlet* and *Neumann* boundary conditions. This immediately implies that all eigenvalues are non-negative.

35

Periodic boundary conditions. With $\alpha_1 = -\alpha_3$, $\beta_2 = -\beta_4$, and $\alpha_2 = \alpha_4 = \beta_1 = \beta_3 = 0$, eq. (3.36) reduces to periodic boundary conditions,

$$
\begin{aligned}
y(a) &= y(b), \\
y'(a) &= y'(b).
\end{aligned}
\tag{3.40}
$$

For such boundary conditions eq. (3.24) is satisfied for $p(a) = p(b)$, and in this case the Sturm-Liouville problem is self-adjoint. In contrast to the separated boundary conditions, this is an example for coupled boundary conditions.

The eigenvalues form a discrete sequence $-\infty < \lambda_0 \leq \lambda_1 \leq \ldots \leq \lambda_i \leq \ldots$ with $\lambda_i \to \infty$ as $i \to \infty$. In contrast to the eigenvalues of a problem with separated boundary conditions, the eigenvalues may be simple or double. A double eigenvalue $\lambda_i = \lambda_j$ is associated with two linearly independent eigenfunctions $y_i \neq y_j$. If $q(x) \geq 0$ for x in $[a, b]$ then all eigenvalues are non-negative, cf. appendix D.

3.2.3 Boundary conditions for singular problems

In general, any combination of R, LC, and LP endpoints is possible. The case of both endpoints regular was discussed in the previous subsection. A Sturm-Liouville problem is said to be *singular* if at least one of the endpoints a or b is not regular. As in the regular case, the boundary conditions may be separated or coupled. However, coupled boundary conditions are only possible if non of the endpoints is LP.

In the following we will discuss only separated singular boundary conditions, which are of special interest within this thesis. Hence, it is sufficient to investigate the boundary condition at each endpoint of the interval (a, b) separately. The problem is self-adjoint if the condition

$$
[f, g](d) = 0
\tag{3.41}
$$

is met for all solutions f, g that satisfy the boundary condition at the endpoint $d = a$ and $d = b$. Together with the separated regular boundary conditions at a and/or b, eq. (3.38), all possible combinations of R, LC, and LP endpoints are covered.

LP endpoints. If d is LP, the two-point boundary condition is vacuous at this endpoint. This follows directly from eq. (3.35) as eq. (3.41) is fulfilled for all solutions $f, g \in L^2((a, b); w)$ of eq. (3.18). Thus only at the non-LP endpoint a boundary condition is posed. No boundary condition is necessary if both endpoints are LP.

36

Furthermore, if both endpoints a, b are LP, $q(x) \geq 0$ for $x \in [a, b]$, and there exist a *principal* solution at both endpoints for all λ, the Sturm-Liouville problem possesses an infinite, discrete series of non-negative, simple eigenvalues, i.e. $0 \leq \lambda_0 < \lambda_1 < \ldots < \lambda_i < \ldots$ with $\lambda_i \to \infty$ as $i \to \infty$. The same holds true if one endpoint is LP and there exist a *principal* solution for all λ at this endpoint, while the other endpoint is either R and eq. (3.39) holds at this endpoint, or it is LC and eq. (3.46) holds at this endpoint. A proof can be found in appendix D.

Principal and non-principal solutions. For a certain λ, the solution $u(x)$ of eq. (3.18) is referred to as the *principal* solution at the singular endpoint d for this value of λ, if

$$\lim_{x \to d} \frac{u(x)}{v(x)} = 0, \tag{3.42}$$

where $v(x)$ is any solution, which is linearly independent to $u(x)$, cf. [Zet05, p. 131; Olv74, p. 155]; $v(x)$ is referred to as a *non-principal* solution. This means that at the endpoint the principal solution is recessive[3], while the non-principal solution is dominant. Clearly, the principle solution is unique up to scalar multiples, while the non-principal solution is not unique. Note that the attributes *principal* and *non-principal* are tied to the singular endpoint under consideration, i.e. a principal solution at the singular endpoint a may be non-principal at the singular endpoint b and vice versa.

LC endpoints. If d is LC then the boundary condition at this endpoint takes the form

$$\alpha_1[y, u](d) + \alpha_2[y, v](d) = 0, \tag{3.43}$$

where $\alpha_{1,2} \in \mathbb{R}$ with $|\alpha_1|^2 + |\alpha_2|^2 > 0$, and $\{u, v\}$ are a real, linearly independent basis of solutions of eq. (3.18) with $[u, v](d) \neq 0$. Such pairs always exists if d is LC, see [BEZ01; Zet05], and are called boundary condition basis at the endpoint d. If both endpoints are LC, the bases are in general different at the two endpoints.

It is common practice to choose $\{u, v\}$ such that u is the *principal* solution and v is any *non-principal* solution of eq. (3.18) at d for some eigenvalue λ_i, see [BEZ01; Eve05]. Clearly such a boundary condition basis is not unique. However, boundary conditions expressed by $\{u, v\}$ and $\alpha_{1,2}$ can be equivalently expressed by any other

---

[3]The terms *recessive* and *dominant* solution are used alternatively for *principal* and *non-principal* solution, e.g. in the monograph of Frank Olver [Olv74].

basis $\{\tilde{u}, \tilde{v}\}$ and $\tilde{\alpha}_{1,2}$, see [Zet05, p. 185].

Table 3.3 contains the boundary condition bases for the associated Legendre equation, eq. (3.5), and the spherical Bessel equation, eq. (3.6). These can be found[4] in [Eve05] as well as bases for many other classical differential equation.

If each endpoint is either R or LC and the boundary conditions are separated, then the eigenvalues are simple, discrete and bounded below, i.e. $-\infty < \lambda_0 < \lambda_1 < \ldots < \lambda_i < \ldots$, with $\lambda_i \to \infty$ as $i \to \infty$, cf. [Zet05, p. 209].

Parameter	u	v
$\mu = 0$	1	$\ln\left(\dfrac{1+x}{1-x}\right)$
$0 < \mu < 1$	$(1-x^2)^{\frac{\mu}{2}}$	$(1-x^2)^{-\frac{\mu}{2}}$

(a)

Parameter	u	v
$0 \leq \nu < \frac{1}{2}$	x^ν	$x^{-\nu-1}$

(b)

Table 3.3: Boundary condition basis for (a) the associated Legendre equation for the endpoints ± 1, and (b) the spherical Bessel equation for the endpoint 0.

Friedrichs boundary condition. It is named after K. Friedrichs, who termed this boundary condition "ausgezeichnet" in his article [Fri36]. For many classical differential equations, like for the Legendre and Bessel equation, see table 3.2, the LP/LC classification of the singular endpoints depends on a parameter. Friedrichs' intention was to single out a boundary condition for the LC case, which is automatically fulfilled if the endpoint is LP. In singular eigenvalue problems of mathematical physics this boundary condition is almost always implicitly applied [Rel50, p. 344]. However, it seems that there is no explicit physical interpretation.

The Friedrichs boundary condition is a special case of eq. (3.43) with $\alpha_2 = 0$ and u being a principal solution of the differential equation for some value of λ,

$$[y, u](d) = 0. \tag{3.44}$$

It can be shown that if f is a principal solution at d for some eigenvalue λ_i and g is a solution for a possibly different eigenvalue λ_j, then, cf. [MP95, Lemma 4],

$$[f, g](d) \begin{cases} = 0 & \text{if } g \text{ is a principal solution at } d, \\ \neq 0 & \text{if } g \text{ is a non-principal solution at } d. \end{cases} \tag{3.45}$$

---

[4]Note that the boundary condition basis for the spherical Bessel equation is achieved from the basis of the Bessel equation in Liouville form, see [Eve05, p.15], by substituting $\hat{y} = xy$ and $\hat{\nu} = \nu + \frac{1}{2}$.

Thus the Friedrichs boundary condition is fulfilled only by solutions that are principal at the singularity. Note that the Friedrichs boundary condition is independent of the choice of λ, for which u is the principal solution.

Furthermore, if both endpoints a, b are LC, $q(x) \geq 0$ for $x \in [a, b]$, and the following conditions hold,

$$
\begin{aligned}
\frac{p(a)u'(a)}{u(a)} &\geq 0, \\
\frac{p(b)u'(b)}{u(b)} &\leq 0,
\end{aligned}
\tag{3.46}
$$

then all eigenvalues are non-negative. The same holds true if one endpoint is LC while the other endpoint is either R and eq. (3.39) holds at this endpoint, or it is LP and there exist a *principal* solution at this endpoints for all λ. A proof can be found in appendix D.

3.3 Eigenfunctions of the Helmholtz equation with angular boundary conditions

As shown in the previous section, a complete set of orthogonal eigenfunctions emerge naturally as solution of a self-adjoint Sturm-Liouville problem. The differential equations arising from the separation of the Helmholtz equation in spherical coordinates can be brought in Sturm-Liouville form. Together with homogeneous two-point boundary conditions, complete orthogonal sets are achieved for each differential equation.

The boundary conditions are specified for each differential equation and thus for each coordinate separately. Setting one coordinate to a constant value, without any restriction on the remaining two coordinates, yields a coordinate surface. Figure 3.1[5] shows the coordinate surfaces in spherical coordinates. A constant value of ϕ yields a vertical half-plane, and a constant value of θ yields a semi-infinite cone, whose tip is located at the origin and whose axis of rotation coincides with the z-axis. At these surfaces the boundary conditions are specified, and they represent the boundaries of the domain where the corresponding set of eigenfunctions is valid. Thereby the boundary conditions specify the acoustical properties of these planes.

Within this work we only discuss Dirichlet/Neumann boundary conditions as

---

[5]Figure reprinted from [Wik17]
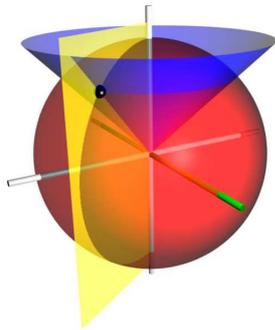
Figure 3.1: Coordinate surfaces in spherical coordinates; the yellow half-plane corresponds to $\phi = \mathrm{constant}$, the blue semi-infinite cone corresponds to $\theta = \mathrm{constant}$, and the red sphere corresponds to $r = \mathrm{constant}$.

well as boundary conditions, which result from the range of spherical coordinates. Physically, a Dirichlet boundary condition represents a sound-soft surface and a Neumann boundary condition represents a sound-hard surface, respectively.

In absence of a boundary surface, the boundary conditions result from the range of spherical coordinates. If there is no boundary surface in ϕ the boundary condition is a periodic one, with a periodicity of 2π, as the sound pressure and its derivative are required to be continuous. In absence of a boundary surface in θ, the boundary conditions are singular ones at $\theta = 0$ and $\theta = \pi$. If only a boundary surface at $\theta = \theta_1$ is specified, then the remaining boundary condition is a singular one at either $\theta = 0$ or $\theta = \pi$, depending on whether the domain above or below the semi-infinite cone is considered.

In the following subsections we discuss the eigenfunctions of the ordinary differential equation arising from the separation of the Helmholtz equation in spherical coordinates for angular boundary conditions in ϕ or θ.

3.3.1 Boundary conditions in ϕ

Equation (3.4) is the differential equation for the azimuth coordinate ϕ with the general solution given in eq. (3.9). This differential equation together with a homogeneous two-point boundary condition at ϕ_1 and ϕ_2, with $0 \leq \phi_1 \leq \phi_2 \leq 2\pi$, constitutes a Sturm-Liouville problem.

The boundary conditions are either separated Dirichlet/Neumann boundary conditions, corresponding to one or two sound-soft/-hard vertical half-planes, cf. fig. 3.2, or periodic boundary conditions in absence of a boundary surface. As discussed in section 3.2.2, such problems exhibit an infinite, but discrete set of real eigenvalues $\lambda_i = \mu_i^2$. Furthermore, putting eq. (3.4) in Sturm-Liouville form, see table 3.1, it is
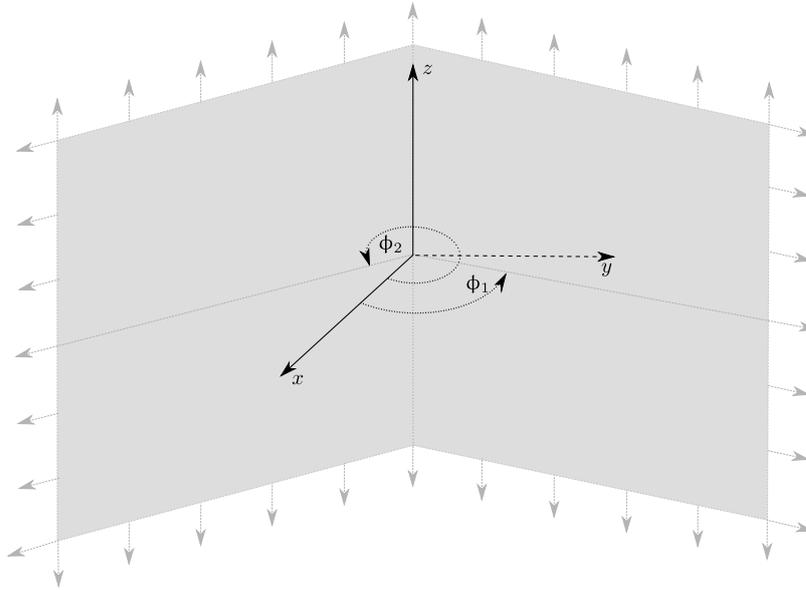
Figure 3.2: Half-planes corresponding to a two-point boundary condition at $\phi = \phi_{1,2}$.

seen that $q(\phi) \geq 0$ and thus all eigenvalues are non-negative. Hence the parameter μ_i is real, and we restrict $\mu_i \geq 0$ by convention.

The associated eigenfunctions $\Phi_{\mu_i}(\phi)$ form a complete orthogonal basis on the interval $\phi \in [\phi_1, \phi_2]$. The eigenfunctions can always be normalized such that the following relations holds,

$$\int_{\phi_1}^{\phi_2} \Phi_{\mu_i}(\phi)\Phi_{\mu_{i'}}(\phi)d\phi = \delta_{ii'}. \tag{3.47}$$

Separated boundary conditions in ϕ. Specifying boundary conditions at ϕ_1 and ϕ_2 geometrically corresponds to two infinite vertical half-planes as sketched in fig. 3.2. In the following we will discuss the eigenfunctions for sound-soft (Dirichlet) and sound-hard (Neumann) boundary conditions.

Dirichlet boundary conditions. The eigenfunctions $\Phi_{\mu_i}(\phi)$ of eq. (3.4) fulfilling Dirichlet boundary conditions at $\phi_{1,2}$,

$$\Phi_{\mu_i}(\phi)\Big|_{\phi=\phi_{1,2}} = 0,$$

are determined by applying the boundary conditions to the general solution eq. (3.9). This yields a pair of equations and written in matrix form we get

$$
\begin{bmatrix}
\sin(\mu_i\phi_1) & \cos(\mu_i\phi_1) \\
\sin(\mu_i\phi_2) & \cos(\mu_i\phi_2)
\end{bmatrix}
\begin{bmatrix}
A_i \\
B_i
\end{bmatrix} = 0. \tag{3.48}
$$

The above equation only has a non-trivial solution, i.e. $|A_i|+|B_i| \neq 0$, if the determinant of the involved matrix is zero. Calculating this determinant, and equating it to zero yields

$$
\sin(\mu_i(\phi_2 - \phi_1)) = 0. \tag{3.49}
$$

Obviously, the above condition is fulfilled for $\mu_i = \frac{\pi i}{\phi_2 - \phi_1}$, with $i = 0, 1, 2, 3, \ldots, \infty$. For these values of μ_i, the rank of the matrix in eq. (3.48) equals 1. From the rank-nullity theorem[6] we know that there exists only one arbitrary scaled vector $\left[A_i, B_i\right]^{\mathrm{T}} = N \left[\cos(\mu_i\phi_1), -\sin(\mu_i\phi_1)\right]^{\mathrm{T}}$, $N \in \mathbb{R}$ fulfilling eq. (3.48). Choosing $A_i = \sqrt{\frac{2}{\phi_2 - \phi_1}} \cos(\mu_i\phi_1)$ and $B_i = -\sqrt{\frac{2}{\phi_2 - \phi_1}} \sin(\mu_i\phi_1)$, the eigenfunctions yield

$$
\Phi_{\mu_i}(\phi) = \sqrt{\frac{2}{\phi_2 - \phi_1}} \sin\left(\frac{\pi i}{\phi_2 - \phi_1}(\phi - \phi_1)\right). \tag{3.50}
$$

The factor $\sqrt{\frac{2}{\phi_2 - \phi_1}}$ is included for normalization such that relation eq. (3.47) holds. Note that the eigenfunction for $i = 0$ is the zero function $\Phi_{\mu_0}(\phi) = 0$. Hence the set of eigenfunctions is complete for $i = 1, 2, \ldots, \infty$.

Neumann boundary conditions. Applying Neumann boundary conditions,

$$
\left.\frac{d\Phi_{\mu_i}(\phi)}{d\phi}\right|_{\phi=\phi_{1,2}} = 0,
$$

to the general solution eq. (3.9) yields

$$
\begin{bmatrix}
-\cos(\mu_i\phi_1) & \sin(\mu_i\phi_1) \\
-\cos(\mu_i\phi_2) & \sin(\mu_i\phi_2)
\end{bmatrix}
\begin{bmatrix}
A_i \\
B_i
\end{bmatrix} = 0. \tag{3.51}
$$

Equating the determinant of the above matrix to zero yields the same condition as in case of Dirichlet conditions, see eq. (3.49), and thus to the same values $\mu_i = \frac{\pi i}{\phi_2 - \phi_1}$, with $i = 0, 1, 2, \ldots, \infty$. We choose $A_i = \sqrt{\frac{2-\delta_i}{\phi_2 - \phi_1}} \cos(\mu_i\phi_1)$, $B_i = \sqrt{\frac{2-\delta_i}{\phi_2 - \phi_1}} \sin(\mu_i\phi_1)$,

---

[6]This theorem states that the rank and the nullity of a matrix add up to the number of columns [Mey00], whereby nullity refers to the dimensions of the null space of the matrix.

and the eigenfunctions yield

$$\Phi_{\mu_i}(\phi) = \sqrt{\frac{2-\delta_i}{\phi_2-\phi_1}} \cos\left(\frac{\pi i}{\phi_2-\phi_1}(\phi - \phi_1)\right). \tag{3.52}$$

These eigenfunctions form an orthonormal basis for $\phi \in [\phi_1, \phi_2]$ such that eq. (3.47) holds and fulfill Neumann boundary conditions at both endpoints.

Periodic boundary conditions in ϕ. In contrast to separated boundary conditions, in this case there are no local boundary surfaces where the values of the field quantities take specified values. The natural periodicity of the azimuth coordinate is 2π. Thus for a sound field with no specified local boundary in ϕ the field quantities are required to be continuous and smooth. This claim is identical to a periodic boundary condition where the solution and its derivative are demanded to be periodic functions with a period of 2π. For completeness, the derivation in the following is done for a general periodic boundary condition,

$$\begin{aligned} \Phi_{\mu_i}(\phi_1) &= \Phi_{\mu_i}(\phi_2), \\ \frac{d\Phi_{\mu_i}(\phi_1)}{d\phi} &= \frac{d\Phi_{\mu_i}(\phi_2)}{d\phi}, \end{aligned} \tag{3.53}$$

whereby the periodicity of 2π is a special case with $\phi_1 = 0$ and $\phi_2 = 2\pi$.

Applying these conditions, to the general solution eq. (3.9) yields the following linear system

$$\begin{bmatrix} \sin(\mu_i\phi_1) - \sin(\mu_i\phi_2) & \cos(\mu_i\phi_1) - \cos(\mu_i\phi_2) \\ \cos(\mu_i\phi_2) - \cos(\mu_i\phi_1) & \sin(\mu_i\phi_1) - \sin(\mu_i\phi_2) \end{bmatrix} \begin{bmatrix} A_i \\ B_i \end{bmatrix} = 0. \tag{3.54}$$

Equating the determinant of the above matrix to zero yields

$$\cos(\mu_i(\phi_2 - \phi_1)) = 1, \tag{3.55}$$

which is fulfilled for $\mu_i = \frac{2\pi i}{\phi_2-\phi_1}$, with $i = 0, 1, 2, 3, \ldots, \infty$. For these values of μ_i the matrix in eq. (3.54) becomes the zero matrix. Hence its rank is zero and there are two linearly independent coefficient vectors $\left[A_{i_{1,2}}, B_{i_{1,2}}\right]^{\mathrm{T}}$ fulfilling eq. (3.54). Thus there are two eigenfunctions associated with one eigenvalue. Choosing $A_{i_1} = \sqrt{\frac{2}{\phi_2-\phi_1}}$, $B_{i_1} = 0$ and $A_{i_2} = 0$, $B_{i_2} = \sqrt{\frac{2-\delta_i}{\phi_2-\phi_1}}$ the eigenfunctions yield

$$\Phi_{\mu_{i_1}}(\phi) = \sqrt{\frac{2}{\phi_2 - \phi_1}} \sin\left(\frac{2\pi i}{\phi_2 - \phi_1}\phi\right),$$

$$\Phi_{\mu_{i_2}}(\phi) = \sqrt{\frac{2 - \delta_i}{\phi_2 - \phi_1}} \cos\left(\frac{2\pi i}{\phi_2 - \phi_1}\phi\right). \tag{3.56}$$

Eigenfunctions associated with the same eigenvalue are not necessarily orthogonal, but always can be chosen to be orthogonal, cf. [Zet05, p.207]. In this case they are already orthogonal; and the eigenfunctions form a complete biorthonormal basis for $\phi \in [\phi_1, \phi_2]$ such that the following relations hold:

$$\int_{\phi_1}^{\phi_2} \Phi_{\mu_{i_1}}(\phi)\Phi_{\mu_{i'_1}}(\phi)d\phi = \delta_{ii'}, \tag{3.57}$$

$$\int_{\phi_1}^{\phi_2} \Phi_{\mu_{i_2}}(\phi)\Phi_{\mu_{i'_2}}(\phi)d\phi = \delta_{ii'}, \tag{3.58}$$

$$\int_{\phi_1}^{\phi_2} \Phi_{\mu_{i_1}}(\phi)\Phi_{\mu_{i'_2}}(\phi)d\phi = 0. \tag{3.59}$$

Note that one eigenfunction for $i = 0$ is the zero function $\Phi_{\mu_{0_1}}(\phi) = 0$ and thus the eigenvalue μ_0^2 is single whereas the eigenvalues μ_i^2 for $i \neq 0$ are double.

3.3.2 Boundary conditions in θ

The associated Legendre equation, eq. (3.5), is the differential equation for the zenith angle θ. This differential equation together with a homogeneous two-point boundary condition at θ_1 and θ_2, with $0 \leq \theta_1 \leq \theta_2 \leq \pi$, constitutes a Sturm-Liouville problem. The boundary conditions are either one of the following:

- Separated Dirichlet/Neumann boundary conditions, corresponding to a sound-soft/-hard infinite double cone, cf. fig. 3.3a.

- A Dirichlet/Neumann boundary condition at θ_1 and a singular boundary condition, corresponding to a sound-soft/-hard semi-infinite cone, cf. fig. 3.3b. Thereby the singular boundary condition is either posed at $\theta = 0$ or $\theta = \pi$, depending on whether the domain above or below the semi-infinite cone is considered.

- A singular boundary condition at $\theta = 0$ and $\theta = \pi$, if there is no boundary surface in θ.

As discussed in section 3.2.3, such problems exhibit an infinite but discrete set of simple real non-negative eigenvalues $\lambda_i = \nu_i(\nu_i + 1)$, if
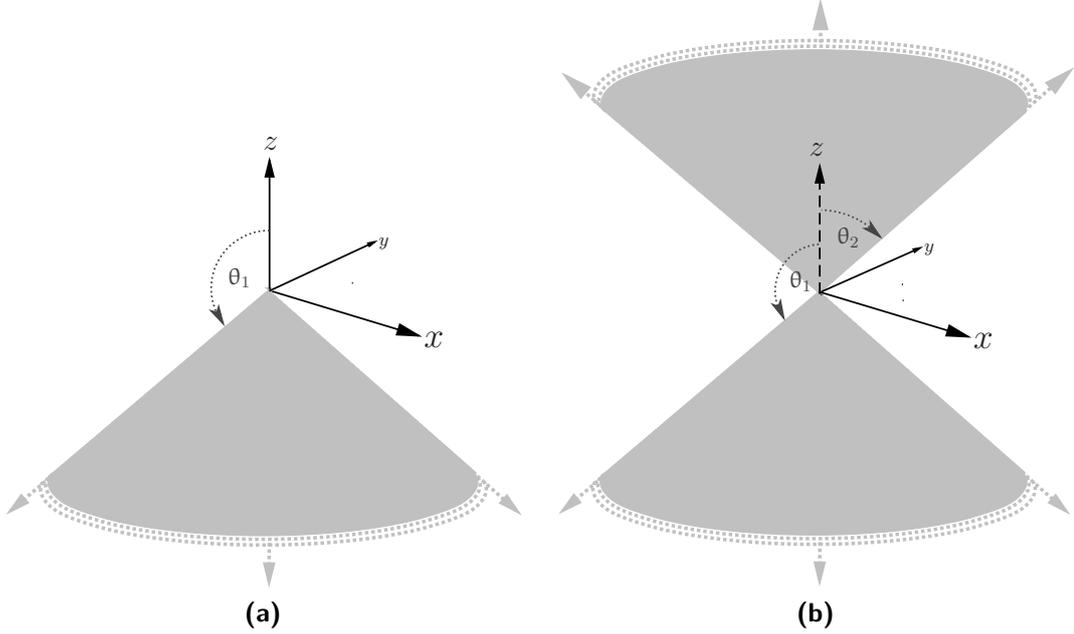
Figure 3.3: (a) semi-infinite cone and (b) infinite double cone.

1. the Sturm-Liouville parameter $q(\cos(\theta)) \geq 0$ and

2. depending on the endpoint classification, cf. table 3.2b,

    (a) there is a Dirichlet/Neumann boundary condition at a R end point, or

    (b) there exists a principal solution at a LP end point, or

    (c) eq. (3.46) holds in case of a LC end point.

The parameter μ is inherited from the Sturm-Liouville problem in ϕ and, as discussed in section 3.3.1, it is real-valued and non-negative. Thus the first condition is met in any case since $q(\cos(\theta)) = \frac{\mu^2}{\sin^2(\theta)}$, cf. table 3.1. For a regular end point the second condition is also met, since we consider only Dirichlet and Neumann boundary conditions.

In case of a LP end point it shows that there exist a principal solution at both singular points $\theta = 0$ and $\theta = \pi$ for any real μ. With $\mu \geq 0$ the principal solution at $\theta = 0$ is $\mathsf{P}_\nu^{-\mu}(\cos\theta)$, cf. [DLMF, §14.2(iii)]. As eq. (3.5) is unchanged when replacing θ by $\pi - \theta$, clearly $\mathsf{P}_\nu^{-\mu}(-\cos\theta)$ is also a solution, and obviously this is the principal solution at $\theta = \pi$.

The singular endpoints are LC for $0 \leq \mu < 1$, and it shows that the left side of eq. (3.46) vanishes for $a = 0$ and $b = \pi$, cf. tables 3.1 and 3.3a. Hence the third condition is also met.

The above consideration proof that the eigenvalues, and thus $\nu_i(\nu_i + 1)$, are non-negative in any case considered within this work. This implies $\nu_i \in (-\infty, -1] \cup [0, \infty)$, and narrows the restriction of ν in eq. (3.8) to

$$\nu \geq 0, \nu \in \mathbb{R}. \tag{3.60}$$

.

The associated eigenfunctions of the Legendre differential equation together with the above described boundary conditions form a complete orthogonal basis on the interval $\theta \in [\theta_1, \theta_2]$. For the normalized eigenfunction $\Theta^\mu_{\nu_i}(\theta)$, the following relation holds,

$$\int_{\theta_1}^{\theta_2} \Theta^\mu_{\nu_i}(\theta) \Theta^\mu_{\nu_{i'}}(\theta) \sin\theta d\theta = \delta_{ii'}. \tag{3.61}$$

The general solution of the Legendre equation is given in eq. (3.16). For a shorter notation we define

$$\mathbb{Q}^\mu_\nu(\cos\theta) := \begin{cases} \mathsf{Q}^\mu_\nu(\cos\theta) & \text{for } \mu \neq \frac{1}{2}, \frac{3}{2}, \frac{5}{2}, \ldots \\ \mathsf{P}^\mu_\nu(\cos\theta) & \text{for } \mu = \frac{1}{2}, \frac{3}{2}, \frac{5}{2}, \ldots \end{cases} . \tag{3.62}$$

Therewith eq. (3.16) is expressed by

$$\Theta^\mu_\nu(\theta) = C\,\mathsf{P}^{-\mu}_\nu(\cos\theta) + D\,\mathbb{Q}^\mu_\nu(\cos\theta). \tag{3.63}$$

Separated boundary conditions in θ. Specifying Dirichlet or Neumann boundary conditions at θ_1 and θ_2 geometrically corresponds to a sound-soft or sound-hard infinite double-conical surface, as sketched in fig. 3.3.

Dirichlet boundary conditions. Applying Dirichlet boundary conditions,

$$\Theta^\mu_{\nu_i}(\theta)\Big|_{\theta=\theta_{1,2}} = 0, \tag{3.64}$$

to the general solution eq. (3.63) yields

$$\begin{bmatrix} \mathsf{P}^{-\mu}_{\nu_i}(\cos\theta_1) & \mathbb{Q}^\mu_{\nu_i}(\cos\theta_1) \\ \mathsf{P}^{-\mu}_{\nu_i}(\cos\theta_2) & \mathbb{Q}^\mu_{\nu_i}(\cos\theta_2) \end{bmatrix} \begin{bmatrix} C_i \\ D_i \end{bmatrix} = 0. \tag{3.65}$$

Equating the determinant of the above matrix to zero yields the following condition

$$\mathsf{P}^{-\mu}_{\nu_i}(\cos\theta_1)\mathsf{Q}^{\mu}_{\nu_i}(\cos\theta_2) - \mathsf{P}^{-\mu}_{\nu_i}(\cos\theta_2)\mathsf{Q}^{\mu}_{\nu_i}(\cos\theta_1) = 0. \qquad (3.66)$$

To determine the values ν_i, for which the above condition is met, corresponds to the zeros of the term on the left side of the above equation with respect to ν. Within this work, the zeros are determined numerically by a root-finding algorithm[7].

Note that the zeros of the associate Legendre functions with respect to the order were determined by similar numerical algorithms in [HC97; Bau86]. In [Van07] a system of algebraic equations for the zeros of the associated Legendre functions is presented, but the method requires the solution of a nonlinear system of coupled differential equations.

As all eigenvalues are simple, the rank of the matrix in eq. (3.65) is always equal to 1, and there exists only one arbitrary scaled vector,

$$\left[C_i, D_i\right]^{\mathrm{T}} = N\left[\mathsf{Q}^{\mu}_{\nu_i}(\cos\theta_1), -\mathsf{P}^{-\mu}_{\nu_i}(\cos\theta_1)\right]^{\mathrm{T}}, \qquad (3.67)$$

with $N \in \mathbb{R}$, fulfilling eq. (3.65). Inserting these values for the weights C and D in eq. (3.63), the eigenfunctions yield

$$\Theta^{\mu}_{\nu_i}(\theta) = N^{\mu}_{\nu_i}\left[\mathsf{Q}^{\mu}_{\nu_i}(\cos\theta_1)\,\mathsf{P}^{-\mu}_{\nu_i}(\cos\theta) - \mathsf{P}^{-\mu}_{\nu_i}(\cos\theta_1)\mathsf{Q}^{\mu}_{\nu_i}(\cos\theta)\right], \qquad (3.68)$$

whereby $N^{\mu}_{\nu_i}$ is chosen such that $\int_{\theta_1}^{\theta_2}\left(\Theta^{\mu}_{\nu_i}(\theta)\right)^2\sin\theta d\theta = 1$.

For the determination of the normalization constant $N^{\mu}_{\nu_i}$, the definite integral $\int_{\theta_1}^{\theta_2}\left[\mathsf{Q}^{\mu}_{\nu_i}(\cos\theta_1)\,\mathsf{P}^{-\mu}_{\nu_i}(\cos\theta) - \mathsf{P}^{-\mu}_{\nu_i}(\cos\theta_1)\mathsf{Q}^{\mu}_{\nu_i}(\cos\theta)\right]^2\sin\theta\,d\theta$ needs to be evaluated. This may be done either numerically or, similar to [Smy50, p.156], a closed-form expression can be derived. However, this closed-form expression involves parameter derivatives of the associated Legendre functions with respect to ν.

Neumann boundary conditions. Applying Neumann boundary conditions,

$$\left.\frac{d\Theta^{\mu}_{\nu_i}(\theta)}{d\theta}\right|_{\theta=\theta_{1,2}} = 0, \qquad (3.69)$$

---

[7]We used the MATLAB function *fzero*, which uses a combination of bisection, secant, and inverse quadratic interpolation methods.

to the general solution eq. (3.16) yields

$$
\begin{bmatrix}
\left.\dfrac{d\,\mathsf{P}_{\nu_i}^{-\mu}(\cos\theta)}{d\theta}\right|_{\theta=\theta_1} & \left.\dfrac{d\mathbb{Q}_{\nu_i}^{\mu}(\cos\theta)}{d\theta}\right|_{\theta=\theta_1} \\[2ex]
\left.\dfrac{d\,\mathsf{P}_{\nu_i}^{-\mu}(\cos\theta)}{d\theta}\right|_{\theta=\theta_2} & \left.\dfrac{d\mathbb{Q}_{\nu_i}^{\mu}(\cos\theta)}{d\theta}\right|_{\theta=\theta_2}
\end{bmatrix}
\begin{bmatrix} C_i \\ D_i \end{bmatrix} = 0.
\tag{3.70}
$$

Equating the determinant of the above matrix to zero yields

$$
\left.\frac{d\,\mathsf{P}_{\nu_i}^{-\mu}(\cos\theta)}{d\theta}\right|_{\theta=\theta_1} \cdot \left.\frac{d\mathbb{Q}_{\nu_i}^{\mu}(\cos\theta)}{d\theta}\right|_{\theta=\theta_2} - \left.\frac{d\,\mathsf{P}_{\nu_i}^{-\mu}(\cos\theta)}{d\theta}\right|_{\theta=\theta_2} \cdot \left.\frac{d\mathbb{Q}_{\nu_i}^{\mu}(\cos\theta)}{d\theta}\right|_{\theta=\theta_1} = 0.
\tag{3.71}
$$

The values of ν_i fulfilling the above conditions have to be determined. As discussed for the Dirichlet boundary condition, this is done numerically by a root finding algorithm. Obviously, the weights in eq. (3.70) result in $C_i = \left.\frac{\mathbb{Q}_{\nu_i}^{\mu}(\cos\theta)}{d\theta}\right|_{\theta=\theta_1}$, $D_i = -\left.\frac{\mathsf{P}_{\nu_i}^{-\mu}(\cos\theta)}{d\theta}\right|_{\theta=\theta_1}$, and inserting these values in eq. (3.63) yields the eigenfunctions

$$
\Theta_{\nu_i}^{\mu}(\theta) = N_{\nu_i}^{\mu}\left[\left.\frac{d\mathbb{Q}_{\nu_i}^{\mu}(\cos\theta)}{d\theta}\right|_{\theta=\theta_1} \cdot \mathsf{P}_{\nu_i}^{-\mu}(\cos\theta) - \left.\frac{d\,\mathsf{P}_{\nu_i}^{-\mu}(\cos\theta)}{d\theta}\right|_{\theta=\theta_1} \cdot \mathbb{Q}_{\nu_i}^{\mu}(\cos\theta)\right],
\tag{3.72}
$$

whereby the normalization constant $N_{\nu_i}^{\mu}$ is chosen such that $\int_{\theta_1}^{\theta_2}\left(\Theta_{\nu_i}^{\mu}(\theta)\right)^2\sin\theta\,d\theta = 1$. Similar to the case of Dirichlet boundary conditions, the normalization constant is computed either numerically or by a closed-form expression involving derivatives of the associated Legendre functions with respect to ν.

Figure 3.4 shows exemplarily the first seven eigenfunctions $\Theta_{\nu_i}^{\mu}(\theta)$, for $\mu = 0$ and symmetric Dirichlet and Neumann boundary conditions at $\theta_1 = 60°$ and $\theta_1 = 120°$. All functions, respectively their derivatives, are zero at the location of the boundary conditions, which are indicated by the vertical black lines. At $\theta = 0°$, $\theta = 180°$, the functions show a singular behavior.

Figure 3.5 shows the trajectories of the eigenvalue parameter ν_i for a symmetric regular two point boundary condition, i.e. $\theta_2 = 180 - \theta_1$, in dependence of θ_1. The solid lines correspond to a Neumann boundary condition, the dashed lines correspond to a Dirichlet boundary condition, respectively. The different colors correspond to the 1st (blue), 2nd (orange), 3rd (yellow), ect. eigenvalue. Subfigures (a) to (f) show the results for $m = 0, \ldots, 5$. For $\theta_1 \to 0°$, i.e. when the location of the symmetric boundary condition approaches the singular points of the differential equation, the eigenvalue parameters tend to integer values. The intersection of dashed vertical line in fig. 3.5a with the trajectories corresponds to the eigenvalue parameters of the

functions depicted in fig. 3.4.

Singular problems in θ. Choosing $\theta_1 = 0$ or $\theta_2 = \pi$, the respective endpoint is singular. In the following we sub-divide these singular problems into two cases. The first case covers boundary conditions with one endpoint singular and the other one regular. Physically this corresponds to a semi-infinite cone with either a sound soft or sound hard surface, depending on the boundary condition at the regular endpoint, see fig. 3.3a. The second case covers boundary conditions with both endpoints singular. Physically, this corresponds to a sound field with no specified local boundary condition in θ.

    Boundary conditions with one singular endpoint. Here we consider boundary conditions with a singular endpoint $\theta_1 = 0$ and a regular endpoint $0 < \theta_2 < \pi$. Note that problems with a regular endpoint $0 < \theta_1 < \pi$ and a singular endpoint $\theta_2 = \pi$ are not considered separately. Such problems can be solved similarly by substitution. Replacing θ by $\pi - \theta$ and θ_2 by $\pi - \theta_1$, i.e. flipping the z-coordinate in Cartesian coordinates, transforms a problem with a singular endpoint at π to a problem with a singular endpoint at 0.

    To determine the eigenfunctions we first consider the singular endpoint $\theta_1 = 0$, which is either LC or LP depending on the value of μ, see table 3.2b. In the LP case, i.e. $\mu \geq 1$, the boundary condition at the singular endpoint is vacuous. However, the eigenfunctions are required to be square integrable on $\theta \in [0, \theta_2]$, i.e. $\int_0^{\theta_2} |\Theta_{\nu_i}^\mu(\theta)|^2 \sin \theta d\theta < +\infty$. Note that the sine function in the integral results from the substitution $x = \cos \theta$ to bring eq. (3.5) in Sturm-Liouville form, cf. table 3.1. It shows that

$$\int_0^{\theta_2} |\, \mathsf{P}_\nu^{-\mu}(\cos \theta)|^2 \sin \theta d\theta < +\infty \text{ for } \mu > 0 \text{ and } 0 < \theta_2 < \pi, \qquad (3.73)$$

and for $\mu \geq 1$, $\mathsf{P}_\nu^{-\mu}(\cos \theta)$ is the only linearly independent solution which is square integrable on $[0, \theta_2]$. A proof is given in appendix E. In the LC case applies the Friedrichs boundary condition, which is only fulfilled by the principal solution, cf. section 3.2.3. The principal solution at the singulartiy $\theta = 0$ is $\mathsf{P}_\nu^{-\mu}(\cos \theta)$ for $\mu \geq 0$, cf. [DLMF, §14.2(iii)].

    Hence in both cases, whether the singular endpoint is LC or LP, the eigenfunctions are $\mathsf{P}_{\nu_i}^{-\mu}(\cos \theta)$. The values of ν_i depend on the boundary condition at the regular
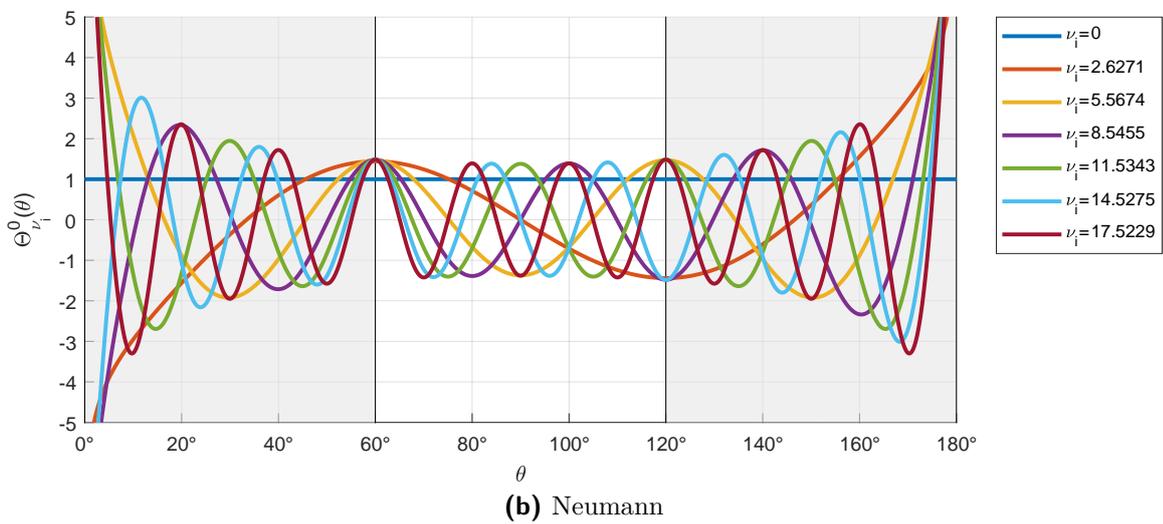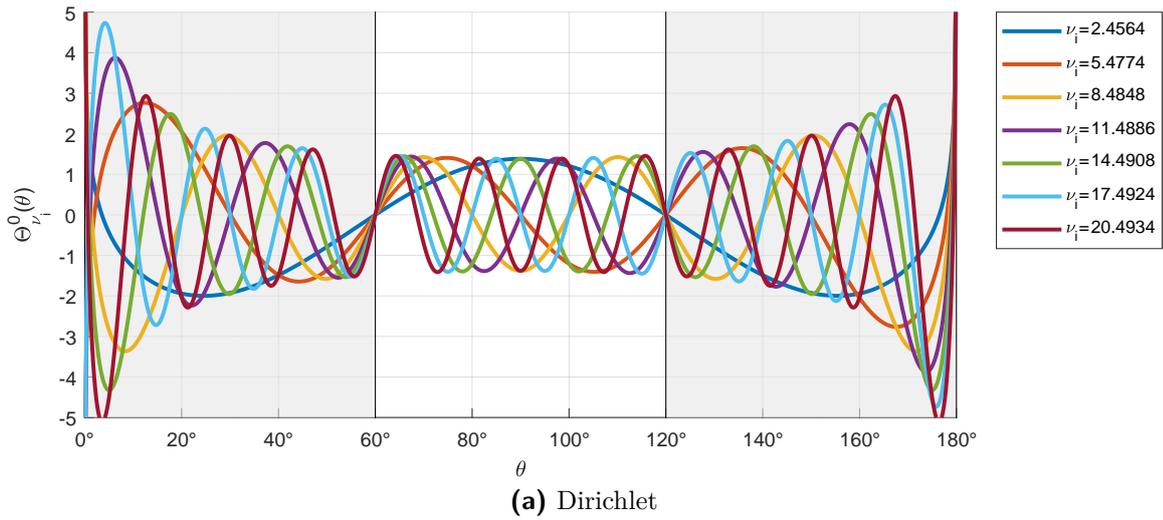
Figure 3.4: Eigenfunctions $\Theta_{\nu_i}^\mu(\theta)$, with $\mu = 0$, for (a) a symmetric Dirichlet and (b) a symmetric Neumann boundary condition at $\theta_1 = 60°$ and $\theta_1 = 120°$. The location of the boundary conditions are indicated by the vertical black lines.
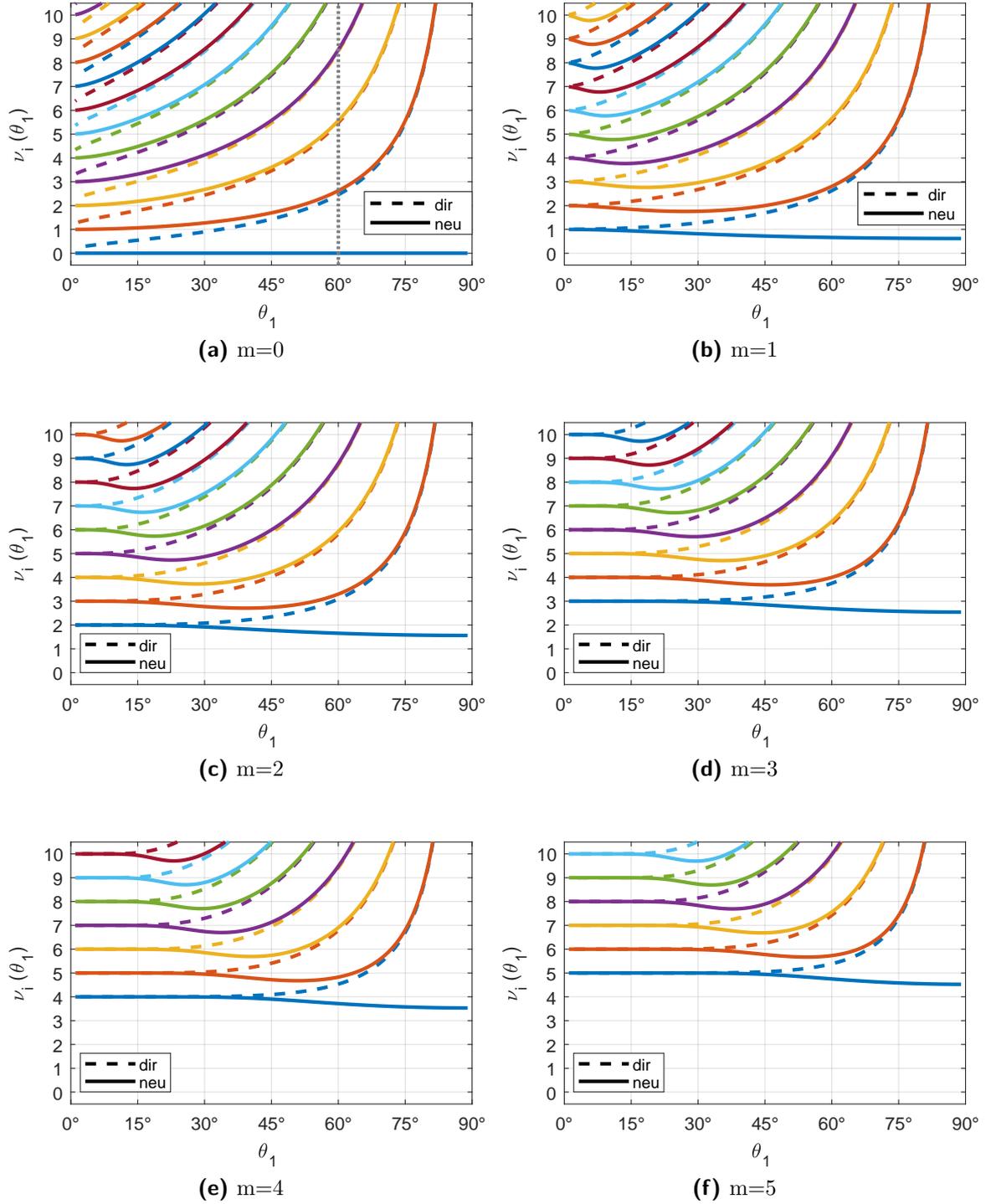
Figure 3.5: Parameter $\nu_i(\theta_1)$ for a symmetric regular two point boundary condition, i.e. $\theta_2 = 180 - \theta_1$. The solid lines correspond to a Neumann boundary condition, the dashed lines correspond to a Dirichlet boundary condition, respectively. The different colors correspond to the 1$^{\text{st}}$ (blue), 2$^{\text{nd}}$ (orange), 3$^{\text{rd}}$ (yellow), ect. eigenvalue. Subfigures (a) to (f) show the results for $m = 0, \ldots, 5$.

endpoint θ_2. At this endpoint the eigenfunctions are required to fulfill either a Dirichlet boundary condition

$$\left. \mathsf{P}_{\nu_i}^{-\mu}(\cos\theta)\right|_{\theta=\theta_2} = 0, \tag{3.74}$$

or a Neumann boundary condition

$$\left. \frac{d\,\mathsf{P}_{\nu_i}^{-\mu}(\cos\theta)}{d\theta}\right|_{\theta=\theta_2} = 0. \tag{3.75}$$

As for regular boundary conditions, the zeros of these functions with respect to ν are determined by a numerical root-finding algorithm. The normalized eigenfunctions yield

$$\Theta_{\nu_i}^{\mu}(\theta) = N_{\nu_i}^{\mu}\,\mathsf{P}_{\nu_i}^{-\mu}(\cos\theta), \tag{3.76}$$

whereby $N_{\nu_i}^{\mu}$ is chosen such that $\int_0^{\theta_2}\left(\Theta_{\nu_i}^{\mu}(\theta)\right)^2\sin\theta d\theta = 1$. Similar to separated regular boundary conditions, the normalization constant is computed either numerically or by a closed-form expression, involving derivatives of the associated Legendre functions with respect to ν.

Figure 3.6 shows exemplarily the first seven eigenfunctions $\Theta_{\nu_i}^{\mu}(\theta)$, for $\mu = 0$, a singular boundary condition at $\theta_1 = 0°$, and a Dirichlet respectively Neumann boundary condition at $\theta_2 = 120°$. All functions, respectively their derivatives, are zero at the location of the regular boundary condition, indicated by the vertical black line. At the singular endpoint $\theta = 180°$ the functions show a singular behavior.

Figure 3.7 shows the trajectories of the eigenvalue parameter ν_i for a singular boundary condition at $\theta_1 = 0°$ and a Dirichlet respectively Neumann boundary condition at θ_2, in dependence of θ_2. The solid lines correspond to a Neumann boundary condition, the dashed lines correspond to a Dirichlet boundary condition, respectively. The different colors correspond to the 1st (blue), 2nd (orange), 3rd (yellow), ect. eigenvalue. Subfigures (a) to (f) show the results for $m = 0, \ldots, 5$. For $\theta_2 \to 180°$, i.e. when the location of the regular boundary condition approaches the second singular point of the differential equation, the eigenvalue parameters tend to integer values. The intersection of dashed vertical line in fig. 3.7a with the trajectories corresponds to the eigenvalue parameters of the functions depicted in fig. 3.6.

(a) Dirichlet
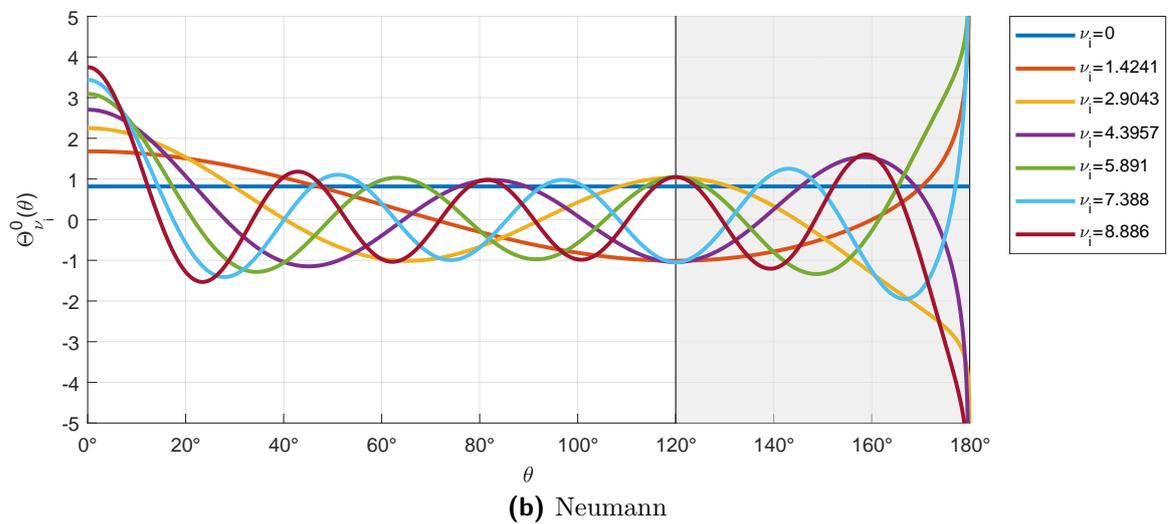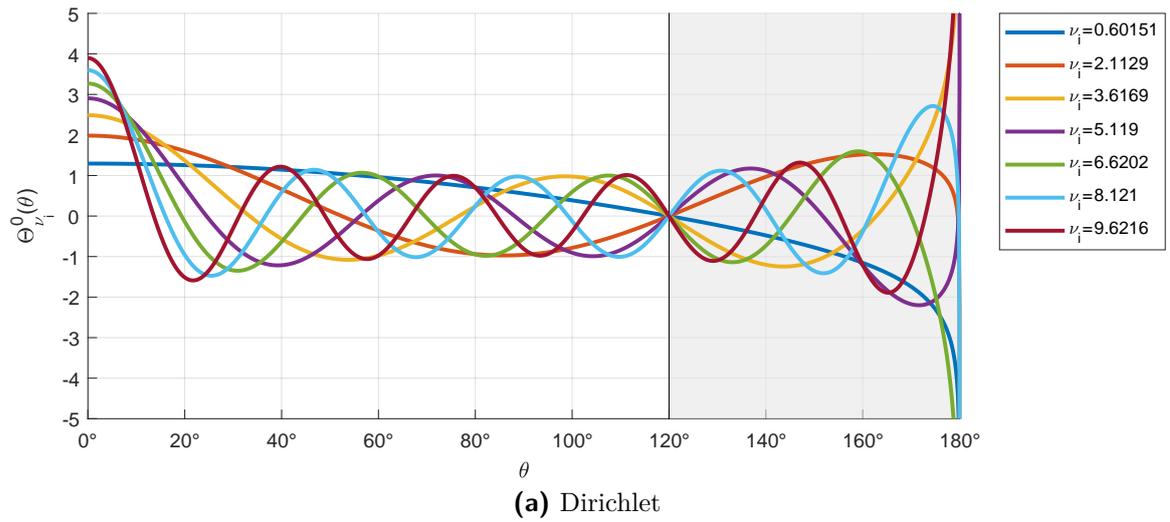
(b) Neumann

Figure 3.6: Eigenfunctions $\Theta^\mu_{\nu_i}(\theta)$, with $\mu = 0$, for a singular boundary condition at $\theta_1 = 0°$ and (a) a regular Dirichlet and (b) a regular Neumann boundary condition at $\theta_1 = 120°$. The location of the regular boundary condition is indicated by the vertical black line.
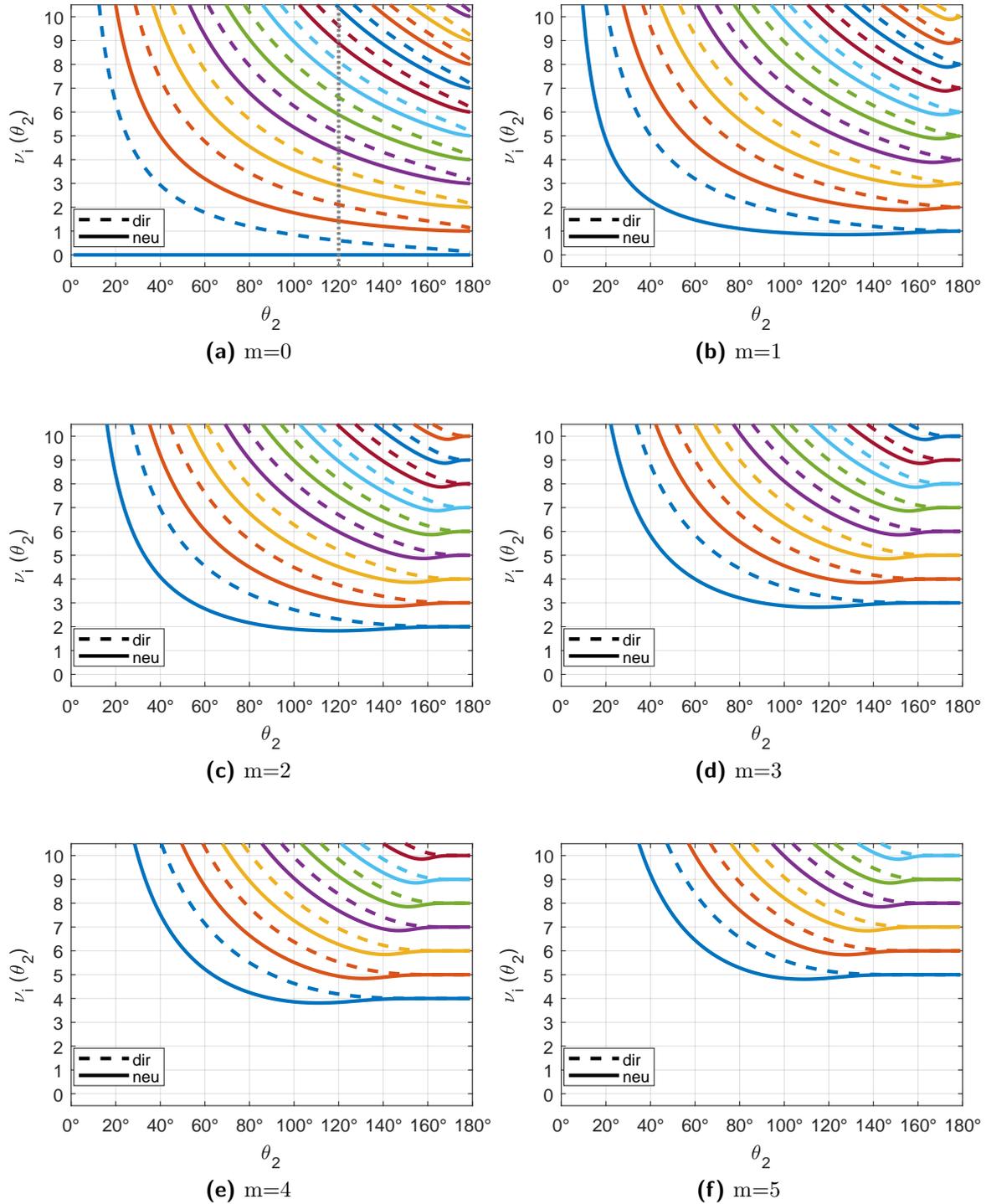
Figure 3.7: Parameter $\nu_i(\theta_2)$ for a regular boundary condition at θ_2 and a singular endpoint at $\theta_1 = 0°$. The solid lines correspond to a Neumann boundary condition, the dashed lines correspond to a Dirichlet boundary condition, respectively. The different colors correspond to the 1ˢᵗ (blue), 2ⁿᵈ (orange), 3ʳᵈ (yellow), ect. eigenvalue. Subfigures (a) to (f) show the results for $m = 0, \ldots, 5$.

Boundary condition with both endpoints singular. In the following we consider boundary conditions with both endpoint singular, i.e. $\theta_1 = 0$ and $\theta_2 = \pi$. Both endpoints are either LC or LP depending on the value of μ, see table 3.2b.

If both endpoints are LP, i.e. $\mu \geq 1$, there is no boundary condition. In this case every square integrable function on the interval $[0, \pi]$ that fulfills eq. (3.5) is an eigenfunction. Hence the eigenfunctions are required to fulfill $\int_0^\pi |\Theta^\mu_{\nu_i}(\theta)|^2 \sin\theta d\theta < +\infty$. It shows that

$$\int_0^\pi | \, \mathsf{P}^{-\mu}_{\mu+l}(\cos\theta)|^2 \sin\theta d\theta < +\infty \text{ for } \mu > 0 \text{ and } l = 0, 1, 2, 3, \ldots, \tag{3.77}$$

and for $\mu \geq 1$, $\mathsf{P}^{-\mu}_{\mu+l}(\cos\theta)$ is the only linearly independent solution which is square integrable on $[0, \pi]$. A proof is given in appendix E. If both endpoints are LC, i.e. $0 \leq \mu < 1$, Friedrichs boundary condition applies at each endpoint, which is only fulfilled by the principal solution at the respective endpoint, cf. section 3.2.3. For $\mu \geq 0$, the principal solutions at $\theta = 0$ and $\theta = \pi$ are $\mathsf{P}^{-\mu}_\nu(\cos\theta)$ and $\mathsf{P}^{-\mu}_\nu(-\cos\theta)$, respectively, cf. [DLMF, §14.2(iii)]. From the Wronskian of $\mathsf{P}^\mu_\nu(x)$ and $\mathsf{P}^\mu_\nu(-x)$, [DLMF, §14.2(iv)], it shows that these solutions are linearly dependent if $\mu - \nu = 0, -1, -2, \ldots$ Thus $\mathsf{P}^{-\mu}_{\mu+l}(\cos\theta)$ with $l = 0, 1, 2, 3, \ldots$, satisfies Friedrichs boundary condition at $\theta = 0$ and $\theta = \pi$, as it is the principal solution at both singular endpoints.

Hence in both cases, whether the singular endpoints are LC or LP, the eigenfunctions are $\mathsf{P}^{-\mu}_{\mu+l}(\cos\theta)$ and the normalized eigenfunctions yield

$$\Theta^\mu_{\mu+l}(\theta) = N^\mu_{\mu+l} \, \mathsf{P}^{-\mu}_{\mu+l}(\cos\theta), \tag{3.78}$$

whereby $N^\mu_{\mu+l}$ is chosen such that $\int_0^\pi \left(\Theta^\mu_{\nu_i}(\theta)\right)^2 \sin\theta d\theta = 1$. In this case there is a closed-form expression for $N^\mu_{\mu+l}$. Following the approach in [LS75], one can find the expression

$$\int_0^\pi \left(\mathsf{P}^{-\mu}_{\mu+l}(\cos\theta)\right)^2 \sin\theta d\theta = \frac{2l!}{(2\mu + 2l + 1)\,\Gamma(2\mu + l + 1)}, \text{ for } l = 0, 1, 2, 3 \ldots, \tag{3.79}$$

from the recurrence relations of the associated Legendre functions, cf. [DLMF, §14.10] and the definite integral $\int_0^\pi \left(\mathsf{P}^{-\mu}_\mu(\cos\theta)\right)^2 \sin\theta d\theta = \frac{2^{-2\mu}\sqrt{\pi}}{\Gamma(1+\mu)\Gamma(\frac{2}{3}+\mu)}$. This definite integral is achieved by integrating the expression $\mathsf{P}^{-\mu}_\mu(x) = 2^{-\nu}\frac{(1-x^2)^{\frac{\nu}{2}}}{\Gamma(1+\nu)}$, given in [MOS66,
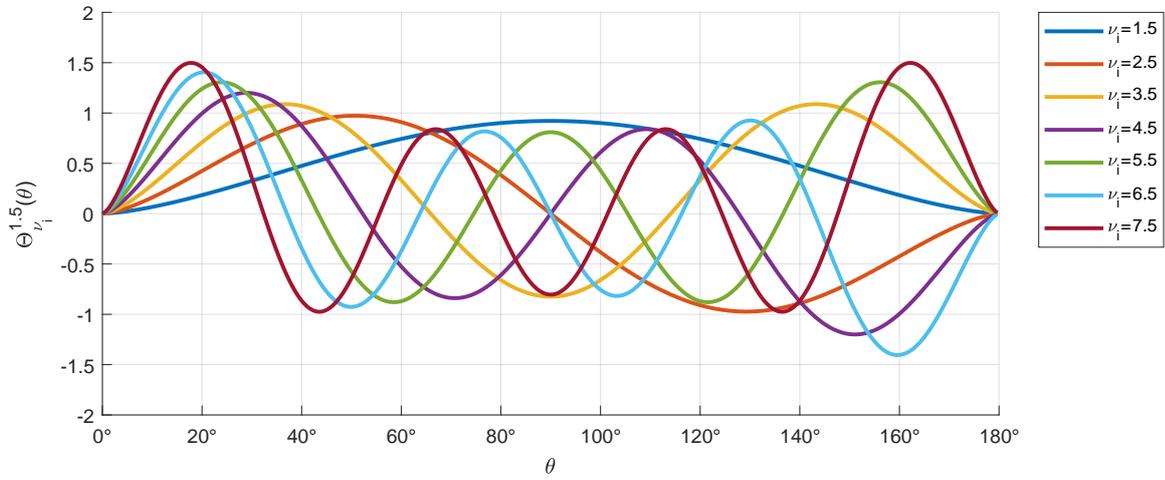
Figure 3.8: Eigenfunctions $\Theta_{\nu_i}^\mu(\theta)$, with $\mu = 1.5$, for a singular boundary condition at both endpoints.

p.172]. Therewith the normalization term yields

$$N_{\mu+l}^\mu = \sqrt{\frac{(2\mu + 2l + 1)\,\Gamma(2\mu + l + 1)}{2l!}}.$$

(3.80)

Figure 3.6 shows exemplarily the first seven eigenfunctions $\Theta_{\nu_i}^\mu(\theta)$, for $\mu = 1.5$ and a singular boundary condition at both endpoints.

Chapter 4

Solution of the Helmholtz equation with rigid angular boundaries

Within this chapter we develop the solution of the Helmholtz equation in regions of $\mathbb{R}^3$ bounded by coordinate surfaces in ϕ and θ. The applied homogeneous boundary conditions could be either sound-soft (Dirichlet), sound-hard (Neumann) or any combinations thereof. There are up to two boundary surfaces possible in both, azimuth and zenith angle. Due to the variety of combinations, we considers here sound-hard boundaries, only. Sound-soft boundaries are nearly not feasible to realize in practice, and hence of minor relevance for microphone array applications.

4.1 Angular solutions

Combining the angular solutions of the Helmholtz equation fulfilling sound-hard boundary conditions in azimuth and zenith angle, as described in the previous chapter, yields orthonormal function sets on several partial spherical surfaces. Depending on the boundary conditions, this allows for spherical zones, lunes or intersections of a zone and a lune, cf. fig. 4.1. Within this work we use the term *spherical quadrangle*, as there is no common name for the intersection of a spherical zone and lune, although this is not a very accurate naming[1].

In analogy to the terms *spherical harmonics* and *spherical cap harmonics* [Hai85], the consistent naming for functions on a spherical zone would be *spherical zone*

---

[1]Occasionally, the term *spherical quadrangle* is used for a four sided spherical polygon, whereby the term *spherical quadrilateral* is more common. However, a spherical polygon is defined as a surface on the sphere formed by arcs of great circles; in contrast the intersection of a zone and a lune is bounded by arcs of two great and two small circles.
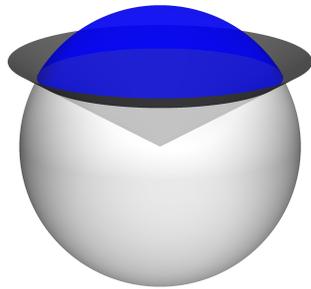
(a) spherical cap
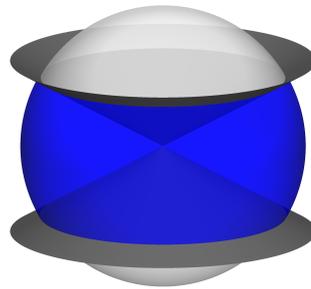
(b) spherical zone
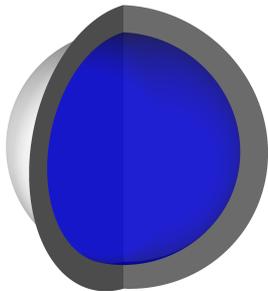
(c) spherical lune
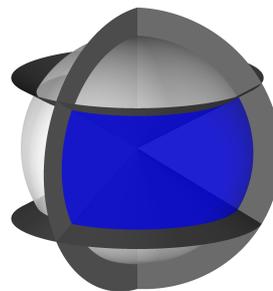
(d) spherical quadrangle
(intersection of zone and lune)

Figure 4.1: Feasible partial spherical surfaces accomplished by angular boundary conditions.

harmonics. However, the term *zonal spherical harmonics* is frequently used in literature for the subset of spherical harmonics, which do not depend on the zenith angle θ, i.e. $m = n$. To avoid confusion, we use the term *spherical segment harmonics* for orthogonal functions on a spherical zone. A spherical segment is the solid that remains after cutting a sphere with two parallel planes, and the curved surface of a spherical segment is a spherical zone.

4.1.1 Spherical cap harmonics.

These are the eigenfunctions of the Helmholtz equation fulfilling a 2π-periodic boundary condition in the azimuth angle as well as a Neumann boundary condition at θ_2, and a singular boundary condition at the north pole, i.e. $\theta = 0$. This set of boundary

conditions corresponds to a semi-infinite rigid cone, cf. fig. 3.3a, and the partial surface of the unit sphere enclosed by the boundary is a spherical cap, cf. fig. 4.1a.

Similar to the conventional spherical harmonics, the parameter μ of the azimuthal eigenfunctions yields a non-negative integer due to the 2π-periodic boundary condition, and every eigenvalue except $\mu^2 = 0$ is associated with two eigenfunctions, cf. section 3.3.1. For notational convenience we define $\mu = m \in \mathbb{Z}$ and the sign of m is used to distinguish the two solutions, avoiding an additional index[2]. Thus the normalized azimuthal eigenfunctions, cf. eq. (3.56), are denoted by

$$\Phi_m(\phi) = \sqrt{\tfrac{2-\delta_m}{2\pi}} \begin{cases} \sin(m\phi), & \text{for } m < 0, \\ \cos(m\phi), & \text{for } m \geq 0. \end{cases} \tag{4.1}$$

With the inherited parameter $\mu = m$ and for a singular boundary condition at $\theta = 0$, the normalized eigenfunctions in θ are denoted by, cf. eq. (3.76),

$$\Theta^{|m|}_{\nu_l(|m|)}(\theta) = \sqrt{\frac{1}{\int_0^{\theta_2} \left| \mathsf{P}^{-|m|}_{\nu_l(|m|)}(\cos\theta) \right|^2 \sin\theta d\theta}} \, \mathsf{P}^{-|m|}_{\nu_l(|m|)}(\cos\theta), \tag{4.2}$$

whereby for each m the infinite sequence $\left(\nu_l(|m|)\right)_{l\in\mathbb{N}}$, with $\nu_l(|m|) \leq \nu_{l+1}(|m|)$, contains the values, for which the the Neumann boundary condition at $\theta = \theta_2$ is fulfilled, cf. section 3.3.2, i.e. $\frac{\mathsf{P}^{-|m|}_{\nu_l(|m|)}(\cos\theta_2)}{d\theta} = 0, \, \forall l \in \mathbb{N}$.

Combining the normalized eigenfunctions in azimuth and zenith angle yields a set of complete orthonormal functions on the spherical cap $\mathcal{S}^2 \subset \mathbb{S}^2$, with $\mathcal{S}^2 := \{\boldsymbol{\theta} : 0 \leq \theta \leq \theta_2\}$. These functions are called *spherical cap harmonics* and are denoted by

$$Y^m_{\nu_l(|m|)}(\boldsymbol{\theta}) = N^{|m|}_{\nu_l(|m|)} \, \mathsf{P}^{-|m|}_{\nu_l(|m|)}(\cos\theta) \cdot \begin{cases} \sin(m\phi), & \text{for } m < 0, \\ \cos(m\phi), & \text{for } m \geq 0, \end{cases} \tag{4.3}$$

whereby the normalization term is

$$N^{|m|}_{\nu_l(|m|)} = \sqrt{\frac{(2-\delta_m)}{2\pi \int_0^{\theta_2} \left| \mathsf{P}^{-|m|}_{\nu_l(|m|)}(\cos\theta) \right|^2 \sin\theta d\theta}}. \tag{4.4}$$

Orthogonality and completeness follows straight-forward from the Sturm-Liouville theory, cf. section 3.2. Due to the proper normalization the following orthogonality

---

[2]This sign convention is similar to the usual notation of conventional spherical harmonics.
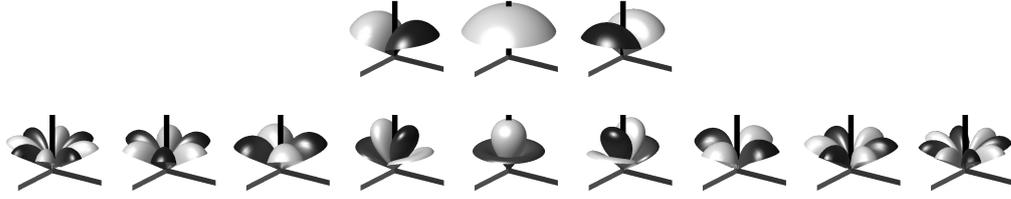
Figure 4.2: Spherical cap harmonics for a conical sound-hard boundary condition at $\theta_2 = 60°$; from the infinite sequence, only functions with $\nu_l(|m|) \leq 6$ are shown.

relation holds,

$$\int_{\mathcal{S}^2} Y^m_{\nu_l(|m|)}(\boldsymbol{\theta}) \, Y^{m'}_{\nu'_l(|m'|)}(\boldsymbol{\theta}) d\boldsymbol{\theta} = \delta_{ll'}\delta_{mm'} \tag{4.5}$$

and any square-integrable function on the spherical cap $\mathcal{S}^2$ can be expanded in a series of spherical cap harmonics,

$$f(\boldsymbol{\theta}) = \sum_{m=-\infty}^{\infty} \sum_{l=1}^{\infty} f_{lm} Y^m_{\nu_l(|m|)}(\boldsymbol{\theta}), \tag{4.6}$$

where $f_{lm} = \int_{\mathcal{S}^2} f(\boldsymbol{\theta}) Y^m_{\nu_l(|m|)}(\boldsymbol{\theta}) d\boldsymbol{\theta}$ are the expansion coefficients.

Figure 4.2 shows exemplary the first few spherical cap harmonics with $\nu_l(|m|) \leq 6$ for a cap with a sound-hard boundary condition at $\theta_2 = 60°$.

4.1.2 Spherical segment harmonics.

These are the angular solutions of the Helmholtz equation fulfilling a 2π-periodic boundary condition in the azimuth and a two-point Neumann boundary condition in the zenith angle at θ_1, θ_2. This set of boundary conditions corresponds to an infinite rigid double-cone, cf. fig. 3.3b, and the partial surface of the unit sphere enclosed by the boundaries is a spherical zone, cf. fig. 4.1b.

Due to the 2π-periodic boundary condition in ϕ the azimuthal eigenfunctions are the same as for the spherical cap harmonics, cf. eq. (4.1). With the inherited parameter $\mu = m$ from the azimuthal eigenfunctions and for the two-point Neumann boundary condition at $\theta_{1,2}$, cf. eq. (3.72), the normalized eigenfunctions in θ yield

$$\Theta^{|m|}_{\nu_l(|m|)}(\theta) = \sqrt{\frac{1}{\int_{\theta_1}^{\theta_2} \left| P^{|m|}_{\nu_l(|m|)}(\cos\theta) \right|^2 \sin\theta d\theta}} \, P^{|m|}_{\nu_l(|m|)}(\cos\theta), \tag{4.7}$$

whereby for a compact notation we define

$$P^\mu_\nu(\cos\theta) = \left. \frac{d\,\mathbb{Q}^\mu_\nu(\cos\theta)}{d\theta} \right|_{\theta=\theta_1} \cdot \mathsf{P}^{-\mu}_\nu(\cos\theta) - \left. \frac{d\,\mathsf{P}^{-\mu}_\nu(\cos\theta)}{d\theta} \right|_{\theta=\theta_1} \mathbb{Q}^\mu_\nu(\cos\theta). \tag{4.8}$$

60
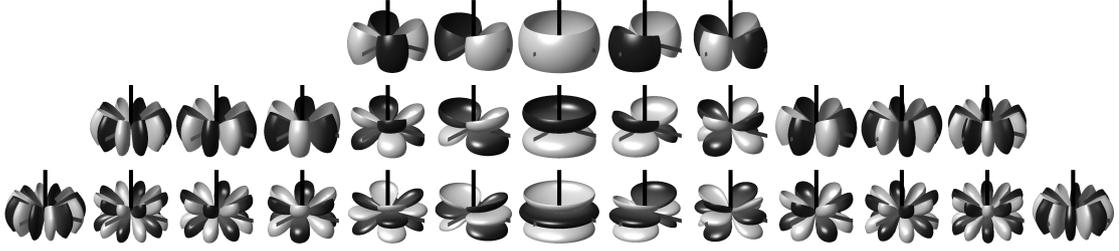
Figure 4.3: Spherical segment harmonics for a two conical sound-hard boundary conditions at $\theta = 60°$ and $\theta = 120°$; from the infinite sequence, only functions with $\nu_l(|m|) \leq 6$ are shown.

The values of $\nu_l(|m|)$ are determined by the location of the Neumann boundary conditions, cf. section 3.3.2, such that $\left. \frac{d\,P_{\nu_l(|m|)}^{|m|}(\cos\theta)}{d\theta} \right|_{\theta=\theta_{1,2}} = 0$.

Combining the normalized eigenfunctions in azimuth and zenith angle yields a set of complete orthonormal functions on the spherical zone $\mathcal{S}^2 \subset \mathbb{S}^2$, with $\mathcal{S}^2 := \{\boldsymbol{\theta} : \theta_1 \leq \theta \leq \theta_2\}$. These functions are called *spherical segment harmonics* and are denoted by

$$Y_{\nu_l(|m|)}^m(\boldsymbol{\theta}) = N_{\nu_l(|m|)}^{|m|} \, P_{\nu_l(|m|)}^{|m|}(\cos\theta) \cdot \begin{cases} \sin(m\phi), & \text{for } m < 0, \\ \cos(m\phi), & \text{for } m \geq 0. \end{cases} \tag{4.9}$$

whereby the normalization term is

$$N_{\nu_l(m)}^{|m|} = \sqrt{\frac{(2 - \delta_m)}{2\pi \int_{\theta_1}^{\theta_2} \left| P_{\nu_l(m)}^{|m|}(\cos\theta) \right|^2 \sin\theta \, d\theta}}. \tag{4.10}$$

Like for the spherical cap harmonics, orthogonality and completeness follows straight-forward from the Sturm-Liouville theory, cf. section 3.2. The orthogonality relation and the series expansion on the spherical zone $\mathcal{S}^2$ are formally equal to eqs. (4.5) and (4.6).

Figure 4.3 shows exemplary the first few spherical segment harmonics with $\nu_l(|m|) \leq 6$ for a spherical zone bounded by a sound-hard symmetric double cone with $\theta_1 = 60°$ $\theta_2 = 120°$.

4.1.3 Spherical lune harmonics.

These are the angular solutions of the Helmholtz equation fulfilling a two-point Neumann boundary condition in the azimuth angle at ϕ_1, ϕ_2, as well as singular boundary conditions at the north and south pole. This set of boundary conditions

corresponds to two semi-infinite rigid half-planes, cf. fig. 3.2, and the partial surface of the unit sphere enclosed by the boundaries is a spherical lune, cf. fig. 4.1c.

For the two-point Neumann boundary condition in ϕ we assume for simplicity that $\theta_1 = 0$. The normalized azimuthal eigenfunctions yield, cf. eq. (3.52),

$$\Phi_{\mu_k}(\phi) = \sqrt{\tfrac{2-\delta_k}{\phi_2}} \cos\left(\mu_k \phi\right). \tag{4.11}$$

where $\mu_k = \frac{\pi k}{\theta_2}$, with $k = 0, 1, 2, \ldots, \infty$. With the inherited parameter μ_k from the azimuthal eigenfunctions, the eigenfunctions in θ for the singular boundary conditions yield, cf. eq. (3.78),

$$\Theta_{\mu_k+l}^{\mu_k}(\theta) = \sqrt{\tfrac{(2\mu_k+2l+1)\,\Gamma(2\mu_k+l+1)}{2l!}}\, \mathsf{P}_{\mu_k+l}^{-\mu_k}(\cos\theta), \tag{4.12}$$

Combining the normalized eigenfunctions in azimuth and zenith angle yield a set of complete orthonormal functions on the spherical lune $\mathcal{S}^2 \subset \mathbb{S}^2$ with $\mathcal{S}^2 := \{\boldsymbol{\theta} : 0 \le \phi \le \phi_2\}$. These functions are called *spherical lune harmonics* and are denoted by

$$Y_{\mu_k+l}^{\mu_k}(\boldsymbol{\theta}) = N_{\mu_k+l}^{\mu_k} \cos(\mu_k\phi)\mathsf{P}_{\mu_k+l}^{-\mu_k}(\cos\theta), \tag{4.13}$$

whereby the normalization term is

$$N_{\mu_k+l}^{\mu_k} = \sqrt{\frac{(2-\delta_k)}{\phi_2}\frac{(2\mu_k+2l+1)\,\Gamma(2\mu_k+l+1)}{2l!}}. \tag{4.14}$$

With the orthogonality and completeness deduced from the Sturm-Liouville theory, cf. section 3.2, the orthogonality relation and series expansion on the spherical lune $\mathcal{S}^2$ are,

$$\int_{\mathcal{S}^2} Y_{\mu_k+l}^{\mu_k}(\boldsymbol{\theta})\, Y_{\mu_k'+l'}^{\mu_k'}(\boldsymbol{\theta})d\boldsymbol{\theta} = \delta_{ll'}\delta_{kk'}, \tag{4.15}$$

$$f(\boldsymbol{\theta}) = \sum_{k=0}^{\infty}\sum_{l=1}^{\infty} f_{lk}Y_{\mu_k+l}^{\mu_k}(\boldsymbol{\theta}), \tag{4.16}$$

whereby $f_{lk} = \int_{\mathcal{S}^2} f(\boldsymbol{\theta})Y_{\mu_k+l}^{\mu_k}(\boldsymbol{\theta})d\boldsymbol{\theta}$ are the expansion coefficients.

Figure 4.4 shows exemplary the first few spherical lune harmonics with $\mu_k + l \le 6$, for a spherical lune bounded by sound-hard half-planes at $\phi_1 = 0°$ $\phi_2 = 120°$.

4.1.4 Spherical quadrangle harmonics.

These are the angular solutions of the Helmholtz equation fulfilling a two-point Neumann boundary condition in both angular directions, at ϕ_1, ϕ_2 in the azimuth angle
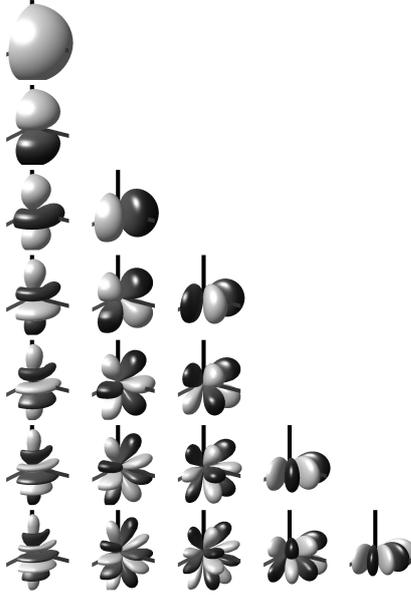
Figure 4.4: Spherical lune harmonics for two planar sound-hard boundary conditions at $\phi = 0°$ and $\phi = 120°$; from the infinite sequence, only functions with $\mu_k + l \leq 6$ are shown.

and at θ_1, θ_2 in the zenith angle. The boundary conditions in the azimuth correspond to two semi-infinite rigid half-planes, cf. fig. 3.2, and the boundary conditions in the zenith angle correspond to an infinite rigid double-cone, cf. fig. 3.3b. The partial surface of the unit sphere enclosed by these boundaries is the intersection of a spherical zone and a spherical lune, cf. fig. 4.1d. For this partial spherical surface we use the term *spherical quadrangle*.

As for the spherical lune harmonics, we assume for simplicity that $\theta_1 = 0$. As the azimuthal eigenfunctions are independent of the boundary condition in the zenith angle, they are identical to those for the spherical lune, cf. eq. (4.11). With the inherited parameter μ_k from the azimuthal eigenfunctions, and for the two-point Neumann boundary condition at $\theta_{1,2}$, cf. eq. (3.72), the normalized eigenfunctions in θ yield

$$\Theta^{\mu_k}_{\nu_l(\mu_k)}(\theta) = \sqrt{\frac{1}{\int_{\theta_1}^{\theta_2} \left| P^{\mu_k}_{\nu_l(\mu_k)}(\cos\theta) \right|^2 \sin\theta d\theta}} \, P^{\mu_k}_{\nu_l(\mu_k)}(\cos\theta), \tag{4.17}$$

where $P^{\mu}_{\nu}(\cos\theta)$ is defined in eq. (4.8). The values of $\nu_l(\mu_k)$ are determined by the Neumann boundary conditions, cf. section 3.3.2, such that $\left. \frac{d\,P^{\mu_k}_{\nu_l(\mu_k)}(\cos\theta)}{d\theta} \right|_{\theta=\theta_{1,2}} = 0$.

Combining the normalized eigenfunctions in azimuth and zenith angle yield a set of complete orthonormal functions on the spherical quadrangle $\mathcal{S}^2 \subset \mathbb{S}^2$, with $\mathcal{S}^2 := \{\boldsymbol{\theta} : 0 \leq \phi \leq \phi_2 \text{ and } \theta_1 \leq \theta \leq \theta_2\}$. These functions are called *spherical quadrangle*
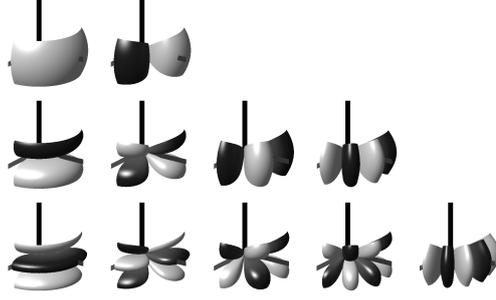
Figure 4.5: Spherical quadrangle harmonics for two planar sound-hard boundary condition at $\phi = 0°$, $\phi = 120°$ and two conical sound-hard boundary conditions at $\theta = 60°$, $\theta = 120°$; from the infinite sequence, only functions with $\nu_l(|m|) \leq 6$ are shown.

harmonics and are denoted by

$$Y^{\mu_k}_{\nu_l(\mu_k)}(\boldsymbol{\theta}) = N^{\mu_k}_{\nu_l(\mu_k)} \, P^{-\mu_k}_{\nu_l(\mu_k)}(\cos\theta) \, \cos(\mu\phi), \tag{4.18}$$

whereby the normalization term is

$$N^{\mu_k}_{\nu_l(\mu_k)} = \sqrt{\frac{(2 - \delta_k)}{\phi_2 \int_{\theta_1}^{\theta_2} \left| P^{\mu_k}_{\nu_l(\mu_k)}(\cos\theta) \right|^2 \sin\theta d\theta}}. \tag{4.19}$$

The functions are orthonormal on the spherical quadrangle $\mathcal{S}^2$, i.e.

$$\int_{\mathcal{S}^2} Y^{\mu_k}_{\nu_l(\mu_k)}(\boldsymbol{\theta}) \, Y^{\mu'_k}_{\nu'_l(\mu'_k)}(\boldsymbol{\theta}) d\boldsymbol{\theta} = \delta_{ll'} \delta_{kk'}, \tag{4.20}$$

and due to their completeness on $\mathcal{S}^2$ any square integrable function can be expanded in the series

$$f(\boldsymbol{\theta}) = \sum_{k=0}^{\infty} \sum_{l=1}^{\infty} f_{lk} Y^{\mu_k}_{\nu_l(\mu_k)}(\boldsymbol{\theta}), \tag{4.21}$$

where $f_{lk} = \int_{\mathcal{S}^2} f(\boldsymbol{\theta}) Y^{\mu_k}_{\nu_l(\mu_k)}(\boldsymbol{\theta}) d\boldsymbol{\theta}$ are the expansion coefficients.

Figure 4.5 shows exemplary the first few spherical quadrangle harmonics with $\nu_l(\mu_k) \leq 6$ for a spherical quadrangle bounded by sound-hard half-planes at $\phi_1 = 0°$, $\phi_2 = 120°$, and a sound-hard symmetric double cone with $\theta_1 = 60°$, $\theta_2 = 120°$.

4.1.5 Uniform notation

To achieve a uniform notation of the series expansions in spherical cap, segment, lune, and quadrangle harmonics, cf. eqs. (4.6), (4.16) and (4.21), we denote the respective

combinations of order and degree as a set of ordered pairs $\mathcal{N}$, where

$$\mathcal{N} := \begin{cases} \{(\nu_l(|m|), m) : l \in \mathbb{N}, m \in \mathbb{Z}\} & \text{for } Y_{\nu_l(|m|)}^m(\boldsymbol{\theta}) \text{ in eq. (4.3)}, \\ \{(\nu_l(|m|), m) : l \in \mathbb{N}, m \in \mathbb{Z}\} & \text{for } Y_{\nu_l(|m|)}^m(\boldsymbol{\theta}) \text{ in eq. (4.9)}, \\ \{(\mu_{k+l}, \mu_k) : l \in \mathbb{N}, k \in \mathbb{N}_0\} & \text{for } Y_{\mu_{k+l}}^{\mu_k}(\boldsymbol{\theta}) \text{ in eq. (4.13)}, \\ \{(\nu_l(\mu_k), \mu_k) : l \in \mathbb{N}, k \in \mathbb{N}_0\} & \text{for } Y_{\nu_l(\mu_k)}^{\mu_k}(\boldsymbol{\theta}) \text{ in eq. (4.18)}. \end{cases} \tag{4.22}$$

We use the linear index $q \in \mathbb{N}$ to index the parameter pairs $(\nu_q, \mu_q) \in \mathcal{N}$ in ascending lexicographical order, i.e. $\nu_q < \nu_{q+1}$ or $(\nu_q = \nu_{q+1}$ and $\mu_q < \mu_{q+1})$. In doing so, allows to express the series expansions on $\mathcal{S}^2 \subset \mathbb{S}^2$ in eqs. (4.6), (4.16) and (4.21) uniformly by

$$f(\boldsymbol{\theta}) = \sum_{q=1}^{\infty} f_q Y_{\nu_q}^{\mu_q}(\boldsymbol{\theta}), \tag{4.23}$$

where $Y_{\nu_q}^{\mu_q}(\boldsymbol{\theta})$ is either given by eq. (4.3), eq. (4.9), eq. (4.13), or eq. (4.18), respectively, $f_q = \int_{\mathcal{S}^2} f(\boldsymbol{\theta}) Y_{\nu_q}^{\mu_q}(\boldsymbol{\theta}) d\boldsymbol{\theta}$ are the corresponding expansion coefficients, and the partial spherical surface is defined by

$$\mathcal{S}^2 := \begin{cases} \{\boldsymbol{\theta} : 0 \le \theta \le \theta_2\} & \text{for a spherical cap}, \\ \{\boldsymbol{\theta} : \theta_1 \le \theta \le \theta_2\} & \text{for a spherical zone}, \\ \{\boldsymbol{\theta} : 0 \le \phi \le \phi_2\} & \text{for a spherical lune}, \\ \{\boldsymbol{\theta} : 0 \le \phi \le \phi_2 \text{ and } \theta_1 \le \theta \le \theta_2\} & \text{for a spherical quadrangle}. \end{cases} \tag{4.24}$$

We will refer to $Y_{\nu_q}^{\mu_q}(\boldsymbol{\theta})$ as *partial spherical harmonics* whenever it is used generically without specifying the particular case of boundaries. In this uniform notation, the orthogonality relation on $\mathcal{S}^2$ writes as

$$\int_{\mathcal{S}^2} Y_{\nu_q}^{\mu_q}(\boldsymbol{\theta}) \, Y_{\nu_q'}^{\mu_q'}(\boldsymbol{\theta}) d\boldsymbol{\theta} = \delta_{qq'}. \tag{4.25}$$

Equation (4.23) is equivalent to the completeness relation, cf. page 32,

$$\int_{\mathcal{S}^2} \left[f(\boldsymbol{\theta}) - \sum_{q=1}^{\infty} f_q Y_{\nu_q}^{\mu_q}(\boldsymbol{\theta}) \right]^2 d\boldsymbol{\theta} = 0, \tag{4.26}$$

Parseval's relation

$$\int_{\mathcal{S}^2} |f(\boldsymbol{\theta})|^2 d\boldsymbol{\theta} = \sum_{q=1}^{\infty} |f_q|^2, \tag{4.27}$$

and the closure relation

$$\sum_{q=1}^{\infty} Y_{\nu_q}^{\mu_q}(\boldsymbol{\theta}) Y_{\nu_q}^{\mu_q}(\boldsymbol{\theta}') = \delta(\boldsymbol{\theta} - \boldsymbol{\theta}'), \qquad (4.28)$$

where $\delta(\boldsymbol{\theta}) = \delta(\cos\theta - \cos\theta')\,\delta(\phi - \phi') = \frac{1}{\sin\theta}\delta(\theta - \theta')\,\delta(\phi - \phi')$.

Note that also the conventional spherical harmonics fit within this uniform notation, which are in fact the angular solutions fulfilling a 2π periodic boundary condition in ϕ as well as two-point singular boundary condition at $\theta_1 = 0$ and $\theta_2 = \pi$. Interchanging the summation and substituting $n = |m| + l$, the spherical harmonics expansion in eq. (2.14) is equivalent to

$$f(\boldsymbol{\theta}) = \sum_{m=-\infty}^{\infty} \sum_{l=0}^{\infty} f_{nl} Y_{|m|+l}^m(\boldsymbol{\theta}), \qquad (4.29)$$

where $f_{nl} = \int_{\mathbb{S}^2} f(\boldsymbol{\theta}) Y_{|m|+l}^m(\boldsymbol{\theta}) d\boldsymbol{\theta}$.

Obviously from this unusual notation of the spherical harmonics expansion, the set of ordered parameter-pairs yields $\mathcal{N} := \{(|m| + l, m) : l \in \mathbb{N}_0, m \in \mathbb{Z}\}$ and clearly $\mathcal{S}^2 := \{\boldsymbol{\theta}\} = \mathbb{S}^2$. As above, by indexing the parameter-pairs in ascending lexicographical order, the spherical harmonics expansion is expressed by eq. (4.23), and eqs. (4.26) to (4.28) hold. In contrast to the angular solutions on partial spherical surfaces, in this case we can express the index q explicitly as a function of order and degree, $q = n^2 + n + m + 1$, cf. [Zot09a, p. 67].

4.2 Homogeneous solution, interior and exterior problem

This is the generalization of section 2.2.1. Having sound-hard boundaries at coordinate surfaces in ϕ and/or θ, the homogeneous solution of the Helmholtz equation for corresponding bounded region in $\mathbb{R}^3$ is of the general form

$$p(\boldsymbol{r}) = \sum_{q=1}^{\infty} \left(b_q\, j_{\nu_q}(kr) + c_q\, h_{\nu_q}^{(2)}(kr) \right) Y_{\nu_q}^{\mu_q}(\boldsymbol{\theta}). \qquad (4.30)$$

This equation expresses any sound field in the source-free region $\Omega := \{\boldsymbol{r} \in \mathbb{R}^3 : \mathrm{r}_e \leq r \leq \mathrm{r}_i, \boldsymbol{\theta} \in \mathcal{S}^2\}$, see fig. 4.6a, whereby the partial spherical surface $\mathcal{S}^2$ corresponds to the angular boundary conditions, i.e. $\mathcal{S}^2$ can be either a spherical cap, zone, lune, quadrangle, cf. eq. (4.24), or the unit-sphere $\mathbb{S}^2$.

Interior problem. In case of $r_e = 0$, Ω includes the singular point of the spherical Bessel differential equation at $r = 0$, see fig. 4.6b. Clearly, as for the integer order functions, only the spherical Bessel functions fulfill the differential equation at $r = 0$ and hence eq. (4.30) reduces to

$$p(\boldsymbol{r}) = \sum_{q=1}^{\infty} b_q \, j_{\nu_q}(kr) \, Y_{\nu_q}^{\mu_q}(\boldsymbol{\theta}). \tag{4.31}$$

Exterior problem. In case of $r_i = \infty$, see fig. 4.6c, the radial solutions are required to fulfill the radiation condition, cf. eq. (2.19). Also in case of non-integer order, only, the spherical Hankel functions of the second kind fulfill this requirement, and eq. (4.30) reduces to

$$p(\boldsymbol{r}) = \sum_{q=1}^{\infty} c_q \, h_{\nu_q}^{(2)}(kr) \, Y_{\nu_q}^{\mu_q}(\boldsymbol{\theta}). \tag{4.32}$$

4.3 Green's function and plane waves

Green's function. Convolution with Green's function is the inverse to the Helmholtz operator, and hence the particular solution of the inhomogeneous Helmholtz equation, cf. eq. (2.21), fulfilling prescribed angular boundary conditions is determined by convolving Green's function for this problem with the excitation, see eq. (2.23). The Green's function fulfills the Helmholtz equation excited by a delta distribution, cf. eq. (2.22), and the prescribed angular boundary conditions. The general construction of Green's function is shown in appendix A. Inserting eq. (A.24) in eq. (A.17) yields Green's function with no explicit boundary condition in r,

$$G(\boldsymbol{r}, \boldsymbol{r}_0) = -ik \sum_{q=1}^{\infty} Y_{\nu_q}^{\mu_q}(\boldsymbol{\theta}) Y_{\nu_q}^{\mu_q}(\boldsymbol{\theta}_0) \begin{cases} j_{\nu_q}(kr) h_{\nu_q}^{(2)}(kr_0) & \text{for } r \leq r_0, \\ j_{\nu_q}(kr_0) h_{\nu_q}^{(2)}(kr) & \text{for } r \geq r_0, \end{cases} \tag{4.33}$$

whereby $Y_{\nu_q}^{\mu_q}(\boldsymbol{\theta})$ are the angular solutions according to the prescribed boundary conditions in uniform notation, as established in section 4.1.5. This ensures that the prescribed boundary conditions hold also for $G(\boldsymbol{r}, \boldsymbol{r}_0)$.

Scattered plane wave. Obviously, a "pure" plane wave can not expressed by the series expansion eq. (4.31), as the solutions are fulfilling the prescribed boundary conditions. However, the sound pressure due to a plane wave scattered by the

(a) general problem

(b) interior problem
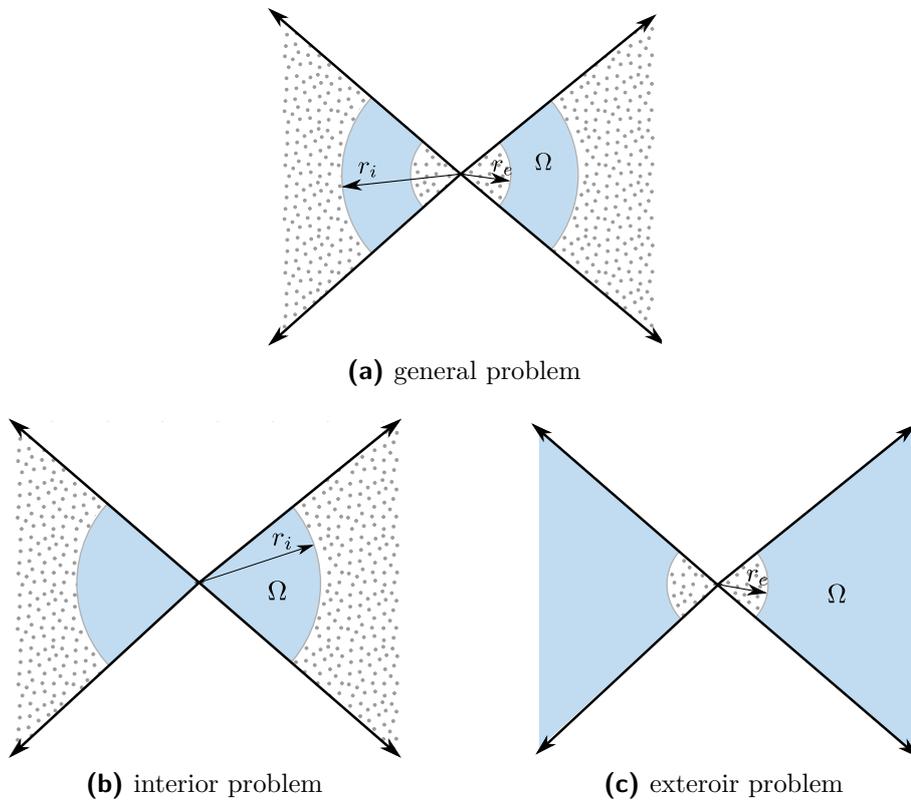
(c) exteroir problem

Figure 4.6: Source-free region Ω (blue) for a double-conical boundary condition in θ for a (a) the general problem, (b) interior problem and (c) exterior problem. The graphics show a cross section in ϕ through the origin, whereby the bold arrows are the intersection lines with the rigid infinite conical boundaries.
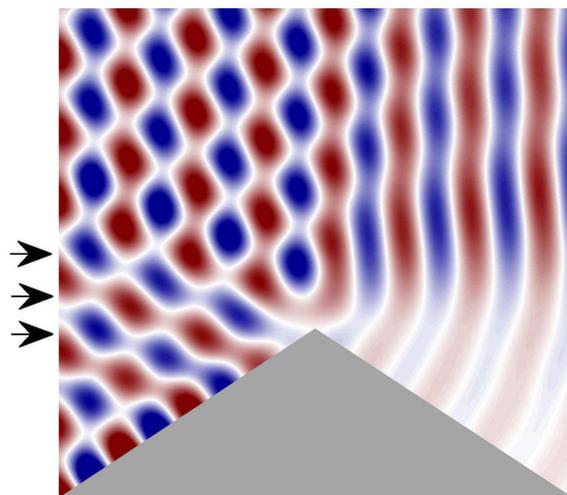
Figure 4.7: Sound pressure of plane wave scattered by a rigid infinite cone on a cross section in ϕ through the origin. The gray surface indicates the cone; the arrows indicate the incident direction.

angular boundary surfaces is derived in the same way as a plane wave in free field, cf. section 2.2.2. Considering the asymptotic equivalent of the spherical Hankel function[3], $h_\nu^{(2)}(x) \sim i^{\nu+1} x^{-1} e^{-ix}$ for $x \to \infty$ [DLMF, §10.52(ii)], the asymptotic equivalent of Green's function follows from eq. (4.33),

$$G(\boldsymbol{r}, \boldsymbol{r}_0) \sim \frac{e^{-ikr_0}}{r_0} \sum_{q=1}^{\infty} i^{\nu_q} j_{\nu_q}(kr) Y_{\nu_q}^{\nu_q}(\boldsymbol{\theta}) Y_{\nu_q}^{\nu_q}(\boldsymbol{\theta}_0), \quad r_0 \to \infty. \tag{4.34}$$

Multiplying the right side of the above equation by $A\, r_0 e^{ikr_0}$ yields the sound pressure of a scattered plane wave,

$$p(\boldsymbol{r}) = A \sum_{q=1}^{\infty} i^{\nu_q} j_{\nu_q}(kr) Y_{\nu_q}^{\mu_q}(\boldsymbol{\theta}) Y_{\nu_q}^{\mu_q}(\boldsymbol{\theta}_0), \tag{4.35}$$

where $A = \int_{\mathcal{S}^2} d\boldsymbol{\theta}$ is the area of the fraction of the unit sphere enclosed by the boundaries. For illustration, fig. 4.7 shows the sound pressure for a conical boundary condition, on a cross section in ϕ through the origin .

---

[3]The properties and relations for the spherical Bessel and Hankel functions are frequently stated only for $\nu = n$, where n is an integer. However most of these relations hold for also for non-integer parameters and can be derived from the corresponding relations for $J_\nu(x)$ and $H_\nu(x)$, which are usually given without a restriction to integer parameters.

Chapter 5

Partial spherical microphone arrays with rigid angular boundaries

As shown in the previous chapter, the solutions of the Helmholtz equation in the presence of rigid angular boundaries are structural similar to those of a free field. In this chapter we will discuss the application of these theoretical results for modal sound field decomposition with partial spherical arrays, i.e. a set of microphones suitably distributed on a partial spherical surface $\mathcal{S}^2 \subset \mathbb{S}^2$ enclosed by the according rigid coordinate surfaces. Within this work, we only consider partial spherical arrays on a rigid partial spherical surface. Similarly as for spherical microphone arrays, open partial spherical arrays using cardioid microphones or concentric dual partial spherical arrays are also an option, but are not within the focus of this work.

5.1 Modal sound field decomposition

The sound pressure of an incident field, bounded by rigid angular boundary conditions and a rigid partial spherical surface at $r = r_m$, is derived from eqs. (4.31) and (4.32). The radial boundary condition $\left.\frac{\partial p(\boldsymbol{r})}{\partial r}\right|_{r=r_m} = 0$ is fulfilled by setting

$$c_q = -b_q \frac{j'_{\nu_q}(kr_m)}{h'^{(2)}_{\nu_q}(kr_m)}.$$

(5.1)

This yields

$$p(\boldsymbol{r}) = \sum_{q=1}^{\infty} b_q \left(j_{\nu_q}(kr) - \frac{j'_{\nu_q}(kr_m)}{h'^{(2)}_{\nu_q}(kr_m)} h^{(2)}_{\nu_q}(kr) \right) Y^{\mu_q}_{\nu_q}(\boldsymbol{\theta}).$$

(5.2)

Setting $r = r_m$ in the above equation yields the pressure distribution on the rigid partial spherical surface and using the Wronskian relation $\mathscr{W}\left\{j_\nu(kr), h_\nu^{(2)}(kr)\right\} = j_\nu(kr)h_\nu'^{(2)}(kr) - h_\nu^{(2)}(kr)j_\nu'(kr) = -i(kr)^{-2}$ we get

$$p(r_m\boldsymbol{\theta}) = -i(kr_m)^{-2} \sum_{q=1}^{\infty} \frac{b_q}{h_{\nu_q}'^{(2)}(kr_m)} Y_{\nu_q}^{\mu_q}(\boldsymbol{\theta}). \tag{5.3}$$

For notational convenience, we express the infinite sum by an infinite matrix product

$$p(r_m\boldsymbol{\theta}) = -i(kr_m)^{-2} \, \boldsymbol{y}^{\mathrm{T}}(\boldsymbol{\theta}) \, diag\{\boldsymbol{h}'(kr_m)\}^{-1}\boldsymbol{b}, \tag{5.4}$$

whereby

$$\boldsymbol{y}(\boldsymbol{\theta}) := [Y_{\nu_1}^{\mu_1}(\boldsymbol{\theta}), Y_{\nu_2}^{\mu_2}(\boldsymbol{\theta}), Y_{\nu_3}^{\mu_3}(\boldsymbol{\theta}), \ldots]^{\mathrm{T}},$$
$$\boldsymbol{h}'(kr_m) := [h_{\nu_1}'^{(2)}(kr_m), h_{\nu_2}'^{(2)}(kr_m), h_{\nu_3}'^{(2)}(kr_m), \ldots]^{\mathrm{T}}, \tag{5.5}$$
$$\boldsymbol{b} := [b_1, b_2, b_3, \ldots]^{\mathrm{T}}.$$

The array microphones sample the pressure pattern $p(r_m\boldsymbol{\theta})$ on the partial spherical surface at M discrete positions $\boldsymbol{\theta}_i$, $i = 1, 2, \ldots, \mathrm{M}$. The discretized pressure pattern $\boldsymbol{p} := [p(r_m\boldsymbol{\theta}_1), \ldots, p(r_m\boldsymbol{\theta}_\mathrm{M})]^{\mathrm{T}}$ yields

$$\boldsymbol{p} = -i(kr_m)^{-2} \, \boldsymbol{Y} \, diag\{\boldsymbol{h}'(kr_m)\}^{-1}\boldsymbol{b}, \tag{5.6}$$

whereby

$$\boldsymbol{Y} := [\boldsymbol{y}(\boldsymbol{\theta}_1), \ldots, \boldsymbol{y}(\boldsymbol{\theta}_i), \ldots, \boldsymbol{y}(\boldsymbol{\theta}_\mathrm{M})]^{\mathrm{T}}. \tag{5.7}$$

Similar as for conventional spherical microphone arrays, it is convenient to characterize the incident sound field by a continuous partial spherical source distribution $f(\boldsymbol{\theta})$, $\boldsymbol{\theta} \in \mathcal{S}^2$, at some radius $r_s > r_m$. Typically, one chooses $r_s \to \infty$ for characterizing the far-field directivity pattern of a beamformer, whereas r_s is set to the radius of a surrounding spherical loudspeaker array for reproducing the sound field. Expanding the source distribution in partial spherical harmonics yields

$$f(\boldsymbol{\theta}) = \sum_{q=1}^{\infty} \phi_q \, Y_{\nu_q}^{\mu_q}(\boldsymbol{\theta}). \tag{5.8}$$

Green's function, $G(\boldsymbol{r}, \boldsymbol{r}_0)$, for the domain Ω, bounded by the rigid angular boundaries and the rigid partial spherical surface, is achieved by inserting eq. (A.23) in eq. (A.17) and $\Omega := \{\boldsymbol{r} \in \mathbb{R}^3 : r_s \leq r \leq r_m, \boldsymbol{\theta} \in \mathcal{S}^2\}$. Evaluating the

sound pressure by convolving the source distribution with Green's function, $p(\boldsymbol{r}) = \int_\Omega G(\boldsymbol{r}, \boldsymbol{r}_0) f(\boldsymbol{\theta}_0) \delta(r_0 - r_s) \, r^{-2} \, d\boldsymbol{r}_0$, and comparing the result for $r < r_s$ to eq. (5.2), reveals the connection between the coefficients of the incident field and the partial spherical source distribution

$$b_q = -ikh^{(2)}_{\nu_q}(kr_s)\phi_q. \tag{5.9}$$

Hence, eq. (5.6) is equivalently expressed in terms of a partial spherical source distribution by

$$\boldsymbol{p} = \boldsymbol{Y} \; diag\{\boldsymbol{w}(k, r_m, r_s)\}\boldsymbol{\phi}, \tag{5.10}$$

whereby

$$\boldsymbol{w}(k, r_m, r_s) := [w_{\nu_1}(k, r_m, r_s), w_{\nu_2}(k, r_m, r_s), w_{\nu_3}(k, r_m, r_s), \dots]^{\mathrm{T}},$$

$$w_{\nu_q}(k, r_m, r_s) := -\frac{h^{(2)}_{\nu_q}(kr_s)}{kr_m^2 h^{\prime(2)}_{\nu_q}(kr_m)}. \tag{5.11}$$

In general, eq. (5.10) is formally highly undetermined and has an infinitude of solutions. Hence a direct inversion of eq. (5.6) is not feasible without any further assumptions.

The objective of modal sound field decomposition is to determine an optimal estimate $\hat{\boldsymbol{\phi}}_{\mathrm{N}} := [\hat{\phi}_1, \dots, \hat{\phi}_q, \dots, \hat{\phi}_{\mathrm{Q}}]^{\mathrm{T}}$, $\nu_q \leq \mathrm{N}$, of the first Q elements of $\boldsymbol{\phi}$ from the angularly sampled sound pressure distribution $\boldsymbol{p}$. We assume that the pressure distribution sampled by the array is spatially band-limited, i.e. modal components of the source distribution with $q > \mathrm{N}$ do not contribute to the pressure distribution at the array surface. Choosing $\mathrm{M} = \mathrm{Q}$, $\boldsymbol{\phi}_{\mathrm{N}}$ is related to $\boldsymbol{p}$ by a square matrix. In this case the problem yields a unique solution, which is determined by matrix inversion,

$$\boldsymbol{\phi}_{\mathrm{N}} = diag\{\boldsymbol{w}_{\mathrm{N}}(k, r_m, r_s)\}^{-1} \, \boldsymbol{Y}_{\mathrm{N}}^{-1}\boldsymbol{p}, \tag{5.12}$$

whereby $\boldsymbol{Y}_{\mathrm{N}} := [\boldsymbol{y}_{\mathrm{N}}(\boldsymbol{\theta}_1), \dots, \boldsymbol{y}(\boldsymbol{\theta}_{\mathrm{M}})]^{\mathrm{T}}$, with $\boldsymbol{y}_{\mathrm{N}}(\boldsymbol{\theta}) := [Y^{\mu_1}_{\nu_1}(\boldsymbol{\theta}), \dots, Y^{\mu_{\mathrm{Q}}}_{\nu_{\mathrm{Q}}}(\boldsymbol{\theta})]^{\mathrm{T}}$, and $\boldsymbol{w}_{\mathrm{N}}(k, r_m, r_s) := [w_{\nu_1}(k, r_m, r_s), \dots, w_{\nu_{\mathrm{Q}}}(k, r_m, r_s)]^{\mathrm{T}}$. Clearly, $\boldsymbol{Y}_{\mathrm{N}}$ and $diag\{\boldsymbol{w}_{\mathrm{N}}(k, r_m, r_s)\}$ are both required to be well-conditioned to achieve useful results under real-world conditions, like e.g. additive noise.

The condition number of $\boldsymbol{Y}_{\mathrm{N}}$ depends on the distribution of the sampling points over the partial spherical surface. In contrast to sampling a spherical surface, where various samplings strategies are available, see e.g. [Zot09b], there are rarely publications

on sampling strategies for partial spherical surfaces. Sampling strategies for partial spherical surfaces are discussed in more detail in section 5.2.

Frequency limits. A lower and an upper frequency limit can be defined for modal sound field decomposition, which both are derived from $\boldsymbol{w}_{\mathrm{N}}(k, r_m, r_s)$. In the following we assume that source distribution $f(\boldsymbol{\theta})$ is in the far field, i.e. $r_s \to \infty$. Using the asymptotic equivalent of the spherical Hankel function, $h_\nu^{(2)}(x) \sim i^{\nu+1} x^{-1} e^{-ix}$ for $x \to \infty$ [DLMF, §10.52(ii)], we have

$$w_{\nu_q}(k, r_m, r_s) \sim \frac{e^{-ikr_s}}{r_s} \cdot \frac{i^{\nu_q - 1}}{(kr_m)^2 h_{\nu_q}^{\prime(2)}(kr_m)}. \tag{5.13}$$

The first fraction on the right side in the above equation represents the common attenuation and delay of all components. Therefore, we discard the first fraction, define

$$w_{\nu_q}(kr_m) := \frac{i^{\nu_q - 1}}{(kr_m)^2 h_{\nu_q}^{\prime(2)}(kr_m)}, \tag{5.14}$$

and replace $\boldsymbol{w}_{\mathrm{N}}(k, r_m, r_s)$ in eq. (5.12) by

$$\boldsymbol{w}_{\mathrm{N}}(kr_m) := [w_{\nu_1}(kr_m), \ldots, w_{\nu_Q}(kr_m)]^{\mathrm{T}}. \tag{5.15}$$

In almost all cases this assumption holds also for sound field reproduction applications as typically $r_s \gg r_m$.

Lower frequency limit. For a fixed array radius, $\boldsymbol{w}_{\mathrm{N}}(kr_m)$ depends on k, only, i.e. it is frequency dependent, and its elements are a set of frequency responses. The inverse of these frequency responses define the diagonal matrix in eq. (5.12), as $diag\{\boldsymbol{w}_{\mathrm{N}}(kr_m,)\}^{-1} = diag\{w_{\nu_1}^{-1}(kr_m), \ldots, w_{\nu_Q}^{-1}(kr_m)\}$, and $w_{\nu_q}^{-1}(kr_m)$ is referred to as radial filter. The rigid array surface ensures that $w_{\nu_q}(kr_m)$ is invertible, as in this case $|w_{\nu_q}(kr_m)| > 0$. In contrast, it shows that for an open array $w_{\nu_q}(kr_m)$ has isolated zeros in kr_m, as it involves the spherical Bessel function. From the asymptotic equivalent of the spherical Hankel function, $h_\nu^{(2)}(x) \sim i \frac{1}{\sqrt{\pi}} 2^\nu \Gamma\left(\nu + \frac{1}{2}\right) x^{-\nu-1}$ for $x \to 0$ [DLMF, §10.52(i)], it shows that

$$w_{\nu_q}^{-1}(kr_m) \sim -i \frac{1}{\sqrt{\pi}} 2^{\nu_q} \Gamma\left(\nu_q + \frac{1}{2}\right) (\nu_q + 1) (kr_m)^{-\nu_q} \quad \text{for } kr_m \to 0. \tag{5.16}$$

This reveals that the magnitude of $w_{\nu_q}^{-1}(kr_m)$ grows towards low frequencies up to ∞, except for $\nu_q = 0$, and the growth rate is determined by ν_q. For a practical application

$|w_{\nu_q}^{-1}(kr_m)|$ has to be limited to a maximally acceptable filter gain. This determines the lower frequency limit, down to which modal sound field decomposition is permissible for a given maximum order ν_Q. Figure 5.1 depicts $|w_\nu^{-1}(kr_m)|$ in dependence of kr_m and ν_q. The black dashed contour lines server as examples for a maximal acceptable filter gain. The gray dotted lines represent the estimated contour lines, determined from low frequency approximation according to eq. (5.16). Obviously, the estimated values deviate from the true contours for large values kr_m, as the approximation is not valid for large arguments.

As it is common practice with spherical microphone arrays, the lower frequency limit is shifted down by reducing the spatial resolution. This is achieved by step-wise lowering the maximal decomposition order to $\nu_{Q'} \leq N' < \nu_Q$, such that $|w_{\nu_{Q'}}(kr_m)^{-1}|$ does not to exceed the specified maximum gain down to a lower value of kr. The stable implementation of $w_{\nu_q}(kr_m)^{-1}$ as a discrete-time filter will be discussed in section 5.3.

Upper frequency limit. Conversely, there is an upper frequency limit above which the wave spectrum of an incident field is not ensured to be spatially band-limited, i.e. above this frequency limit there is a significant contribution of higher order components. For spherical microphone arrays, $kr_m \leq N$ is usually used as a rule of thumb to estimate the upper frequency limit. The motivation therefore is the fact that $|w_n(kr)|$ decreases in n for a $n > kr$. Hence, the contribution of order larger than N to the sound pressure on the array surface is expected to die down, and the assumption of a spatially band-limited pressure distribution will be approximately valid, cf. [Raf04].

As $|w_\nu(kr)|$ is a monotonically decreasing function in ν for about $\nu > kr$, see fig. 5.2, also the sequence $(|w_{\nu_1}(kr)|, |w_{\nu_2}(kr)|, \ldots, |w_{\nu_q}(kr)|, \ldots)$ decreases for a particular angular boundary condition, as we defined q such that $\nu_q \leq \nu_{q+1}$. Hence, with the same argumentation as for spherical arrays, the upper frequency limit for a partial spherical microphone array is roughly estimated by the rule of thumb

$$kr_m \leq \nu_Q \leq N. \tag{5.17}$$

Note that for a detailed analysis of spatial aliasing the particular incident sound field as well as the distribution of the sampling points have to be considered.
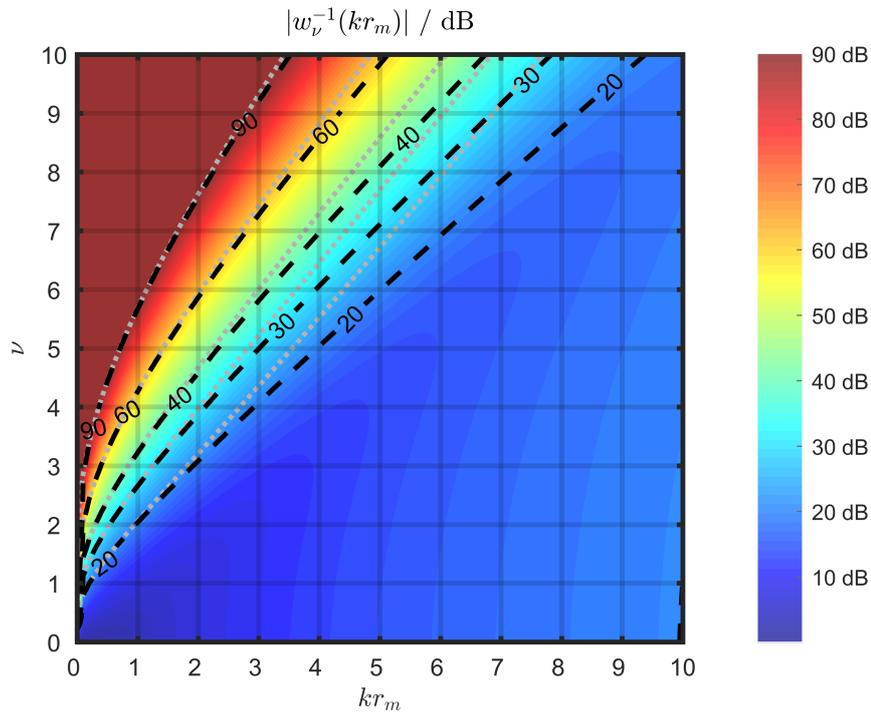
Figure 5.1: Gain of the radial filter $|w_\nu^{-1}(kr_m)|$ in dependence of ν and kr_m. The black dashed contour lines server as examples for a maximal acceptable gain value. The gray dotted lines represent the estimated contour lines determined from the low frequency approximation according to eq. (5.16).
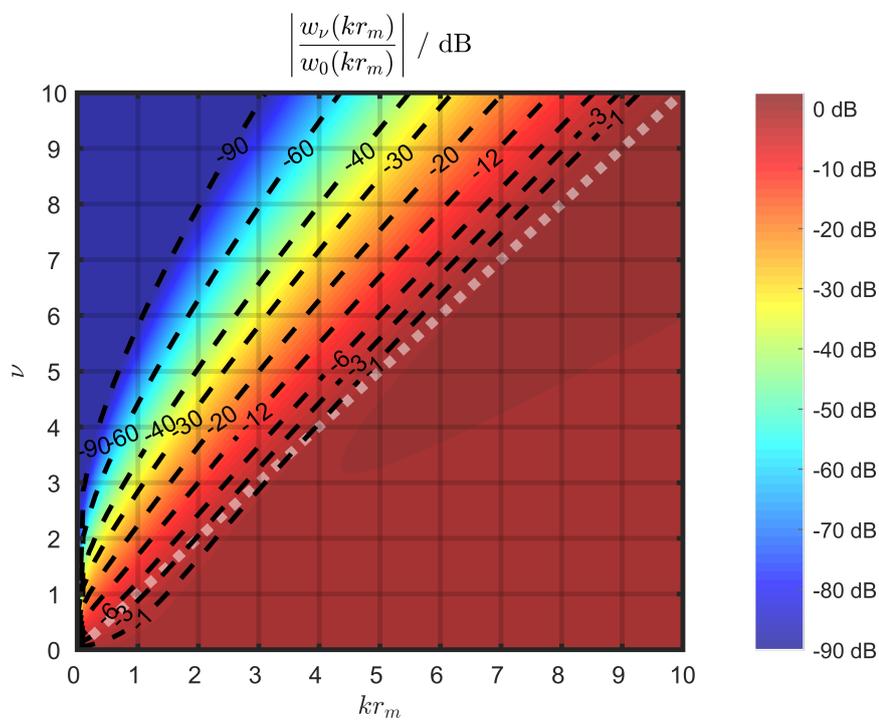
Figure 5.2: $|w_\nu(kr_m)|$ normalized to $|w_0(kr_m)|$ as a function of ν and kr_m. The white dotted line indicates $\nu = kr$.

5.2 Sampling partial spherical surfaces

A sampling strategy shall provide a set of discrete points on a partial spherical surface, which allows for a discrete partial spherical harmonics transform of spatially band-limited functions. Thereby the sampling is required to be efficient in terms of the number of sampling points, and robust to additive errors arising from measuring the sampled quantity, e.g. additive noise, positioning errors.

To analyze sampling efficiency and error sensitivity, we assume a spatially band-limited function $g(\boldsymbol{\theta})$ on $\mathcal{S}^2$, i.e. $\int_{\mathcal{S}2} g(\boldsymbol{\theta})Y_{\nu_q}^{\mu_q}(\boldsymbol{\theta})d\boldsymbol{\theta} = 0$ for $q > Q$, where $\nu_Q \leq N$. The discrete partial spherical harmonics series of $g(\boldsymbol{\theta})$, sampled angularly at $\{\boldsymbol{\theta}_i\}_{i=1,\dots,M}$, can be expressed by the matrix equation

$$\boldsymbol{g} = \boldsymbol{Y}_{\mathrm{N}}\boldsymbol{\gamma}_{\mathrm{N}}, \tag{5.18}$$

where $\boldsymbol{g} := [g(\boldsymbol{\theta}_1), \dots, g(\boldsymbol{\theta}_M)]^{\mathrm{T}}$ is a vector containing the set of discrete angular samples, $\boldsymbol{\gamma}_{\mathrm{N}} := [\gamma_1, \dots, \gamma_Q]^{\mathrm{T}}$ is a vector containing the expansion coefficients, and $\boldsymbol{Y}_{\mathrm{N}}$ is a $M \times Q$ matrix as defined for eq. (5.12). Equation (5.18) is overdetermined for $M > Q$ and underdetermined for $M < Q$. Hence $M \geq Q$ is required for a unique solution. As we desire a most efficient sampling scheme, i.e. $M = Q$, we focus the discussion on this case. The solution to eq. (5.18) is the discrete partial spherical harmonics transform,

$$\boldsymbol{\gamma}_{\mathrm{N}} = \boldsymbol{Y}_{\mathrm{N}}^{-1}\boldsymbol{g}. \tag{5.19}$$

The data in $\boldsymbol{g}$ is to some extend corrupted by measurement errors, and thus $\boldsymbol{Y}_{\mathrm{N}}$ is required to be well-conditioned. The problem is said to be well conditioned if the ratio of the relative error in $\boldsymbol{\gamma}_{\mathrm{N}}$ to the relative error in $\boldsymbol{g}$ is sufficiently small. If we use the 2-norm as an error measure, the upper bound of this ratio is equivalent to the ratio of the largest to the smallest singular value of $\boldsymbol{Y}_{\mathrm{N}}$, see [GV96, §2.7.2]. This value is referred to as the condition number number,

$$\kappa\left(\boldsymbol{Y}_{\mathrm{N}}\right) = \frac{\sigma_{\max}(\boldsymbol{Y}_{\mathrm{N}})}{\sigma_{\min}(\boldsymbol{Y}_{\mathrm{N}})} \geq 1, \tag{5.20}$$

where $\{\sigma_i(\boldsymbol{Y}_{\mathrm{N}})\}$ is the set of singular values of $\boldsymbol{Y}_{\mathrm{N}}$. Hence an optimal sampling strategy finds a set of sampling points $\{\boldsymbol{\theta}_i\}_{i=1,\dots,M}$ with $M = Q$, for which $\kappa(\boldsymbol{Y}_{\mathrm{N}})$ is minimal.

Minimizing the condition number. Minimizing the condition number of a Gram matrix, defined by a polynomial basis and a set of points, is neither a convex nor a

smooth problem. This is shown in [CWY11], and there is an example given, where the condition number of the Gram matrix arising from sampled spherical harmonics is minimized. Minimization the condition number for partial spherical harmonics is a similar problem, and thus the properties of the cost function are the same. Interestingly, the non-smoothness of the condition number is related to the singular values. The condition number may be non-smooth if either the largest or the smallest singular value is not simple, cf.[YZ13]. Due to the non-convexity of the problem, it is not guaranteed that an optimization reaches the global minimum. The non-smoothness of the problem implies that efficient gradient methods can not be applied, since the cost function is not differentiable everywhere.

One strategy to avoid these problems is to minimize the condition not directly. Instead, the sampling points are optimized due to other criteria, which are expected to be related to a low condition number. In [Köß11], different approaches to optimize a microphone distribution on a spherical cap have been compared to a direct minimization of the condition number. The indirect optimization methods relied either on a minimum energy approach, in terms of repellent charges, or on geometrical regularity, in terms of Voronoi cells, whereby the minimum energy approach yielded insufficient results[1]. Starting from the same initial point distribution, it showed that the geometrical optimization achieved better results than the direct minimization. Obviously, the direct minimization converges to some local minimum of condition number, depending on the initial distribution. This illustrates the nonconvex nature of the problem.

Furthermore, an optimization approach using a fixed grid on spherical cap was presented in [Köß11]. This approach was developed further in [Pau13], where it was applied to find sampling points for spherical segment harmonics. In [Pau13] a prototype of a microphone array on a rigid spherical zone bounded by a rigid double cone was developed. Further details on this prototype are given in section 5.6. The proposed optimization aims at more robustness against local minima and is based on a fine discrete grid of points on the partial spherical surface. The initial point set is distributed randomly on the grid. In the optimization, the condition number tested for moving single points sequentially to all vacant grid positions, and then the point is placed on the position with the lowest condition number. This operation is repeated for all remaining sampling points in random order. If the condition number of the point distribution after one such run, i.e. moving all points once, is lower than

---

[1]The author in [Köß11] suspected that better results can be achieved with a more suitable charge distribution representing the angular boundary. However, the last example in [CWY11] reveals that even for a full spherical surface the minimum energy points can have very large condition numbers.
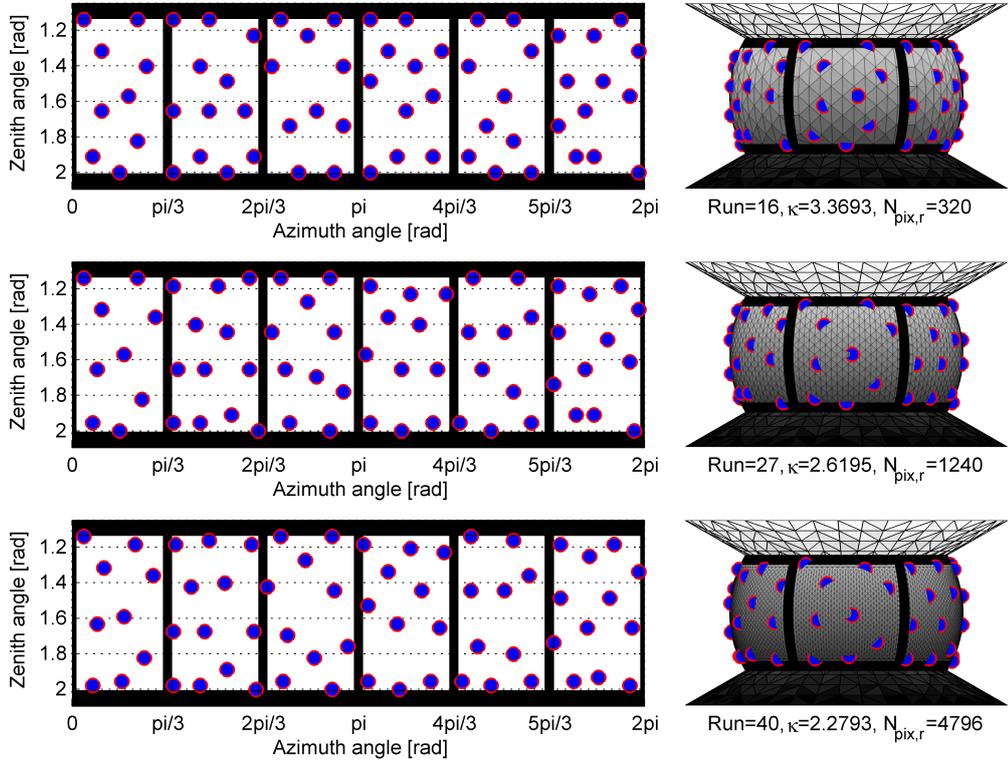
Figure 5.3: Intermediated results of the optimization algorithm proposed in [Pau13]. The right column shows the perspective view on the spherical zone bounded by a double cone, and the left column provides the unrolled surface of the zone. The rows represent different grid refinements, whereby from top to bottom the number of grid points is 320, 1240 and 4796. The location of the grid points is indicated by the intersection of the thin black lines in the perspective view. The red circles, filled with blue, indicate the current sampling position. The black areas represent regions where no sampling points are allowed due to constructive joints. The bottom row corresponds to the final sampling positions, which achieve a condition number $\kappa(\mathbf{Y}_N) \approx 2.3$, [Pau13].

before, it is used as initial condition for the next run. If there is no improvement between consecutive runs, the grid resolution is increased for the next run. If there is no improvement with the denser grid, the optimization is aborted. Figure 5.3 illustrates the progress of the optimization. Regions on the partial spherical surface, which are not feasible, e.g. due to constructional issues as in the vicinity of the angular boundaries or joints of the rigid elements, are easily excluded from the discrete grid. Clearly, this optimization is a kind of Greedy algorithm and it is not guaranteed that it achieves the overall global minimum. This is the price payed for the reduced complexity, but, as the results in [Pau13] suggest, the algorithm delivers a good local minimum. However, to achieve the final result, the optimization algorithm was fed with several random initial point sets, and the best result therefrom was used.
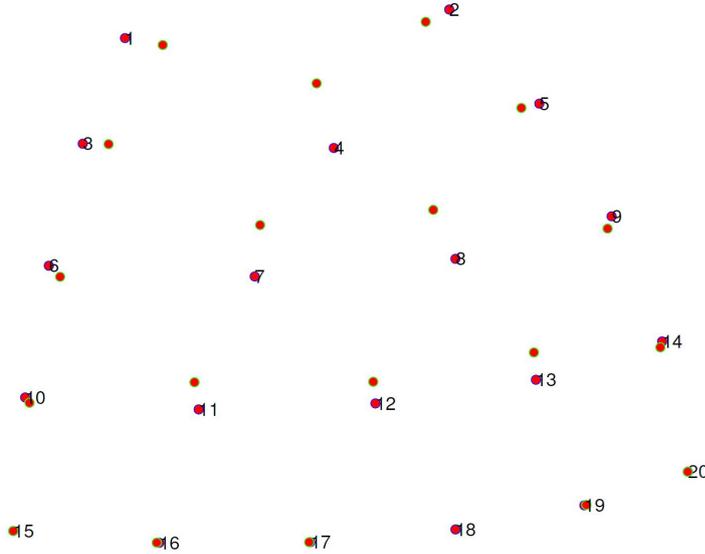
Figure 5.4: Optimized sampling points on a spherical quadrangle. The blue circles, filled with red, indicate the initial sampling points determined by Greedy selection, achieving $\kappa(\boldsymbol{Y}_{\mathrm{N}}) \approx 4$, and the green circles, filled with red, indicate the final sampling points achieved by direct minimization of the condition number, achieving $\kappa(\boldsymbol{Y}_{\mathrm{N}}) \approx 1.45$.

In [Kel15; KZ15], a direct minimization approach was applied to determine sampling points on a spherical quadrangle. Although the target application is here the synthesis of highly directive radiation patterns, the sampling problem is similar to a partial spherical microphone array. The minimization of the condition number was conducted by MATLAB's *unconstrained nonlinear least-squares algorithm*, whereby the initial distribution of sampling points was determined by a Greedy selection algorithm. For the Greedy selection a fine grid of discrete points on the spherical quadrangle is used, and one initial point is chosen. The next point is chosen such that the condition number of the matrix of spherical quadrangle harmonics sampled at the chosen points is minimal. In this way sampling points are added until the matrix is square. The initial set of sampling points for a spherical quadrangle determined by Greedy selection, and the final set achieved from direct minimization of the condition number are shown in fig. 5.4. Constructional constraints as a minimum distance between the sampling points and to the angular boundary were ensured in the direct minimization by adding a strong penalty to the condition number.

As stated in [CWY11] and illustrated by the above examples, the nonconvex problem of minimizing the condition number of a matrix, defined by a set of sampling points and a set of orthogonal basis functions, typically has many local minima and one has to settle for a good local minimum, which might not be the global one.

5.3 Implementation of radial filters

Whereas the angular decomposition in eq. (5.12) is a frequency independent matrix multiplication, the radial part is frequency dependent and for a practical application requires a suitable implementation in terms of discrete time filter operations. These radial filter shall approximate either $w_{\nu_q}^{-1}(k, r_m, r_s)$, cf. eq. (5.11), or $w_{\nu_q}^{-1}(kr_m)$, cf. eq. (5.14), in case of assuming the source distribution to be in the far-field.

If $\nu = n \in \mathbb{N}$, as for a spherical microphone arrays, the explicit formula for spherical Hankel function of the second kind is, cf. [DLMF, eq. 10.49.7],

$$h_n^{(2)}(z) = -i^n \frac{e^{-iz}}{(iz)^{n+1}} \sum_{l=0}^{n} \frac{(n+l)!}{l!(n-l)!2^l}(iz)^{n-l} \tag{5.21}$$

The sum in the above equation represents a finite order polynomial, and this allows for a very elegant infinite impulse response (IIR) filter implementation for spherical arrays, see [Pom08; Lös14; BPF11].

The generalization of eq. (5.21) to non-integer values of ν is the relation

$$h_\nu^{(2)}(z) = e^{-iz}\, e^{i(\nu+1)\pi}\, 2^{\nu+1}\, z^\nu\, U(\nu+1, 2\nu+2, 2iz), \tag{5.22}$$

whereby $U(a, b, z)$ is the confluent hypergeometric function of the second kind, cf. [DLMF, §13]. The above relation is achieved by combining [DLMF, eq. 10.16.6] with eq. (C.12). In general, $U(\nu+1, 2\nu+2, 2iz)$ is an infinite series for $\nu \neq n$. Hence, for partial spherical arrays the radial filters can not be implemented in the same way as for a spherical arrays.

Causality. Equation (5.22) reveals that the spherical Hankel function in general contains the term e^{-iz}, which represents a delay in the time domain, for $z = kr$. To avoid acausal radial filters, we discard this delay and replace the radial term in eq. (5.12) by either

$$\mathsf{w}_{\nu_q}(kr_m) := \frac{i^{\nu_q}}{k^2 h'^{(2)}_{\nu_q}(kr_m)} e^{ikr_m}, \text{ or} \tag{5.23}$$

$$\mathsf{w}_{\nu_q}(k, r_m, r_s) := \frac{h^{(2)}_{\nu_q}(kr_s)}{k h'^{(2)}_{\nu_q}(kr_m)} e^{ik(r_m - r_s)}, \tag{5.24}$$

where in the latter definition we also dropped the constant factor $-r_m^{-2}$.

Regularization.   Using the causal radial filters directly, i.e. $\mathsf{w}_{\nu_q}(kr_m)^{-1}$ or $\mathsf{w}_{\nu_q}(k, r_m, r_s)^{-1}$, would lead to strong errors due to their huge magnitude at low frequencies, cf. the discussion in section 5.1 on the condition number of $diag\{\boldsymbol{w}_{\mathrm{N}}(kr_m)\}$. Therefore a suitable gain limitation for the radial filters is required. This can be achieved, as for conventional spherical microphone arrays, either by modifying the frequency domain expressions adequately, see e.g. [BPSW11], before the discrete-time implementation, or by using a suitable filter bank prior to the radial filters in the signal processing chain, see e.g. [Lös14; BPF11].

Discrete-time filter implementation.   The discrete-time implementation of the radial filters is confined to simple approaches here, as this topic is not in the main focus of this thesis. the frequency sampling method, cf.[PB87; Pau13], is the simplest and most direct technique to implement the radial filters as finite impulse response filters (FIR). Thereby the frequency response of the (regularized) radial filter is uniformly sampled in the frequency domain and performing the inverse discrete Fourier transform thereof yields the corresponding impulse response. The results are not optimal as the response may deviate from what is desired between the samples and the FIR filter length has to be chosen sufficiently long to avoid time-domain aliasing. An infinite impulse response filter approximation can be achieved using a complex-curve fitting algorithm as shown in [Köß11]. This algorithm is also based on sampling points in the frequency domain. The quality of the result depends here on the location of the sampling points and the maximal allowed filter order. However, for larger values of ν satisfying results by a reasonable low filter order need a more elaborated distribution of the sampling points over the frequency.

Example.   Exemplarily, we show here radial filters for a microphone array on a rigid spherical zone bounded by rigid double-cone. The array geometry is as for the prototype presented in section 5.6. The simple FIR filter approximation of radial filters for $\nu_q < 6$ is shown in fig. 5.5. The implementation uses the regularization proposed in [BPSW11], limiting the maximum gain to 30dB, and the FIR filter length is 4096 tabs. The dotted light-gray lines indicate magnitude and phase of the non-regularized continuous-time radial filters $\mathsf{w}_{\nu_q}^{-1}(kr_m)$. The deviation between the frequency-domain sampling points is in this case relatively low, but clearly visible especially for the radial filter with $\nu = 0.661$.
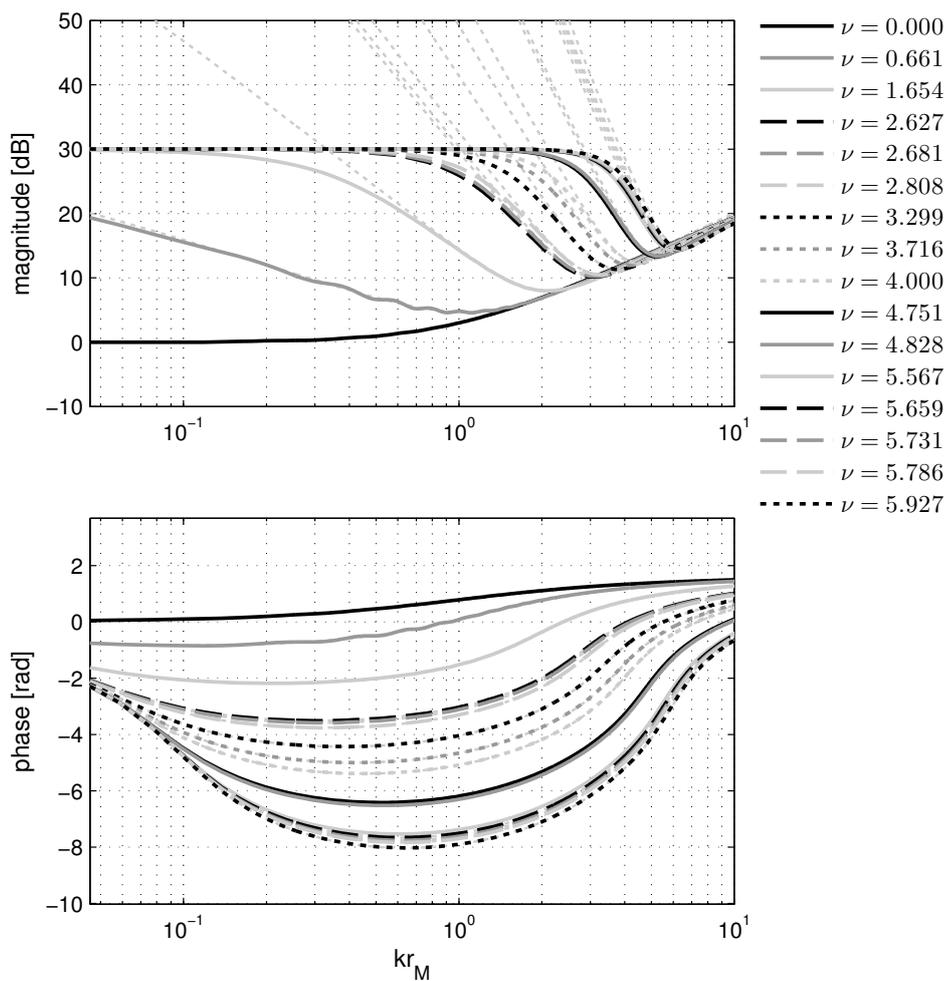
Figure 5.5: Frequency responses of the regularized radial filters for a microphone array on a spherical zone, realized as FIR filters with 4096 tab and a maximum gain of 30 dB. The dotted light-gay lines indicate the frequency responses of the non-regularized continuous-time radial filters $w_{\nu_q}^{-1}(kr_m)$.

5.4 Modal beamformer

We will use the term *modal beamformer*, similar as in [ME02], for the weighted sum of the signal vector $\boldsymbol{\phi}_N(t)$, containing the output signals of the modal sound field decomposition, cf. eq. (5.12), and assuming a far-field source distribution. The output signal of the modal beamformer is expressed by

$$s(t) = \boldsymbol{\gamma}^T(\boldsymbol{\theta}_b) \, \boldsymbol{\phi}_N(t), \tag{5.25}$$

where $\boldsymbol{\gamma}(\boldsymbol{\theta}_b)$ is the steering vector containing the beamformer weights for a desired look-direction $\boldsymbol{\theta}_b$. The partial spherical harmonics of limited order are non-isotropic. Therefore it is not feasible to calculate the beamformer weights for a single direction and then steer the beam to any desired look-direction by a rotation, as shown for spherical arrays in [ME02].

For the basic maximum directivity beamformer the calculation of the steering vector is as simple as for a spherical array, cf. [SYS+10]. However, design methods of more advanced beampatterns for spherical microphone arrays, like e.g. Dolph–Chebyshev designs [KR09], are not directly applicable in the same way for partial spherical arrays.

Maximum-directivity. Assuming an ideal modal sound field decomposition, the directivity pattern $g(\boldsymbol{\theta})$ for an arbitrary steering vector $\boldsymbol{\gamma}^T(\boldsymbol{\theta}_b)$ yields

$$d(\boldsymbol{\theta}) = \boldsymbol{\gamma}^T(\boldsymbol{\theta}_b) \, \boldsymbol{y}_N(\boldsymbol{\theta}). \tag{5.26}$$

The directivity factor D is the ratio of the sensitivity in look-direction to the sensitivity to a random sound field with unit power, i.e. random plane waves from all directions $\boldsymbol{\theta} \in \mathcal{S}^2$,

$$D = \frac{A|d(\boldsymbol{\theta}_b)|^2}{\int_{\mathcal{S}^2} |d(\boldsymbol{\theta})|^2 d\boldsymbol{\theta}}, \tag{5.27}$$

where $A = \int_{\mathcal{S}^2} d\boldsymbol{\theta}$ is the surface area of the unit partial spherical surface. Obviously, the directivity factor is maximized by minimizing the denominator in eq. (5.27) while holding the numerator constant. Inserting eq. (5.26) in the above equation yields the following optimization problem, which is equivalent to maximizing the directivity:

$$\min \|\boldsymbol{\gamma}\|_2^2 \,, \quad \text{s.t. } \boldsymbol{\gamma}^T \boldsymbol{y}_N(\boldsymbol{\theta}_b) = 1. \tag{5.28}$$

This constrained minimization problem is solved straightforwardly by the method of Lagrange multipliers, and its solution is

$$\boldsymbol{\gamma}(\boldsymbol{\theta}_b) = \frac{\boldsymbol{y}_{\mathrm{N}}(\boldsymbol{\theta}_b)}{\|\boldsymbol{y}_{\mathrm{N}}(\boldsymbol{\theta}_b)\|_2^2}. \tag{5.29}$$

5.5   Converting partial-sphere array recordings

Spherical arrays with rigid angular boundaries allow for a representation of the sound field in terms of basis functions which are orthogonal on the corresponding partial spherical surface. However, the spatially band-limited set of orthogonal functions is non-isotropic due to rigid boundaries. Hence, direct rendering on a surrounding loudspeaker setup might exhibit direction-dependent panning artifacts which might disturb the perceived spatial image. This is in contrast to conventional Ambisonics employing spherical harmonics, as the spatially band-limited set of spherical harmonics yields an isotropic orthogonal basis on the sphere.

What is more, in conventional Ambisonics the recording setup is formally independent of the playback setup. This independence is based on the assumption that within both steps, recording and playback, the full angular range is considered. However, a fully spherical loudspeaker setups requires an acoustically transparent floor in a practical application for a large audience. Usually this is not feasible in existing rooms and thus hemispherical setups are used. Therefore, there exist playback strategies for partial spherical loudspeaker setups based on spherical harmonics, see e.g. [ZF12; ZPN12]. To make use of these existing playback strategies and to maintain the independence of recording and playback, a suitable conversion of the partial spherical harmonics to conventional spherical harmonics is required.

Due to the angular boundary conditions, the source distribution captured by a partial spherical array is space-limited, i.e.

$$f(\boldsymbol{\theta}) = \begin{cases} \tilde{f}(\boldsymbol{\theta}) & \text{for } \boldsymbol{\theta} \in \mathcal{S}^2, \\ 0 & \text{for } \boldsymbol{\theta} \notin \mathcal{S}^2. \end{cases} \tag{5.30}$$

Both the spherical harmonics as well as the set of partial spherical harmonics form a complete set of orthogonal functions. Hence, any square integrable function on $\mathcal{S}^2$

can be expressed by either set of basis functions,

$$f(\boldsymbol{\theta}) = \boldsymbol{y}^{\mathrm{T}}(\boldsymbol{\theta})\boldsymbol{\phi} = \begin{cases} \breve{\boldsymbol{y}}^{\mathrm{T}}(\boldsymbol{\theta})\breve{\boldsymbol{\phi}} & \text{for } \boldsymbol{\theta} \in \mathcal{S}^2, \\ 0 & \text{for } \boldsymbol{\theta} \notin \mathcal{S}^2, \end{cases} \tag{5.31}$$

where $\boldsymbol{y}(\boldsymbol{\theta})$, $\breve{\boldsymbol{y}}(\boldsymbol{\theta})$ are infinite-dimensional vector functions containing the spherical harmonics or the particular partial spherical harmonics, respectively, cf. eqs. (2.31) and (5.5). Note that the symbol ˘ on top is used here to distinguish the partial spherical harmonics. The corresponding coefficient vectors of infinite length are $\boldsymbol{\phi} = \int_{\mathbb{S}^2} \boldsymbol{y}(\boldsymbol{\theta}) f(\boldsymbol{\theta}) d\boldsymbol{\theta}$ and $\breve{\boldsymbol{\phi}} = \int_{\mathcal{S}^2} \breve{\boldsymbol{y}}(\boldsymbol{\theta}) f(\boldsymbol{\theta}) d\boldsymbol{\theta}$.

Although both infinite series expansions are equivalent in L^2, the equivalence does not hold for the truncated series expansions, which express the respective spatially band-limited source distribution, i.e.

$$f_{\mathrm{N}}(\boldsymbol{\theta}) = \boldsymbol{y}_{\mathrm{N}}^{\mathrm{T}}(\boldsymbol{\theta})\boldsymbol{\phi}_{\mathrm{N}}, \tag{5.32}$$

and

$$\breve{f}_{\breve{\mathrm{N}}}(\boldsymbol{\theta}) = \begin{cases} \breve{\boldsymbol{y}}_{\breve{\mathrm{N}}}^{\mathrm{T}}(\boldsymbol{\theta})\breve{\boldsymbol{\phi}}_{\breve{\mathrm{N}}} & \text{for } \boldsymbol{\theta} \in \mathcal{S}^2, \\ 0 & \text{for } \boldsymbol{\theta} \notin \mathcal{S}^2. \end{cases} \tag{5.33}$$

Modal sound field decomposition using a partial spherical microphone array provides the partial spherical harmonics coefficient vector $\breve{\boldsymbol{\phi}}_{\breve{\mathrm{N}}}$. We denote the conversion to spherical harmonics generically by

$$\hat{\boldsymbol{\phi}}_{\mathrm{N}} = \mathcal{C}(\breve{\boldsymbol{\phi}}_{\breve{\mathrm{N}}}), \tag{5.34}$$

where $\mathcal{C}$ is the conversion operator and $\hat{\boldsymbol{\phi}}_{\mathrm{N}}$ is the achieved estimator for the spherical harmonics coefficient vector $\boldsymbol{\phi}_{\mathrm{N}}$.

5.5.1 Performance measures

As an error-free conversion is not feasible, suitable error measures are required to quantify the conversion performance. For a pragmatic use Ambisonics, is considered as an amplitude panning approach rather than a highly accurate sound-field synthesis, cf. [ZPN12; ZF12]. Therefore it is reasonable to investigate the conversion error in terms of perceivable features.

In the following we will discuss perceptually motivated performance measures

that correspond to mislocalization and direction-dependent loudness as well as source width variations. The spatially discrete equivalents of these measures have proven to be psychoacoustically relevant estimates for the performance of discrete amplitude panning functions, cf. [Fra14].

The *energy* measure,

$$E = \int_{\mathbb{S}^2} |f(\boldsymbol{\theta})|^2 \mathrm{d}\boldsymbol{\theta}, \tag{5.35}$$

is proportional to the perceived loudness of the surrounding source distribution, cf. [Ger92]. The $\boldsymbol{r}_\mathrm{E}$ measure,

$$\boldsymbol{r}_\mathrm{E} = \frac{\int_{\mathbb{S}^2} \boldsymbol{\theta} |f(\boldsymbol{\theta})|^2 \mathrm{d}\boldsymbol{\theta}}{E}, \tag{5.36}$$

is a vector pointing in the perceived direction of the surrounding source distribution, cf. [Ger92], and its length is proportional to the angular spread which, corresponds to the perceived source width, cf. [ZPN12]. Similarly as in [ZPN12], we define the angular mapping error as the directional deviation of $\boldsymbol{r}_\mathrm{E}$ from the actual source direction $\boldsymbol{\theta}_s$,

$$\epsilon_\mathrm{E} = \arccos \frac{\boldsymbol{\theta}_s^\mathrm{T} \boldsymbol{r}_\mathrm{E}}{\|\boldsymbol{r}_\mathrm{E}\|}, \tag{5.37}$$

and the length $\|\boldsymbol{r}_\mathrm{E}\|$ is mapped to an angular spread by

$$\sigma_\mathrm{E} = 2 \arccos(\|\boldsymbol{r}_\mathrm{E}\|). \tag{5.38}$$

The source distribution for single plane wave impinging from direction $\boldsymbol{\theta}_s$ corresponds to a Dirac delta distribution, $f(\boldsymbol{\theta})_\mathrm{N} = \delta(1 - \boldsymbol{\theta}^\mathrm{T} \boldsymbol{\theta}_s)$, and coefficients of its spatially band-limited spherical harmonics expansion yield $\boldsymbol{\phi}_\mathrm{N} = \boldsymbol{y}_\mathrm{N}(\boldsymbol{\theta}_s)$. In this case $f(\boldsymbol{\theta})_\mathrm{N}$ is ideal in terms of the above proposed measures as, cf. [ZF12], $E = \frac{1}{4\pi} \sum_{n=0}^{N} 2n + 1$ and $\boldsymbol{r}_\mathrm{E} = \boldsymbol{\theta}_s \frac{1}{2\pi E} \sum_{n=0}^{N-1} n + 1$. Hence, the energy measure and the spread measure are direction independent and the directional deviation is zero. This reflects the isotropic properties of the spherical harmonics.

max-$\boldsymbol{r}_\mathrm{E}$ weighting. The length of $\boldsymbol{r}_\mathrm{E}$ can be maximized by weighting the components of each order by a suitable factor a_n, cf. [ZF12]. The spherical source distribution with order weighting is $f(\boldsymbol{\theta}) = \boldsymbol{y}_\mathrm{N}^\mathrm{T}(\boldsymbol{\theta}) \, diag\{\boldsymbol{a}_\mathrm{N}\} \boldsymbol{\phi}_\mathrm{N}$, whereby the vector $\boldsymbol{a}_\mathrm{N} = [a_0, \ldots, \overbrace{a_\mathrm{N}, \ldots, a_\mathrm{N}}^{2\mathrm{N}+1}]$ contains the weights.

Computation of $\boldsymbol{r}_{\mathrm{E}}$. To compute the performance measures for an arbitrary spatially band-limited excitation pattern, $\boldsymbol{r}_{\mathrm{E}}$ can be expressed in terms of the coefficient vector $\boldsymbol{\phi}_{\mathrm{N}}$, cf. appendix F,

$$\boldsymbol{r}_{\mathrm{E}} = \frac{\sqrt{4\pi}}{\sqrt{3}\,\boldsymbol{\phi}_{\mathrm{N}}^{\mathrm{H}}\boldsymbol{\phi}_{\mathrm{N}}} \begin{bmatrix} \boldsymbol{\phi}_{\mathrm{N}}^{\mathrm{H}}\,\boldsymbol{G}_{1,1,\mathrm{N}}\,\boldsymbol{\phi}_{\mathrm{N}} \\ -\boldsymbol{\phi}_{\mathrm{N}}^{\mathrm{H}}\,\boldsymbol{G}_{1,-1,\mathrm{N}}\,\boldsymbol{\phi}_{\mathrm{N}} \\ \boldsymbol{\phi}_{\mathrm{N}}^{\mathrm{H}}\,\boldsymbol{G}_{1,0,\mathrm{N}}\,\boldsymbol{\phi}_{\mathrm{N}} \end{bmatrix}, \tag{5.39}$$

whereby the superscript $^{\mathrm{H}}$ denotes Hermitian transpose and

$$\boldsymbol{G}_{nm,\mathrm{N}} = \begin{bmatrix} G_{n,0,0}^{m,0,0}, & \cdots, & G_{n,0,\mathrm{N}}^{m,0,\mathrm{N}} \\ \vdots & \ddots & \vdots \\ G_{n,\mathrm{N},0}^{m,\mathrm{N},0}, & \cdots, & G_{n,\mathrm{N},\mathrm{N}}^{m,\mathrm{N},\mathrm{N}} \end{bmatrix} \tag{5.40}$$

is a matrix containing Gaunt coefficients. The Gaunt coefficient $G_{n,n',n''}^{m,m',m''}$, introduced by Gaunt in [Gau29], is the integral over the product of three spherical harmonics,

$$G_{n,n',n''}^{m,m',m''} := \int_{\mathbb{S}^2} Y_n^m(\boldsymbol{\theta}) Y_{n'}^{m'}(\boldsymbol{\theta}) Y_{n''}^{m''}(\boldsymbol{\theta}) d\boldsymbol{\theta}. \tag{5.41}$$

For more information on the efficient calculation of these integrals see e.g. [Séb98].

5.5.2 Basic linear conversion

Obviously, there is a linear mapping from infinite-dimensional partial spherical harmonics to infinite-dimensional spherical harmonics. Multiplying eq. (5.31) by $\boldsymbol{y}(\boldsymbol{\theta})$ and integrating over $\mathbb{S}^2$ yields, due to the orthogonality of the spherical harmonics,

$$\boldsymbol{\phi} = \boldsymbol{M}\breve{\boldsymbol{\phi}}, \tag{5.42}$$

whereby $\boldsymbol{M}$ is the infinite matrix

$$\boldsymbol{M} = \int_{\mathcal{S}^2} \boldsymbol{y}(\boldsymbol{\theta})\breve{\boldsymbol{y}}^{\mathrm{T}}(\boldsymbol{\theta}) d\boldsymbol{\theta}. \tag{5.43}$$

However, only the spatially band-limited coefficient vector $\breve{\boldsymbol{\phi}}_{\breve{\mathrm{N}}}$ is provided by a practical partial spherical array, and we are interested in an spatially band-limited spherical harmonics series, only. Thus eq. (5.42) is truncated accordingly, yielding

$$\hat{\boldsymbol{\phi}}_{\mathrm{N}} = \boldsymbol{M}_{\mathrm{N},\breve{\mathrm{N}}}\breve{\boldsymbol{\phi}}_{\breve{\mathrm{N}}}, \tag{5.44}$$

where

$$M_{\mathrm{N},\breve{\mathrm{N}}} = \int_{\mathcal{S}^2} \boldsymbol{y}_{\mathrm{N}}(\boldsymbol{\theta}) \breve{\boldsymbol{y}}_{\breve{\mathrm{N}}}^{\mathrm{T}}(\boldsymbol{\theta}) d\boldsymbol{\theta}. \tag{5.45}$$

Hence in this case the generic conversion operator $\mathcal{C}$ in eq. (5.34) is replaced by a matrix multiplication.

Interestingly, this basic linear conversion can be also viewed as approximating $\breve{f}_{\breve{\mathrm{N}}}(\boldsymbol{\theta})$ by $\hat{f}_{\mathrm{N}}(\boldsymbol{\theta})$ in a least-squares-error sense, as eq. (5.44) is as well the solution of the optimization problem,

$$\min \int_{\mathbb{S}^2} |\breve{f}_{\breve{\mathrm{N}}}(\boldsymbol{\theta}) - \hat{f}_{\mathrm{N}}(\boldsymbol{\theta})|^2 d\boldsymbol{\theta}. \tag{5.46}$$

The value of $\breve{\mathrm{N}}$ is given for a particular partial spherical array and a certain frequency, but we have not specified the value of N, yet. For $\mathrm{N} \to \infty$ it follows from eq. (5.46) that in this case we have $\hat{f}(\boldsymbol{\theta}) = \breve{f}_{\breve{\mathrm{N}}}(\boldsymbol{\theta})$. However, the aim of the conversion is to achieve a spherical harmonics expansion of finite order. Thus the value of N shall be close to $\breve{\mathrm{N}}$, and the pragmatic choice is the nearest integer, i.e. $\mathrm{N} = [\breve{\mathrm{N}}]$.
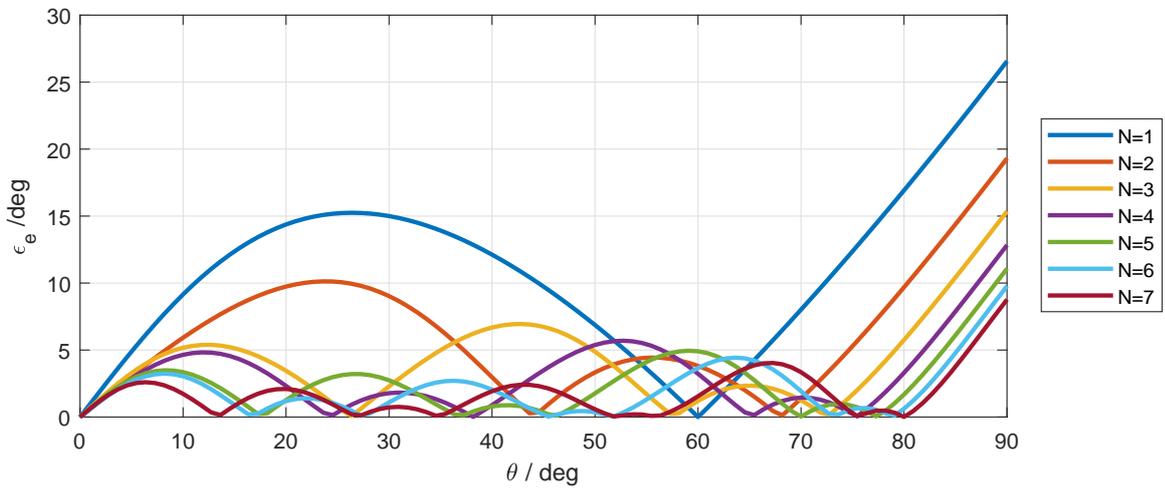
Conversion performance. The conversion performance of the basic linear conversion is exemplarily shown for a hemispherical array and an array on a symmetrical spherical zone with $\theta_1 = 30°$, $\theta_2 = 120°$, for different maximum orders N. Thereby the arrays are assumed to be ideal, i.e. capturing the respective partial spherical harmonics up to the maximum order $\breve{\mathrm{N}}$ without any error. The spatially band-limited partial spherical harmonic coefficients of a plane wave impinging from direction $\boldsymbol{\theta}$ are converted to spherical harmonics according to eq. (5.44), and the performance measures for $\hat{\boldsymbol{\phi}}_{\mathrm{N}}$ are shown in figs. 5.6 and 5.8. Figures 5.7 and 5.9 show the performance measures with max-$\boldsymbol{r}_{\mathrm{E}}$ weighting, applied after the conversion.

Note that the results are shown in dependence of the zenith angle of the incident plane wave, only, as these representation are invariant under azimuthal rotation. Furthermore, due to the symmetry of the spherical segment harmonics, the results in figs. 5.8 and 5.9 are only shown for the upper half, i.e. $\theta = 60° \ldots 90°$, and the x-axis is reversed such that the location of the rigid boundary in the diagrams is on the right side, as in figs. 5.6 and 5.7. The dashed lines in all subfigures (c) are shown for comparison and represent the direction-invariant spread, obtained for the ideal spatially band-limited spherical harmonics expansion, with or without max-$\boldsymbol{r}_{\mathrm{E}}$ weights, respectively.

The energy measure and the spread measure of the converted partial spherical harmonics representations are direction dependent, which is clearly visible for both
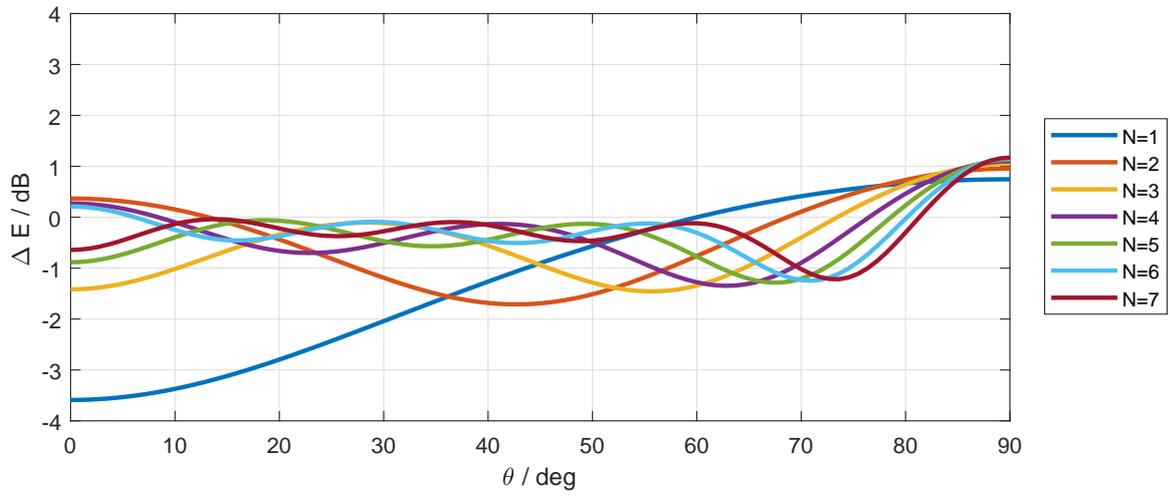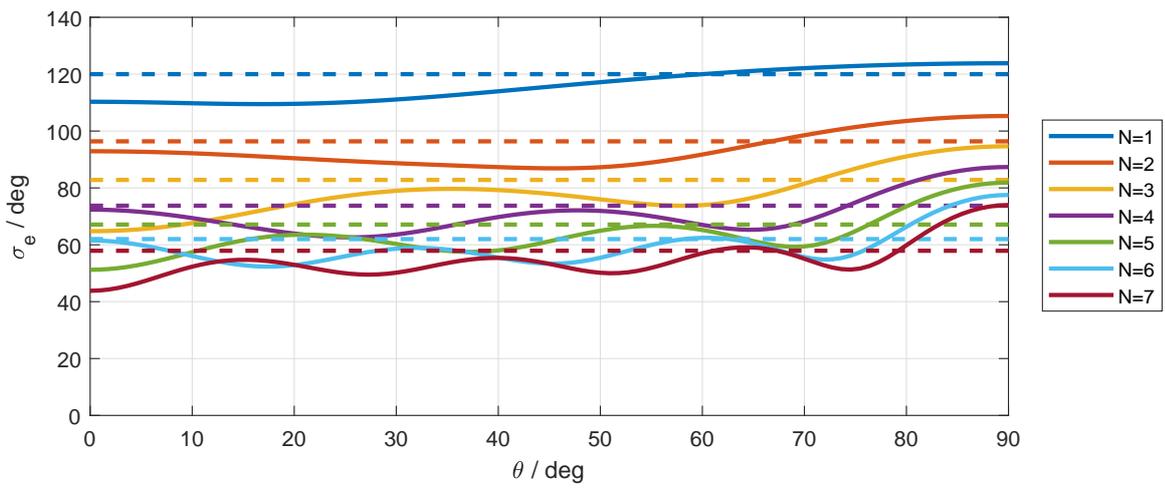
Figure 5.6: Performance measures of a hemispherical array for the basic linear conversion of a plane wave, in dependence of the incident zenith angle, for different maximum orders N.
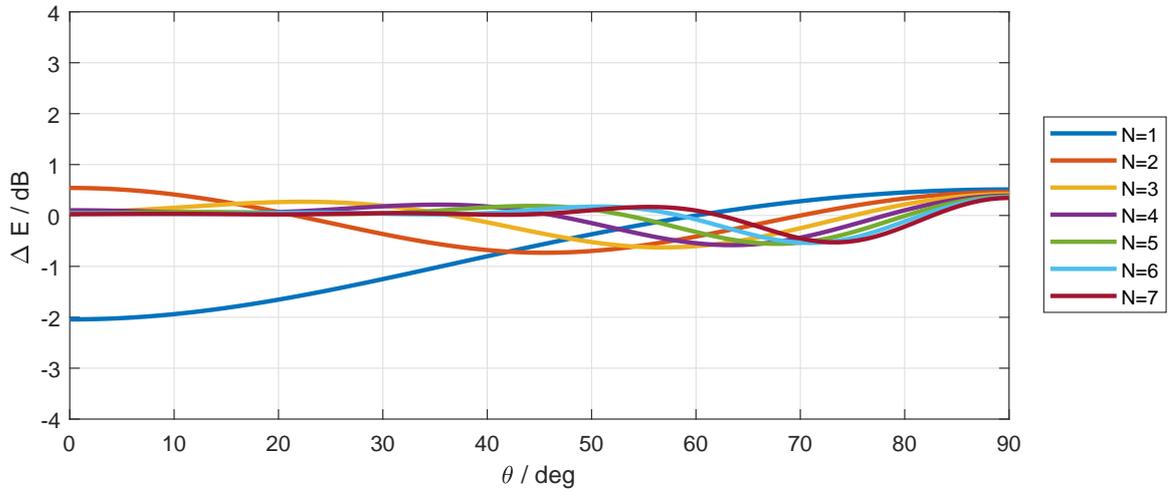
(a)
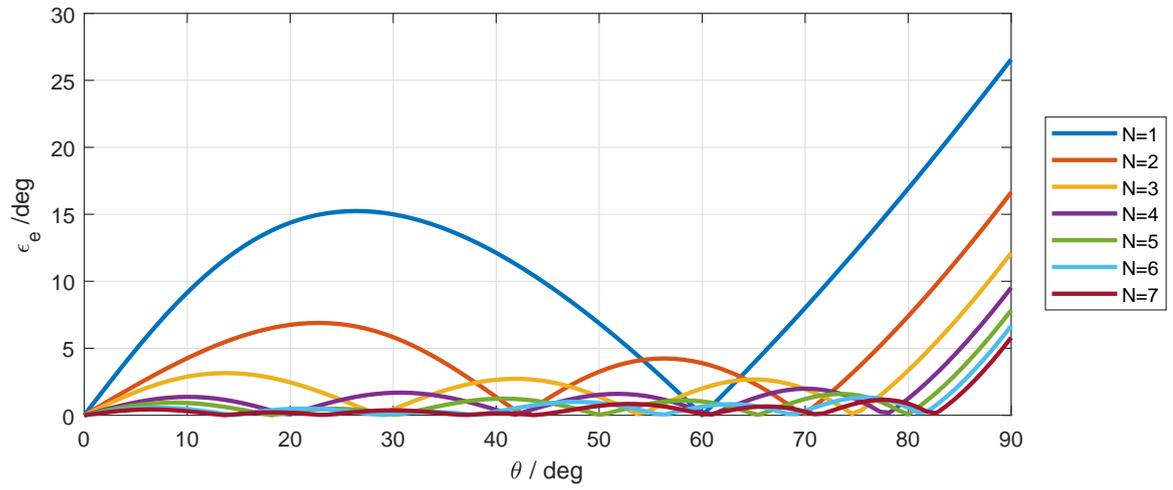
(b)
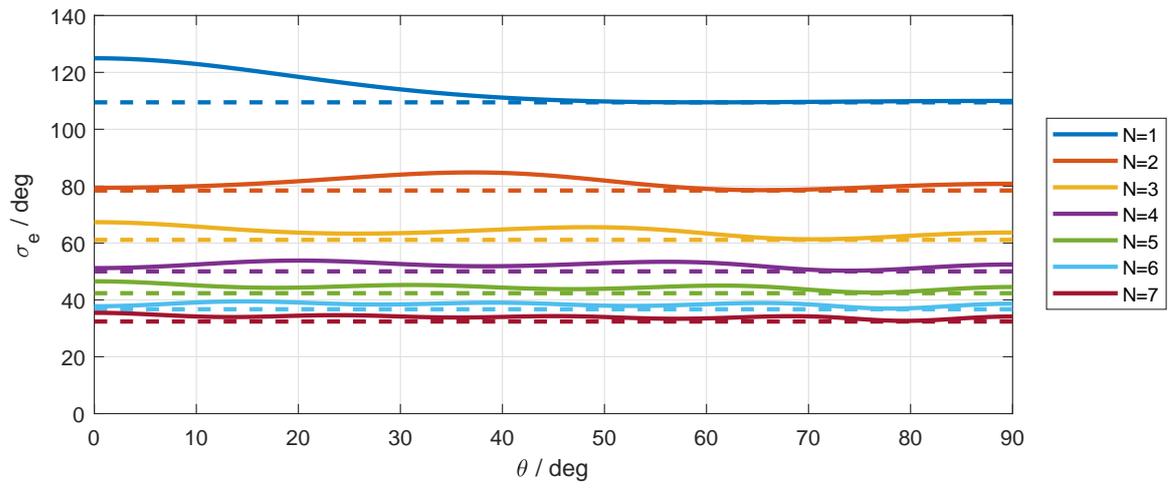
(c)

Figure 5.7: Performance measures of a hemispherical array for the basic linear conversion of a plane wave, with max-$\boldsymbol{r}_\mathrm{E}$ weighting, in dependence of the incident zenith angle, for different maximum orders N.

Figure 5.8: Performance measures of a spherical zone array for the basic linear conversion of a plane wave, in dependence of the incident zenith angle, for different maximum orders N.

Figure 5.9: Performance measures of a spherical zone array for the basic linear conversion of a plane wave, with max-r_E weighting, in dependence of its incident zenith angle, for different maximum orders N.

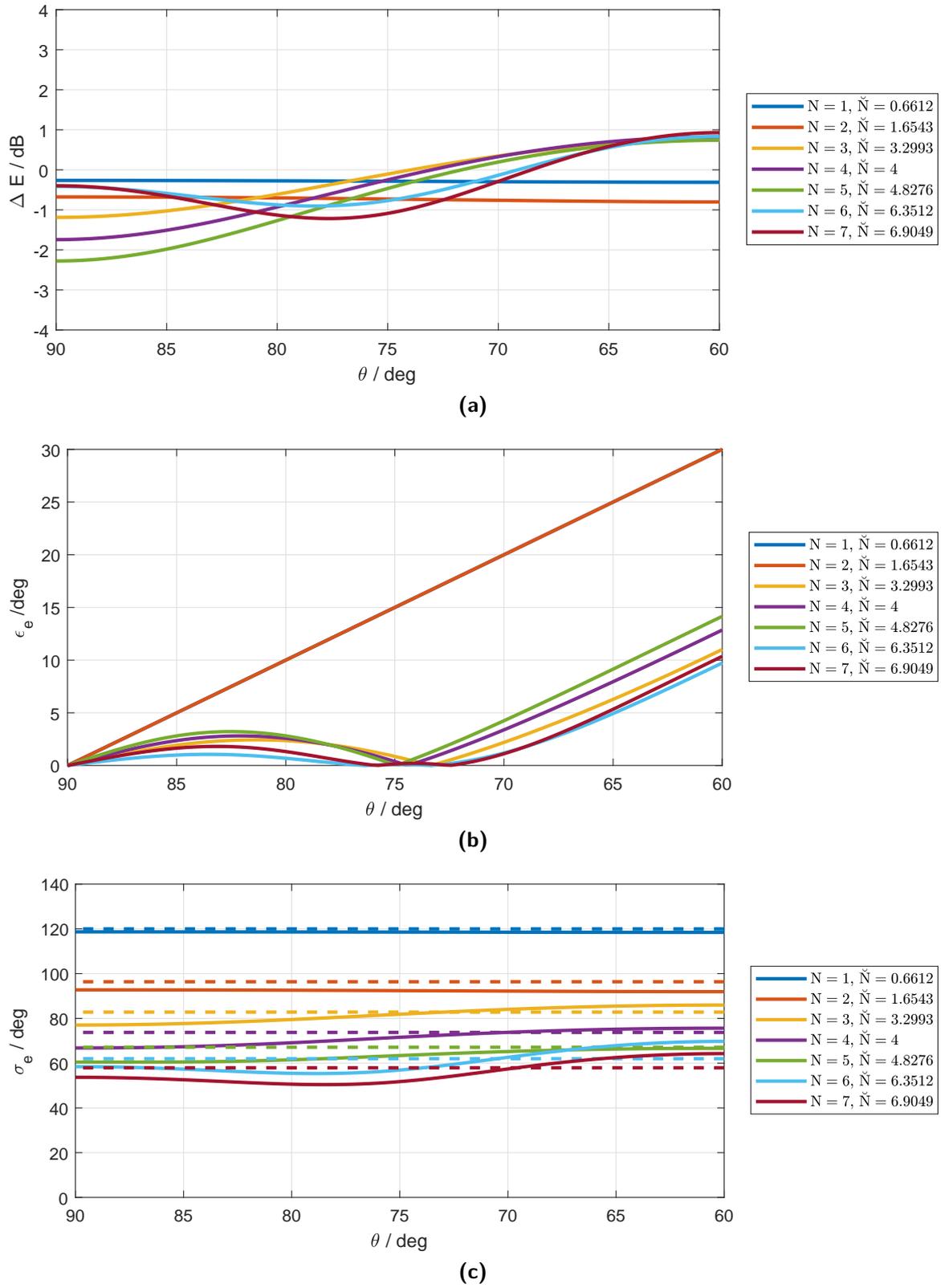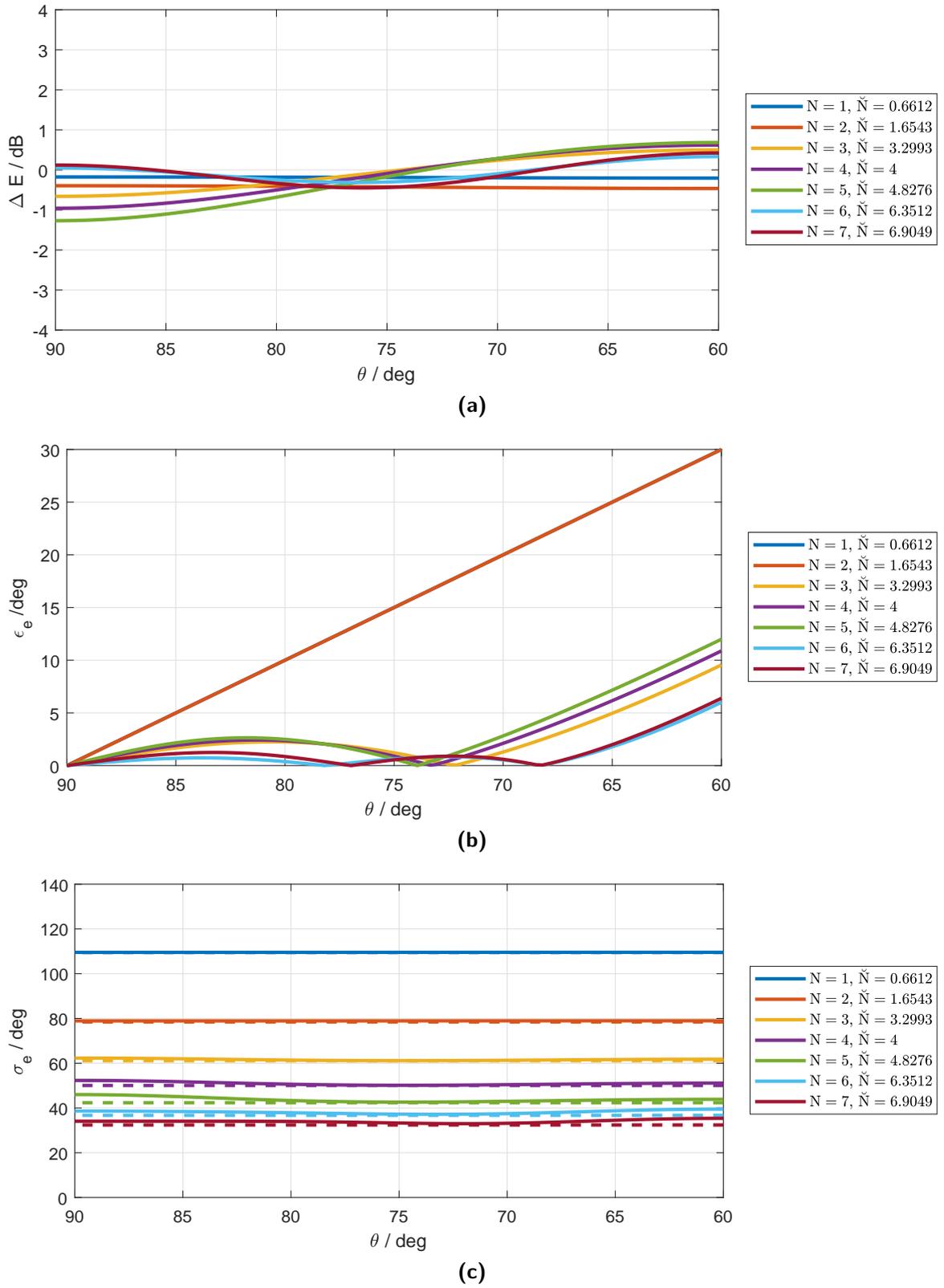examples. Furthermore, the angular mapping error oscillates in θ, whereby it is zero in the middle, i.e. at $\theta = 0°$ for the hemisphere, and $\theta = 90°$ for the spherical zone. The largest mapping errors occur at the the boundaries. Generally, the mapping errors decrease with increasing order. Interestingly, max-$\boldsymbol{r}_\mathrm{E}$ weighting reduces not only the spread measure of the conversion results, but also improves the energy measure and reduces the mapping errors for both examples.

The mapping errors for $\mathrm{N} = 1, 2$ in figs. 5.8b and 5.9b linearly increase towards the boundary, i.e. the conversion maps always to $\theta = 90°$ independent of the true source direction. This results from the fact that for $\mathrm{N} = 1, 2$ the order-limited spherical segment harmonics representation contains only one component for each degree m, which points to $\theta = 90°$.

The results of the basic linear conversion indicate that there will be perceivable artifacts when reproducing sound scenes captured with partial spherical arrays, especially for low orders. This is an issue even for partial spherical arrays which are capable to capture high-oder components, due to the frequency dependent spatial band-limitation, which results from the regularization of the radial filters. For hemispherical arrays better conversion results can be achieved by a non-linear conversion, which takes the energy distribution of a plane wave over the spherical harmonic components into account [PZ17]. These promising results suggest that better conversion results might be achieved for general partial spherical harmonics representations by similar elaborate non-linear conversions.

5.6 Design and evaluation of a prototype array on a symmetrical spherical zone

This section is largely based on [PP14]. The practical applicability of modal sound field decomposition using partial spherical arrays is demonstrated in the following by means of modal beamforming based on acoustical measurements of a prototype array.

5.6.1 Prototype design

The prototype shown in fig. 5.10 was designed to cover a symmetrical spherical zone $\mathcal{S}^2 = \{\boldsymbol{\theta} : 60° \leq \theta \leq 120°\}$, such that the surface of this spherical zone is half of the surface of the full sphere.

Most of the following design parameters, such as the number of microphones and most of the geometrical dimensions result from constructional and availability issues.

Figure 5.10: Finished prototype: the large picture depicts the array mounted on a stand. The smaller pictures show some construction details.

The array has been assembled with 64 digital microphones, which are commercially available [Vis17]. Hence, the sound pressure distribution at the spherical zone is angularly sampled at 64 points, which allows a decomposition into a number of Q = 64 spherical segment harmonics, cf. eq. (5.12). The truncation of the infinite set of basis functions to Q components is illustrated in fig. 5.11. As Q = 64 is predetermined by the microphone hardware, the maximum order results in N $\approx 9.9 \geq \nu_q$. The first 29 spherical segment harmonics of this truncated set, for which $\nu_q \leq 6$, correspond to those depicted in fig. 4.3. The distribution of the microphones on the spherical segment was optimized by minimizing the condition number of the matrix, containing the sampled spherical segment harmonics, based on a fixed grid and considering some constructional restrictions. The optimization was conducted as described in section 5.2. Figure 5.3 illustrates the progress of the optimization, whereby the bottom row corresponds to the final sampling positions, which achieve a condition number $\kappa(\boldsymbol{Y}_\mathrm{N}) \approx 2.3$. This is sufficiently small for a robust modal decomposition. Further details can be found in [Pau13], where also table of sampling positions is provided in the appendix.

For the radius of the rigid spherical zone a value of $r_m = 0.1\,\mathrm{m}$ was chosen, which corresponds to the minimal possible size such that the microphone units just fit in, cf. [Pau13]. Therewith, the upper frequency limit of the array can be estimated using eq. (5.17) by $f_u \approx 5.4\,\mathrm{kHz}$, with $c = 343\,\mathrm{m/s}$. For the lower frequency limit, also the maximum gain of the radial filters has to be considered, cf. section 5.1. A maximum
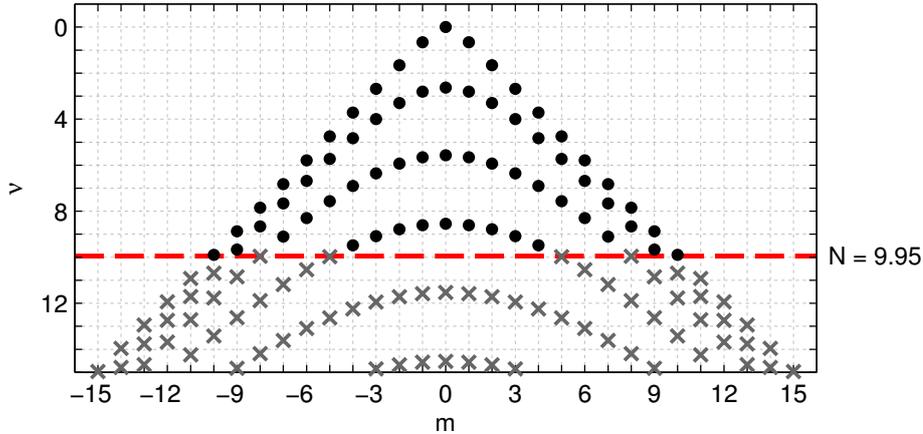
Figure 5.11: Parameter combinations ν_q and m_q of the spherical segment harmonics fulfilling a to the double conical boundary condition according to the geometry of the prototype. The black dots indicate the 64 modal components, for which $\nu_q < N$, the gray crosses indicate higher order components and the red dashed line indicates the truncation boarder $N = 9.95$.

gain of 30 dB was chosen, to leave enough headroom for the signal dynamic in a practical application. For the given value of $N \approx 9.9$, the necessary gain for the radial filters is less than 30 dB down a value of $kr_m \approx 7.8$, cf. fig. 5.1. This yields a lower frequency limit of $f_l \approx 4.3\,\text{kHz}$. The radial filters were implemented as FIR filters as in the design example given section 5.3, and the frequency responses of the gain-limited radial filters for the first 29 modal components, with $\nu_q < 6$, are shown in fig. 5.5.

The radial extent of the conical boundaries was chosen to be 0.4 m. This choice was a compromise between a compact, transportable prototype and a sufficient acoustic attenuation of sources from directions $\boldsymbol{\theta} \notin \mathcal{S}^2$ at lower frequencies.

Hardware Implementation. The digital microphone hardware [Vis17] consist of 64 microphone units and an integration board. Each microphone unit contains an electret capsule, a pre-amplifier and an analog-to-digital converter at a sampling rate of 44.1 kHz. The microphone units are daisy-chained and connected to the integration board, which transmits the microphone signals to a computer via USB. A local carpenter built the cabinet of the prototype using a *computerized numeric control* (CNC) machine. The two rigid cones where made of *medium density fiber* (MDF) and the spherical zone was manufactured from polyurethane plastic plates. Finally, the individual components were glued together and finished in black, cf. fig. 5.10. Further constructional details are given in [Pau13].

5.6.2 Evaluation

The feasibility of modal sound field decomposition with the prototype hardware is investigated based on a beamforming application. Therefore, the spatial impulse responses of the built microphone array were measured. Applying this measurement data, the beamformer responses for different steering directions are analyzed.

Acoustic measurements. In the measurements we determined the transfer functions to the array microphones from 576 position distributed on a centered, surrounding spherical surface with a radius of $r_s = 1.4\,\mathrm{m}$. This was achieved using 16 loudspeakers arranged on a vertical semicircle. The loudspeakers were displaced in equal steps of $\Delta\theta = 11.25°$, as shown in fig. 5.12. Furthermore, the array was positioned on an electronically controlled turntable. The turntable rotated the array in 36 equidistant azimuthal steps of $\Delta\phi = 10°$. In doing so, the 576 positions were measured sequentially. The impulse responses of the transfer functions were measured using exponentially swept sines [Far00], with a sweep length of 1.5 s. After the deconvolution, the impulse responses were truncated to a length of 122 samples, which corresponds to a distance of about 0.96 m at the used sampling frequency of 44.1 kHz. This is sufficiently short to largely exclude possible reflections, due to e.g. the floor of the room, but sufficiently long to preserve the acoustic influence of the rigid cones.

Results. The beamforming performance is investigated in terms of directivity patterns. As described in section 5.1, the measured transfer functions are decomposed into spherical segment harmonics applying eq. (5.12), and using regularized FIR radial filters, cf. fig. 5.5. Then the beamforming according to eq. (5.25) is applied using the weights given in eq. (5.29). This yields directivity patterns for arbitrary steering directions $\boldsymbol{\theta}_b \in \mathcal{S}^2$. To achieve a smooth directivity pattern from the spatially discretized measurement data, these are interpolated using spherical harmonics of order 15.

As expected, the investigated patterns showed that the frequency-dependent directivity of the beamformer is rotationally symmetric with ϕ and mirror symmetric around the equatorial plane. Of course, this symmetry is not perfect, but only slight deviations are noticeable, which mainly affect only the side lobes. Therefore, it is sufficient to show directivity plots for steering directions $\boldsymbol{\theta}_b$ for a fixed azimuth and different zenith angles, ranging from $60° \leq \theta_b \leq 90°$. All other steering directions can be deduced by the geometrical symmetries.

Figure 5.13 shows the directivity and on-axis magnitude response of the beamformer
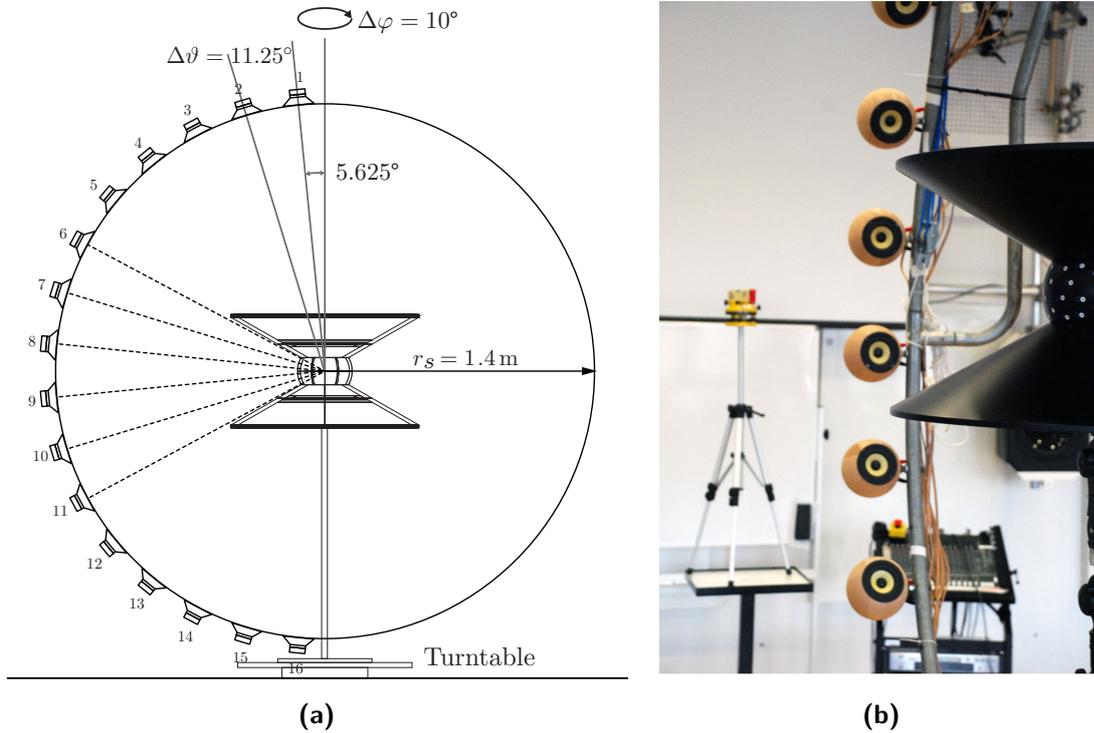
Figure 5.12: Setup for spatial impulse response measurement.

for different steering directions. The decrease of magnitude towards lower frequencies in fig. 5.13c obviously results from the limited maximum gain of the regularized radial filters. Note that the magnitude responses in figs. 5.13f, 5.13i and 5.13l are plotted relative to the on-axis response for $\theta_b = 90°$, cf. fig. 5.13c.

At 5 kHz the beam pattern is well shaped and the main lobe is nearly rotational symmetric when pointing in the horizontal plane, i.e. $\boldsymbol{\theta}_b = 90°$. When the beam is steered towards the conical boundaries, the main lobe is deformed, and the direction of maximum sensitivity does not coincide with the intended beam direction, but is rather shifted away from the boundary. The deformation of the main lobe and shift of the maximum gets more and more pronounced as the steering direction approaches the boundary. This behavior agrees with the results for angular mapping error when converting spherical segment harmonics to spherical harmonics, cf. fig. 5.8b.

The widening of the beam pattern for lower frequencies results from the limited gain of the radial filters as higher order components are not sufficiently amplified. Thus with decreasing frequency the maximum order of the effectively contributing modal components decreases, which reduces the spatial resolution, i.e. the beam pattern gets wider. Interestingly, the beam widening is different for the horizontal and vertical beam width. Each modal component contains some amount of horizontal

(a) $\theta_b = 90°$, horizontal cut   **(b)** $\theta_b = 90°$, vertical cut   **(c)** $\theta_b = 90°$, on-axis response $H_{90}(f)$

(d) $\theta_b = 80°$, horizontal cut   **(e)** $\theta_b = 80°$, vertical cut   **(f)** $\theta_b = 80°$, on-axis response $H_{80}(f)$ relative to $H_{90}(f)$

(g) $\theta_b = 70°$, horizontal cut   **(h)** $\theta_b = 70°$, vertical cut   **(i)** $\theta_b = 70°$, on-axis response $H_{70}(f)$ relative to $H_{90}(f)$

(j) $\theta_b = 60°$, horizontal cut   **(k)** $\theta_b = 60°$, vertical cut   **(l)** $\theta_b = 60°$, on-axis response $H_{60}(f)$ relative to $H_{90}(f)$
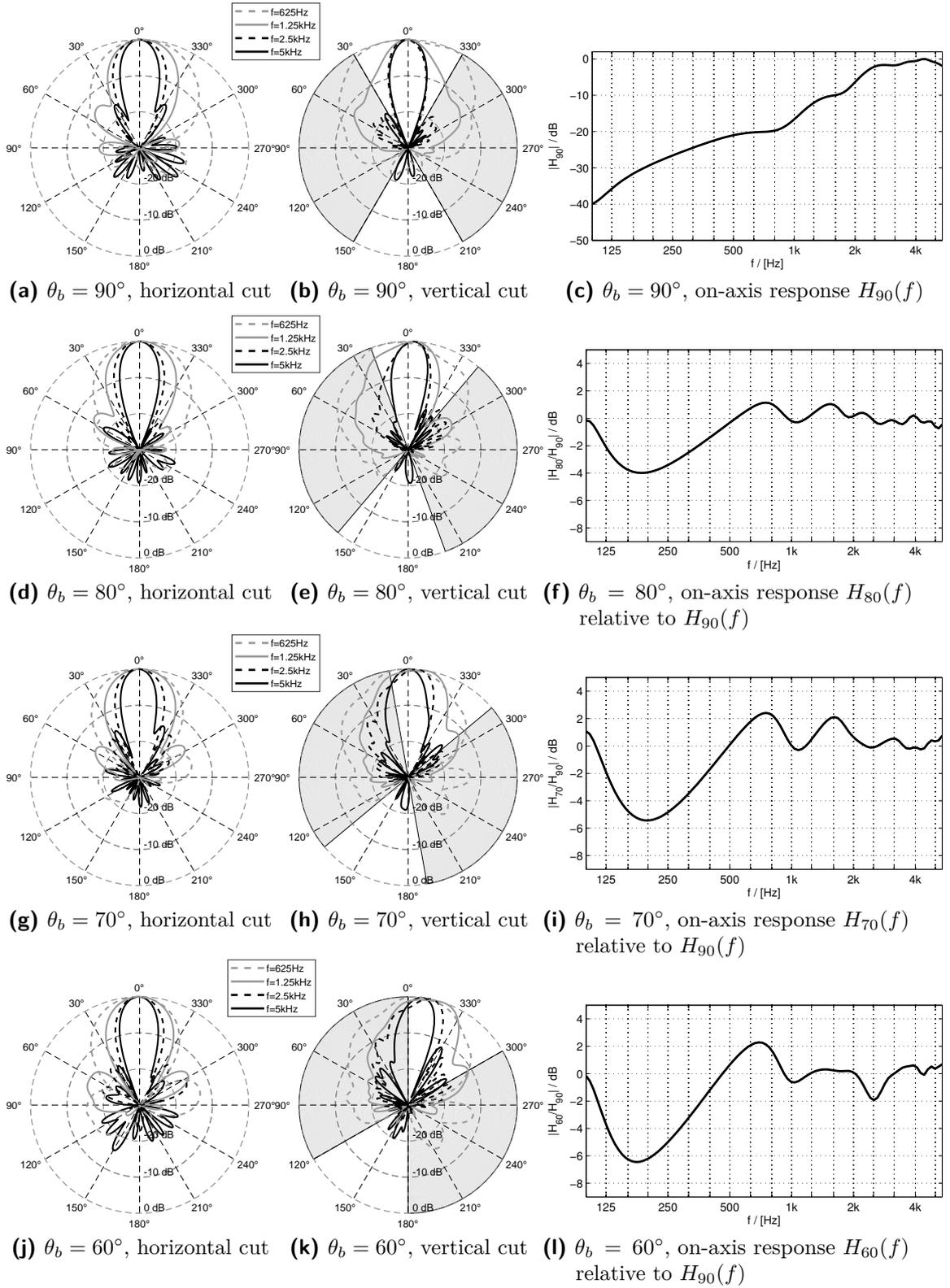
Figure 5.13: Directivity pattern and on-axis response of the beamformer for different steering directions in θ; the polar plots (a), (d), (g), (j) show the horizontal cut and (b), (e), (h), (k) show the vertical cut of the directivity pattern relative to the steering direction, which coincides with the $0°$ direction of each plot. The light gray area indicates the range of the zenith angle covered by the rigid cones. The diagram (c) depicts the on-axis magnitude responses for $\theta_b = 90°$ and the diagrams (f), (i), (l) depict the on-axis magnitude responses for $\theta_b = 80°, 70°, 60°$, relative the response for $\theta_b = 90°$.

99

and/or vertical information. Due to the limited filter gain the higher order modal components die out bit by bit towards lower frequencies, and also the amount of spatial information is reduced bit by bit. If e.g. only the lowest 5 modal components with $\nu_q < 2$ contribute, cf. fig. 5.11, it shows that these functions contain only horizontal and no vertical information, as all of them are nearly constant in θ, see the top row in fig. 4.3. Thus also beam pattern would be nearly constant in the vertical direction within the boundaries, independent of the steering direction, whereas in the horizontal direction still a steering of the beam is possible.

The ripples in the relative on-axis responses above 500 Hz probably originate also from the non-isotropic behavior of the spherical segment harmonics. These ripples are roughly in the same range as the ripples in the energy measure when converting spherical segment harmonics to spherical harmonics, cf. fig. 5.8a. The larger notch at about 180 Hz may be caused by the finite length of the rigid cones.

The evaluation of the realized prototype showed that the beamforming algorithm yields reasonable beam patterns, although an infinitely long double-cone is assumed in the calculation of the beamformer weights. The beamforming approach relies on a proper modal sound field decomposition. Thus the beamforming results imply that modal sound field decomposition is feasible, and sound scenes recorded by the prototype array can be rendered on a surrounding loudspeaker array using a suitable conversion of the spherical segment harmonics to conventional spherical harmonics, cf. section 5.5.

Chapter 6

Conclusion

The main contribution of this work is the generalization of the concept of spherical arrays to arrays on partial spherical surfaces. Similar to spherical arrays, this generalization is based on the solutions of the Helmholtz equation is spherical coordinates, but additional angular boundary conditions are imposed. These boundary conditions enclose the partial spherical surface, respectively restrict the angular range.

To provide a sound foundation of spherical microphone arrays, chapter 2 presented the underlying acoustic theory and a brief review of beamforming, as well as capture and reproduction of spatial sound scenes, using spherical arrays.

In chapter 3, the individual solutions of the angle dependent differential equations, arising from the separation of the Helmholtz equation, have been investigated for various types of boundary conditions. We showed that under these boundary conditions the set of solutions always forms a complete orthogonal basis on the interval between the points where the boundary conditions are imposed. This holds for both, the azimuth and the zenith angle dependent differential equation. The eigenvalues of the respective differential operator are determined by type and location of the boundary conditions. These eigenvalues coincide with the separation constants of the Helmholtz equation, and are usually denoted in terms of the parameters degree and order. For the considered boundary conditions, we showed that these eigenvalues are real-valued, positive, and form a discrete set. The free-field solutions fit in this framework as a set of particular angular boundary conditions, although there are no tangible boundary surfaces in this case. The azimuthal solution is required to be periodic, whereas the solution in the zenith angle has to obey singular boundary conditions, which leads to integer-valued eigenvalues.

Combining the angular solutions for a specific boundary condition in the azimuth and zenith angle yields a complete set of orthogonal functions on the partial spherical

surface enclosed by the boundaries. In chapter 4 we explored the combination possibilities, which yields different partial spherical surfaces such as spherical caps, zones, lunes and quadrangles. A uniform notation of the partial spherical harmonics according to these combinations of boundary conditions was introduced, which allows for a generalized representation of sound fields in source free regions enclosed by angular boundaries, the according Green's function, and the expression for plane waves. This uniform notation also includes conventional spherical harmonics.

The theoretical results clearly show that the solutions under angular boundary conditions exhibit the same structure as the free-field solution. Therefrom, the idea of partial spherical microphone arrays with rigid angular boundary conditions suggest itself, which has been investigated in chapter 5. The properties of the radial solutions, which are similar for integer and non-integer order, confirm that the pressure distribution on a partial spherical surface due to a plane wave is well approximated by truncating the infinite partial spherical harmonics expansion. However, in contrast to spherical harmonics, the truncated partial spherical harmonics series has a non-isotropic point spread function, i.e. the truncated expansion of a Dirac delta distribution does not have a uniform shape in all orientations. This is obviously a consequence of the angular boundaries. The non-isotropy decreases when more functions in the truncated expansion are used, and isotropy is only achieved by the infinite series representation, i.e. the point spread function is a Dirac delta distribution.

Beyond all similarities, there are new challenges in the implementation of partial spherical microphone arrays. Section 5.2 presents a synopsis of new strategies for sampling points on partial spherical surfaces, which have been developed in master projects related to this dissertation. Suitable distributions are achieved for minimizing the condition number of the decomposition matrix by moving the sampling points sequentially on a dense, equally spaced grid. For non-integer orders, the implementation of the radial filters is similar as for the integer order case, and requires a limitation of the maximum filter gain. An recursive discrete-time implementation is not feasible, but a finite impulse response realization of suitable length is appropriate.

Maximum-directivity beamforming based on modal sound field decomposition is achieved similar as for spherical arrays. The angle-dependent beam shape results from the non-isotropy of the spatially band-limited partial spherical harmonics and is evident for the above stated reasons.

Ambisonics related approaches for the reproduction of sound scenes with surrounding spherical loudspeaker arrays require a source distribution represented in spherical harmonics. Therefore the spatially band-limited source distribution captured by a

partial spherical microphone arrays need to be converted into a spherical harmonics. The band-limited spherical harmonics representation of the true source distribution is not achievable by a linear mapping. Like physically perfect sound field reproduction by a surrounding loudspeaker distribution, such a perfect conversion is an overambitious aim, and it is more reasonable to aspire the preservation of perceivable features. This motivates perceptual measures of the conversion error in terms of loudness, mislocalization and source width, which have been presented in section 5.5. By means of this measures, the proposed basic linear conversion has been evaluated.

Finally, we have shown the design and implementation of a microphone array located on a rigid spherical zone bounded by a symmetrical, rigid double-cone. The beamforming performance of a prototype array was investigated by directivity measurements.

The open problems identified during the course of this thesis lead to the following recommendations for future work:

Advanced conversion to spherical harmonics.   The results of the basic linear conversion examined in section 5.5, indicate perceivable artifacts when reproducing sound scenes captured with partial spherical arrays, especially for low order representations. As shown in [PZ17] for hemispherical arrays, better results can be achieved by a non-linear conversion approach, which takes into account the energy distribution of a plane wave over the spherical harmonic components. The underlying principle is not directly applicable for other partial spherical harmonics representations. The transfer of this advanced hemispherical conversion to general partial spherical harmonics and the development of similarly elaborated non-linear conversions is an ongoing research question.

Investigations on the effect of finite-length boundary conditions.   The theoretical considerations are made for infinitely long rigid boundaries, which is clearly not the case for any practical implementation. In the current work, we tacitly assumed that a sufficient length of the boundary surfaces resembles infinity. Similar as in [Mec09], finite length boundary conditions can be modeled by splitting $\mathbb{R}^3$ into a spherical interior region with a radius according to length of the boundaries, and an exterior region. The field within the exterior region is expressed by the free-field solutions and the field within the interior region by the respective partial spherical solutions. The coupling of the modal components is achieved by demanding equality

of the sound pressure and its radial derivate at the joint partial spherical surface. However, the pressure distribution on a large, rigid, circular plane due to a plane wave shows fluctuations associated with Fresnel-zone interference patterns, cf. [JT65], also in the center of the plane. Likewise, the pressure distribution on a large, rigid cone, shows similar fluctuations. These Fresnel-zone fluctuations are not considered in the modal sound field decomposition approach, and the investigation of the impact of these effects remains an open question.

Appendix A

Green's function for the Helmholtz equation

Here we derive Green's function for the Helmholtz equation in spherical coordinates. Therefore we first derive Green's function of ordinary second order differential equations and then trace back the problem of determining Green's function for the Helmholtz equation to such a problem by dimensional reduction.

Green's function of ordinary second order differential equations. *Green's function* $G(x, \xi)$ is the solution of the following inhomogeneous linear second order differential equation $x \in (\mathrm{x}_1, \mathrm{x}_2)$ under prescribed homogeneous boundary conditions at the endpoints of the interval

$$\mathcal{L}G(x, \xi) = -\delta(x - \xi) \tag{A.1}$$

where $\mathcal{L} := \frac{d}{dx}\left(p(x)\frac{d}{dx}\right) - q(x)$ is a formal self-adjoint linear differential operator with p, p' and q being continuous functions and $p > 0$ on the interval $(\mathrm{x}_1, \mathrm{x}_2)$. Green's function fulfills the following conditions, [CH24, p. 275]

1. For a fixed value of ξ, $G(x, \xi)$ is a continuous function of x in $(\mathrm{x}_1, \mathrm{x}_2)$ and fulfills the prescribed boundary conditions at x_1 and x_2.

2. Except for $x = \xi$, the first and second derivative of G with respect to x are continuous everywhere in $(\mathrm{x}_1, \mathrm{x}_2)$. At $x = \xi$, the first derivative has a jump discontinuity given by

$$\left.\frac{dG(x, \xi)}{dx}\right|_{x=\xi-0}^{x=\xi+0} = -\frac{1}{p(x)} \tag{A.2}$$

3. G fulfills the homogeneous differential equation $\mathcal{L}G(x, \xi) = 0$ everywhere in (x_1, x_2) except for $x = \xi$.

Most of these properties of Green's function are evident from the differential equation and the boundary conditions. The fact that $G(x, \xi)$ is continuous and its first derivative shows a jump discontinuity at $x = \xi$ can be shown as follows, see [CH24, p. 273]. Integrating eq. (A.1) in the limits of $\xi - \epsilon$ and $\xi + \epsilon$, $\epsilon > 0$ yields

$$\int_{\xi-\epsilon}^{\xi+\epsilon} \left(p(x) \frac{d^2 G(x, \xi)}{dx^2} + p'(x) \frac{dG(x, \xi)}{dx} - q(x) G(x, \xi) \right) dx = -1, \qquad \text{(A.3)}$$

and applying integration by parts we get

$$\left[p(x) \frac{dG(x, \xi)}{dx} \right]\Big|_{x=\xi-\epsilon}^{|x=\xi+\epsilon} - \int_{\xi-\epsilon}^{\xi+\epsilon} q(x) G(x, \xi) dx = -1. \qquad \text{(A.4)}$$

Obviously, if $G(x, \xi)$ is a solution eq. (A.1), the above equation holds also for the limit of $\epsilon \to 0$. Hence, $G(x, \xi)$ has to be continuous at $x = \xi$ as otherwise the limit of $\left[p(x) \frac{dG(x, \xi)}{dx} \right]\Big|_{x=\xi-\epsilon}^{|x=\xi+\epsilon}$ for $\epsilon \to 0$ does not exist. From the continuity of $G(x, \xi)$ follows that $\lim_{\epsilon \to 0} \int_{\xi-\epsilon}^{\xi+\epsilon} q(x) G(x, \xi) dx = 0$. Furthermore follows from the limit of eq. (A.4) that derivative of $G(x, \xi)$ has to have a jump discontinuity at $x = \xi$ determined by the following relation:

$$\lim_{\epsilon \to 0} \frac{dG(x, \xi)}{dx}\Big|_{x=\xi-\epsilon}^{|x=\xi+\epsilon} = -\frac{1}{p(\xi)}. \qquad \text{(A.5)}$$

Construction of Green's function. Consider two solutions $y_1(x)$, $y_2(x)$ of the homogeneous differential equation $\mathcal{L}y(x) = 0$, where $y_1(x)$ fulfills the prescribed boundary condition at $x = x_1$ and $y_2(x)$ fulfills the prescribed boundary condition at $x = x_2$. $G(x, \xi)$ can be expressed in the following form, as it fulfills the homogeneous equation almost everywhere except for $x = \xi$,

$$G(x, \xi) = \begin{cases} c_1 \, y_1(x) & \text{for } x \leq \xi, \\ c_2 \, y_2(x) & \text{for } x \geq \xi. \end{cases} \qquad \text{(A.6)}$$

Due to the continuity of $G(x, \xi)$ and the jump discontinuity of its first derivative according to eq. (A.2), we have

$$c_1 \, y_1(\xi) = c_2 \, y_2(\xi),$$
$$c_1 \, y_1'(\xi) - c_2 \, y_2'(\xi) = -\frac{1}{p(\xi)}. \tag{A.7}$$

Solving for c_1, c_2 yields

$$c_1 = \frac{-y_2(\xi)}{p(\xi) \, [y_1(\xi) y_2'(\xi) - y_1'(\xi) y_2(\xi)]},$$
$$c_2 = \frac{-y_a(\xi)}{p(\xi) [y_1(\xi) y_2'(\xi) - y_1'(\xi) y_2(\xi)]}. \tag{A.8}$$

Inserting this in eq. (A.6) we get

$$G(x, \xi) = \frac{-1}{p(\xi) \, [y_1(\xi) y_2'(\xi) - y_1'(\xi) y_2(\xi)]} \begin{cases} y_2(\xi) \, y_1(x) & \text{for } x \leq \xi, \\ y_1(\xi) \, y_2(x) & \text{for } x \geq \xi. \end{cases} \tag{A.9}$$

Note that Green's function only exists if $y_1(x)$ and $y_2(x)$ are linearly independent solutions. Evidently, for solutions, i.e.. $y_1(x) = c y_2(x)$, eq. (A.7) is contradicting since if $G(x, \xi)$ is continuous at ξ its first derivative can not have a jump discontinuity and vice versa. However, one can define in this case a *Green's function in the generalized sense*, see [CH24, p. 280].

Dimensional reduction. In spherical coordinates, the problem of determining Green's function for the Helmholtz equation with separable boundary conditions can be reduced to a one-dimensional problem in r for which the construction of Green's function has been shown above. To achieve this dimensional reduction, we split the Laplace operator, cf. eq. (3.2), into $\Delta = \mathcal{L}_1(r, \frac{\partial}{\partial r}) + \frac{1}{r^2} \mathcal{L}_2(\phi, \theta, \frac{\partial}{\partial \phi}, \frac{\partial}{\partial \theta})$, where $\mathcal{L}_1 = \frac{1}{r^2} \frac{\partial}{\partial r} \left(r^2 \frac{\partial}{\partial r} \right)$ and $\mathcal{L}_2 = \frac{1}{\sin \theta} \frac{\partial}{\partial \theta} \left(\sin \theta \frac{\partial}{\partial \theta} \right) + \frac{1}{\sin^2 \theta} \frac{\partial^2}{\partial \phi^2}$. Green's function is uniquely defined by the inhomogeneous equation,

$$\left(\mathcal{L}_1 + \frac{1}{r^2} \mathcal{L}_2 + k^2 \right) G(\boldsymbol{r}, \boldsymbol{r_0}) = -\frac{1}{r^2 \sin \theta} \delta(r - r_0) \delta(\phi - \phi_0) \delta(\theta - \theta_0) \tag{A.10}$$

and a set of boundary conditions at the boundaries of the domain

$$\Omega := \left\{ \boldsymbol{r} \in \mathbb{R}^3 : r_1 \leq r \leq r_2, \phi_1 \leq \phi \leq \phi_2, \theta_1 \leq \theta \leq \theta_2, \right\}.$$

As shown in chapter 3, the homogeneous problem is solved by a product ansatz and any homogeneous solution can be expressed by the series expansion

$$p(\boldsymbol{r}) = \sum_{l=0}^{\infty} a_l Y_{\nu_l}^{\mu_l}(\boldsymbol{\theta}) R_{\nu_l}(r), \qquad (A.11)$$

where $Y_{\nu_l}^{\mu_l}(\boldsymbol{\theta})$ are the angular solutions fulfilling the prescribed boundary conditions at $\phi_{1,2}$, $\theta_{1,2}$, $R_{\nu_l}(r) = e_l\, j_{\nu_l}(kr) + f_l\, h_{\nu_l}^{(2)}(kr)$ are the general radial solutions, and a_l are the expansion coefficients. The coefficients e_l, f_l as well as the values of the wave number k are determined by the boundary conditions at $r_{1,2}$. Obviously, Green's function has to fulfill the homogeneous equation almost everywhere in Ω except for $\boldsymbol{r} = \boldsymbol{r_0}$. Hence we make the following ansatz for Green's function by analogy with eq. (A.11):

$$G(\boldsymbol{r},\boldsymbol{r_0}) = \sum_{l=0}^{\infty} a_l Y_{\nu_l}^{\mu_l}(\boldsymbol{\theta}) G_{R,\nu_l}(r,r_0). \qquad (A.12)$$

Inserting this in eq. (A.10) yields

$$\sum_{l=0}^{\infty} a_l \left(Y_{\nu_l}^{\mu_l}(\boldsymbol{\theta}) \left[\mathcal{L}_1 G_{R,\nu_l}(r,r_0) + k^2 G_{R,\nu_l}(r,r_0) \right] + G_{R,\nu_l}(r,r_0) \frac{1}{r^2} \mathcal{L}_2 Y_{\nu_l}^{\mu_l}(\boldsymbol{\theta}) \right) =$$
$$- \frac{1}{r^2 \sin\theta} \delta(r-r_0)\delta(\phi-\phi_0)\delta(\theta-\theta_0). \qquad (A.13)$$

Recalling the fact that $Y_{\nu_l}^{\mu_l}(\boldsymbol{\theta})$ are the eigenfunctions of $\mathcal{L}_2$ such that

$$\mathcal{L}_2 Y_{\nu_l}^{\mu_l}(\boldsymbol{\theta}) = -\nu_l(\nu_l+1) Y_{\nu_l}^{\mu_l}(\boldsymbol{\theta}),$$

and the completeness relation of the angular solutions in the form of

$$\sum_{l=0}^{\infty} Y_{\nu_l}^{\mu_l}(\boldsymbol{\theta}_0) Y_{\nu_l}^{\mu_l}(\boldsymbol{\theta}) = \frac{1}{\sin\theta} \delta(\phi-\phi_0)\delta(\theta-\theta_0),$$

eq. (A.13) is equivalent to

$$\sum_{l=0}^{\infty} a_l Y_{\nu_l}^{\mu_l}(\boldsymbol{\theta}) \left[\mathcal{L}_1 G_{R,\nu_l}(r,r_0) + \left(k^2 - \frac{\nu_l(\nu_l+1)}{r^2} \right) G_{R,\nu_l}(r,r_0) \right] =$$
$$- \frac{1}{r^2} \delta(r-r_0) \sum_{l=0}^{\infty} Y_{\nu_l}^{\mu_l}(\boldsymbol{\theta}_0) Y_{\nu_l}^{\mu_l}(\boldsymbol{\theta}). \qquad (A.14)$$

By multiplying both sides by $Y_{\nu_l}^{\mu_l}(\boldsymbol{\theta})$ and integrating $\int_{\phi_1}^{\phi_2} \int_{\theta_1}^{\theta_2} (\cdots) Y_{\nu_l}^{\mu_l}(\boldsymbol{\theta}) \sin\theta d\theta d\phi$, we end up with a set of one-dimensional problems:

$$a_l \left[\mathcal{L}_1 G_{R,\nu_l}(r,r_0) + \left(k^2 - \frac{\nu_l(\nu_l+1)}{r^2} \right) G_{R,\nu_l}(r,r_0) \right] = -\frac{1}{r^2} \delta(r-r_0) Y_{\nu_l}^{\mu_l}(\boldsymbol{\theta}_0). \quad \text{(A.15)}$$

Setting $a_l = Y_{\nu_l}^{\mu_l}(\boldsymbol{\theta}_0)$, and by multiplying both sides with r^2 the above equation simplifies to

$$\left[\frac{\partial}{\partial r} \left(r^2 \frac{\partial}{\partial r} \right) + k^2 r^2 - \nu_l(\nu_l+1) \right] G_{R,\nu_l}(r,r_0) = -\delta(r-r_0), \quad \text{(A.16)}$$

which is the spherical Bessel differential equation. Recalling the ansatz in eq. (A.12), Green's function for the Helmholtz equation is expressed by

$$G(\boldsymbol{r},\boldsymbol{r_0}) = \sum_{l=0}^{\infty} Y_{\nu_l}^{\mu_l}(\boldsymbol{\theta}_0) Y_{\nu_l}^{\mu_l}(\boldsymbol{\theta}) G_{R,\nu_l}(r,r_0), \quad \text{(A.17)}$$

where $G_{R,\nu_l}(r,r_0)$ is the Green's function of eq. (A.16) with the prescribed boundary conditions at r_1, r_2.

We are mainly interested in solutions fulling Sommerfeld's radiation condition and a sound-hard, sound-soft or singular boundary condition in r. Hence we look for a solution of eq. (A.16), fulfilling the radiation condition, i.e.

$$\lim_{r \to \infty} r \left(\frac{\partial}{\partial r} + ik \right) G_{R,\nu_l}(r,r_0) = 0, \quad \text{(A.18)}$$

and either a Dirichlet boundary condition, i.e. $G_{R,\nu_l}(r,r_0)|_{r=r_1} = 0$, or a Neumann boundary condition, i.e. $\left. \frac{\partial G_{R,\nu_l}(r,r_0)}{\partial} \right|_{r=r_1} = 0$. Note that for $r_1 \to 0$ the regular boundary condition becomes a singular one.

The homogeneous solution fulfilling the radiation condition is the spherical Hankel function of the second kind,

$$R_{\nu_l,2}(r) = h_{\nu_l}^{(2)}(kr). \quad \text{(A.19)}$$

From the general solution of the homogeneous Bessel differential equation, is easy to

see that following solution fulfill the considered boundary condition types at r_1:

$$R_{\nu_l,1}(r) = \begin{cases} j_{\nu_l}(kr) - \frac{j_{\nu_l}(kr_1)}{h^{(2)}_{\nu_l}(kr_1)} h^{(2)}_{\nu_l}(kr) & \text{for a Dirichlet B.C. at } r_1, \\ j_{\nu_l}(kr) - \frac{j'_{\nu_l}(kr_1)}{h'^{(2)}_{\nu_l}(kr_1)} h^{(2)}_{\nu_l}(kr) & \text{for a Neumann B.C. at } r_1, \\ j_{\nu_l}(kr) & \text{for a singular B.C. at } r_1 = 0. \end{cases}$$
(A.20)

The construction of $G_{R,\nu_l}(r,r_0)$ is carried out as derived in the previous paragraph. It turns out that for every $R_{\nu,1}(r)$ in eq. (A.20) and $R_{\nu,2}(r) = h^{(2)}_{\nu_l}(kr)$ holds

$$R_{\nu,1}(r)R'_{\nu,2}(r) - R'_{\nu,1}(r)R_{\nu,2}(r) = k\left(j_\nu(kr)h'^{(2)}_\nu(kr) - j'_\nu(kr)h^{(2)}_\nu(kr)\right) = -\frac{1}{ikr^2}$$
(A.21)

as $j_\nu(z)h'^{(2)}_\nu(z) - j'_\nu(z)h^{(2)}_\nu(z) = -\frac{1}{iz^2}$. Comparing eq. (A.16) to the general form in eq. (A.1) we have $p(r) = r^2$. Hence, inserting eqs. (A.19) and (A.20) in eq. (A.9) we get the following results for $G_{R,\nu_l}(r,r_0)$ for a radiating boundary condition and

- a Dirichlet boundary condition at r_1

$$G_{R,\nu_l}(r,r_0) = -ik \begin{cases} h^{(2)}_{\nu_l}(kr_0)\left(j_{\nu_l}(kr) - \frac{j_{\nu_l}(kr_1)}{h^{(2)}_{\nu_l}(kr_1)} h^{(2)}_{\nu_l}(kr)\right) & \text{for } r \leq r_0 \\ \left(j_{\nu_l}(kr_0) - \frac{j_{\nu_l}(kr_1)}{h^{(2)}_{\nu_l}(kr_1)} h^{(2)}_{\nu_l}(kr_0)\right) h^{(2)}_{\nu_l}(kr) & \text{for } r \geq r_0 \end{cases}$$
(A.22)

- a Neumann boundary condition at r_1

$$G_{R,\nu_l}(r,r_0) = -ik \begin{cases} h^{(2)}_{\nu_l}(kr_0)\left(j_{\nu_l}(kr) - \frac{j'_{\nu_l}(kr_1)}{h'^{(2)}_{\nu_l}(kr_1)} h^{(2)}_{\nu_l}(kr)\right) & \text{for } r \leq r_0 \\ \left(j_{\nu_l}(kr_0) - \frac{j'_{\nu_l}(kr_1)}{h'^{(2)}_{\nu_l}(kr_1)} h^{(2)}_{\nu_l}(kr_0)\right) h^{(2)}_{\nu_l}(kr) & \text{for } r \geq r_0 \end{cases}$$
(A.23)

- a singular boundary condition at $r_1 = 0$

$$G_{R,\nu_l}(r,r_0) = -ik \begin{cases} h^{(2)}_{\nu_l}(kr_0)\, j_{\nu_l}(kr) & \text{for } r \leq r_0, \\ j_{\nu_l}(kr_0)\, h^{(2)}_{\nu_l}(kr) & \text{for } r \geq r_0, \end{cases}$$
(A.24)

Finally, inserting one of eqs. (A.22) to (A.24) in eq. (A.17) yields Green's function of the Helmholtz equation for the respective boundary conditions.

Appendix B

Separation of the Helmholtz equation in spherical coordinates

Using the Laplace operator in spherical coordinates, cf. eq. (3.2), the homogeneous Helmholtz differential equation, cf. eq. (3.1),

$$\frac{\partial^2 p(\boldsymbol{r})}{\partial r^2} + \frac{2}{r}\frac{\partial p(\boldsymbol{r})}{\partial r} + \frac{\cos\theta}{r^2\sin\theta}\frac{\partial p(\boldsymbol{r})}{\partial\theta} + \frac{1}{r^2\sin^2\theta}\frac{\partial^2 p(\boldsymbol{r})}{\partial\theta^2} + \frac{1}{r^2\sin^2\theta}\frac{\partial^2 p(\boldsymbol{r})}{\partial\phi^2} + k^2 p(\boldsymbol{r}) = 0 \ .$$

Inserting the product ansatz, cf. eq. (3.3) yields

$$\Phi\Theta\frac{d^2 R}{dr^2} + \Phi\Theta\frac{2}{r}\frac{dR}{dr} + \frac{1}{r^2}R\Phi\frac{d^2\Theta}{d\theta^2} + \frac{\cos\theta}{r^2\sin\theta}R\Phi\frac{d\Theta}{d\theta} + \frac{R\Theta}{r^2\sin^2\theta}\frac{d^2\Phi}{d\phi^2} + k^2 + R\Phi\Theta = 0 \ \left| \ \cdot\frac{r^2}{R\Phi\Theta}\right. ,$$

$$\frac{r^2}{R}\frac{d^2 R}{dr^2} + \frac{2r}{R}\frac{dR}{dr} + \frac{1}{\Theta}\frac{d^2\Theta}{d\theta^2} + \frac{\cos\theta}{\sin\theta\,\Theta}\frac{d\Theta}{d\theta} + \frac{1}{\sin^2\theta\,\Phi}\frac{d^2\Phi}{d\phi^2} + k^2 r^2 = 0.$$

Arranging the terms depending on r on the left side and the terms depending on ϕ, θ on the right side of the equation, we can write

$$\frac{r^2}{R}\frac{d^2 R}{dr^2} + \frac{2r}{R}\frac{dR}{dr} + k^2 r^2 = -\frac{1}{\Theta}\frac{d^2\Theta}{d\theta^2} - \frac{\cos\theta}{\sin\theta\,\Theta}\frac{d\Theta}{d\theta} - \frac{1}{\sin^2\theta\,\Phi}\frac{d^2\Phi}{d\phi^2} = C_1,$$

where C_1 is a constant. The above equation splits up in two differential equations. The left side yields an ordinary differential equation in r,

$$\frac{r^2}{R}\frac{d^2 R}{dr^2} + \frac{2r}{R}\frac{dR}{dr} + k^2 r^2 = C_1.$$

For notational convenience we replace $C_1 = \nu(\nu + 1)$, rearrange the terms and get

$$r^2 \frac{d^2 R}{dr^2} + 2r \frac{dR}{dr} + k^2 r^2 R - \nu(\nu + 1)R = 0. \tag{B.1}$$

The right side yields a partial differential equation in ϕ, θ

$$-\frac{1}{\Theta} \frac{d^2 \Theta}{d\theta} - \frac{\cos\theta}{\sin\theta} \frac{d\Theta}{\Theta} \frac{d\Theta}{d\theta} - \frac{1}{\sin^2\theta} \frac{1}{\Phi} \frac{d^2\Phi}{d\phi^2} = \nu(\nu + 1).$$

Multiplying by $\sin^2\theta$ and rearranging the terms yields

$$\frac{\sin^2\theta}{\Theta} \frac{d^2\Theta}{d\theta} + \frac{\sin\theta\cos\theta}{\Theta} \frac{d\Theta}{d\theta} + \nu(\nu + 1)\sin^2\theta = -\frac{1}{\Phi} \frac{d^2\Phi}{d\phi^2} = C_2,$$

where C_2 is a constant. Thus the above equation splits up in two ordinary differential equations, one in θ and one in ϕ. The ordinary differential equation in θ is

$$\frac{\sin^2\theta}{\Theta} \frac{d^2\Theta}{d\theta} + \frac{\sin\theta\cos\theta}{\Theta} \frac{d\Theta}{d\theta} + \nu(\nu + 1)\sin^2\theta = C_2.$$

Dividing by $\sin^2\theta$, multiplying by Θ and setting $C_2 = \mu^2$ gives

$$\frac{d^2\Theta}{d\theta} + \frac{\cos\theta}{\sin\theta} \frac{d\Theta}{d\theta} - \frac{\mu^2}{\sin^2\theta}\Theta + \nu(\nu + 1)\Theta = 0. \tag{B.2}$$

Similarly, the ordinary differential equation in ϕ results in

$$\frac{d^2\Phi}{d\phi^2} + \mu^2\Phi = 0. \tag{B.3}$$

Appendix C

Solving the spherical Bessel differential equation

Equation (3.6) is equivalently expressed by

$$r^2 \frac{d^2 R}{dr^2} + 2r \frac{dR}{dr} + \left[k^2 r^2 - \nu(\nu + 1) \right] R = 0 \ . \tag{C.1}$$

Substituting $z = kr$, and thus $r \frac{dR}{dr} = kr \frac{dR}{d(kr)} = z \frac{dR}{dz}$, as well as $r^2 \frac{d^2 R}{dr^2} = z^2 \frac{d^2 R}{dz^2}$ yields

$$z^2 \frac{d^2 R}{dz^2} + 2z \frac{dR}{dz} + \left[z^2 - \nu(\nu + 1) \right] R = 0 \ . \tag{C.2}$$

Substituting $R(z) = z^{-\frac{1}{2}} S(z)$ for the solution transforms the equation above into the Bessel differential equation,

$$z^2 \frac{d^2 S}{dz^2} + z \frac{dS}{dz} + \left[z^2 - (\nu + \tfrac{1}{2})^2 \right] S = 0, \tag{C.3}$$

which can be solved using the Frobenius method, cf. [Kre99]. The solutions yield

$$J_\lambda(z) = z^\lambda \sum_{m=0}^{\infty} \frac{(-1)^m z^{2m}}{2^{2m+\lambda} \, m! \, \Gamma(\lambda + m + 1)} \ , \tag{C.4}$$

$$Y_\lambda(z) = \frac{J_\lambda(z) \cos \lambda\pi - J_{-\lambda}(z)}{\sin \lambda\pi} \ . \tag{C.5}$$

with $\lambda = \nu + \frac{1}{2}$. In the above equation, $J_\lambda(z)$, $Y_\lambda(z)$ are the Bessel functions of the first and second kind, respectively. If $\lambda = l \in \mathbb{N}$ the right hand side of eq. (C.5) is

replaced by its limiting value

$$Y_l(z) = \lim_{\lambda \to l} Y_\lambda(z) \,. \tag{C.6}$$

which yields, cf. [DLMF, §10.8],

$$Y_l(z) = -\frac{\left(\frac{1}{2}z\right)^{-l}}{\pi} \sum_{m=0}^{l-1} \frac{(l-m-1)!}{m!} \left(\frac{1}{4}z^2\right)^m +$$

$$\frac{2}{\pi} \ln\left(\frac{1}{2}z\right) J_l(z) - \frac{\left(\frac{1}{2}z\right)^l}{\pi} \sum_{m=0}^{\infty} [\psi(m+1) + \psi(l+m+1)] \frac{\left(-\frac{1}{4}z^2\right)^m}{m!\,(l+k)!}, \tag{C.7}$$

where $\psi(x) = \frac{\Gamma'(x)}{\Gamma(x)}$ is the digamma function.

The solutions of the spherical Bessel differential equation, eq. (3.6), are the result of back substitution,

$$j_\nu(kr) = \sqrt{\frac{\pi}{2kr}} \, J_{\nu+\frac{1}{2}}(kr) \,, \tag{C.8}$$

$$y_\nu(kr) = \sqrt{\frac{\pi}{2kr}} \, Y_{\nu+\frac{1}{2}}(kr) \,. \tag{C.9}$$

These functions are called spherical Bessel functions of the first and second kind whereby the term $\sqrt{\frac{\pi}{2}}$ is a convention.

Other standard solutions are the spherical Hankel functions of the first and second kind. These can be expressed as a linear combination of the spherical Bessel functions,

$$h_\nu^{(1)}(kr) = j_\nu(kr) + iy_\nu(kr) \,, \tag{C.10}$$

$$h_\nu^{(2)}(kr) = j_\nu(kr) - iy_\nu(kr) \,. \tag{C.11}$$

Similar to eqs. (C.8) and (C.9), the spherical Hankel functions are related to the Hankel functions by

$$h_\nu^{(1,2)}(kr) = \sqrt{\frac{\pi}{2kr}} \, H_{\nu+\frac{1}{2}}^{(1,2)}(kr). \tag{C.12}$$

Appendix D

Requirements for non-negative eigenvalues in Sturm-Liouville problems

Multiplying the Sturm-Liouville equation, see eq. (3.18), by $\bar{y}$, i.e. the complex conjugate of y, and integrating from a to b yields

$$\int_a^b \frac{d}{dx} \left[py'\right] \bar{y}dx + \int_a^b \left[\lambda w - q\right] y\bar{y}dx = 0.$$

Applying integration by parts to the first integral in the above equation we get

$$p(b)y'(b)\bar{y}(b) - p(a)y'(a)\bar{y}(a) - \int_a^b py'\bar{y}'dx + \int_a^b \left[\lambda w - q\right] y\bar{y}dx = 0.$$

With $y\bar{y} = |y|^2$ and some rearrangements we have

$$\lambda \int_a^b w|y|^2dx = \int_a^b p|y'|^2dx + \int_a^b q|y|^2dx - p(b)y'(b)\bar{y}(b) + p(a)y'(a)\bar{y}(a). \quad \text{(D.1)}$$

The integral on the left-hand side in the above equation is non-negative as $w(x) > 0$ for $x \in (a, b)$, cf. eq. (3.19); $\int_a^b p|y'|^2dx \geq 0$ follows from $p(x) > 0$ for $x \in (a, b)$, cf. eq. (3.19). If we assume that $q(x) \geq 0$ for $x \in (a, b)$ we have $\int_a^b q|y|^2dx \geq 0$. Obviously, for a solution $y_i(x)$ for which the following condition holds:

$$p(a)y_i'(a)\bar{y}_i(a) - p(b)y_i'(b)\bar{y}_i(b) \geq 0, \quad \text{(D.2)}$$

the associated eigenvalue λ_i is in either case non-negative. Note that as the eigenvalue and all integrals in eq. (D.1) are real-valued the term on the left side of the above inequality is clearly real-valued.

The behavior of y_i and its derivative at the endpoints a, b is determined by the boundary conditions of the problem. We will show in the following for different types of boundary conditions that eq. (D.2) holds for any solution of the problem if additional requirements are satisfied and thus no negative eigenvalues exist. Note that these are sufficient but not necessary conditions.

Periodic boundary conditions. In this case, cf. eq. (3.40), strict equality holds in eq. (D.2) for any solution. Hence the additional requirement for non-negative eigenvalues is simply $q(x) \geq 0$ for $x \in (a, b)$.

Separated boundary conditions. In this case both endpoints can be considered separately and thus eq. (D.2) can be split an inequality for each endpoint:

$$p(a)y'(a)\bar{y}(a) \geq 0, \tag{D.3}$$

$$p(b)y'(b)\bar{y}(b) \leq 0. \tag{D.4}$$

The inequality for each endpoint holds and $q(x) \geq 0$, for $x \in (a, b)$, no negative eigenvalues exist.

Regular endpoints. For a regular end point a we have a boundary condition of the form, cf. eq. (3.38),

$$\alpha_1 \, y(a) + \alpha_2 \, y'(a) = 0.$$

Multiplying by $\alpha_1 \, \bar{y}(a)$ and rearranging yields

$$\alpha_1 \alpha_2 \, y'(a)\bar{y}(a) = -\alpha_1^2 \, |y(a)|^2,$$

which implies the inequality

$$\alpha_1 \alpha_2 \, y'(a)\bar{y}(a) \leq 0.$$

This shows that $y'(a)\bar{y}(a) \geq 0$ when $\alpha_1 \alpha_2 < 0$. As α_1, α_2 are restricted to be not both zero, it follows for $\alpha_1 \alpha_2 = 0$ that either $y(a) = 0$ or $y'(a) = 0$ is required by the boundary condition; hence $y'(a)\bar{y}(a) = 0$. Finally, as $p(x) > 0$ for $x \in (a, b)$, eq. (D.3) holds for

$$\alpha_1 \alpha_2 \leq 0.$$

Similarly it can be shown that eq. (D.4) holds for

$$\beta_1 \beta_2 \geq 0.$$

LC end point with Friedrichs boundary condition. If either endpoint a or b is LC and we apply Friedrichs boundary condition, cf. eq. (3.44), we have

$$p(d)\left(y'(d)\bar{u}(d) - y(d)\bar{u}'(d)\right) = 0,$$

for either $d = a$ or $d = b$. Multiplying with $\bar{y}(d)$ and rearranging yields

$$p(d)y'(d)\bar{y}(d) = |y(d)|^2 \frac{p(d)\bar{u}'(d)}{\bar{u}(d)}.$$

As the left side of the above equation is real-valued it follows that the ratio $\frac{\bar{u}'(d)}{\bar{u}(d)}$ is real-valued and the complex conjugation is obsolete. If endpoint a is LC, we have $d = a$ in the above equation. As the squared absolute value is strictly non-negative, eq. (D.3) holds for

$$\frac{p(a)u'(a)}{u(a)} \geq 0.$$

Similarly, if endpoint b is LC eq. (D.4) holds for

$$\frac{p(b)u'(b)}{u(b)} \leq 0.$$

LP end points. If one or both of the endpoints a, b are LP then at these endpoints no boundary conditions are needed or allowed. Hence no addition requirements can be derived directly from boundary conditions for which all eigenvalues are non-negative.

However, Theorem 10.8.2 in [Zet05] states that in general the eigenvalues of a sequence of regular Sturm-Liouville problems on truncated intervals[1] converge to the eigenvalues of the singular problem if its series of eigenvalues is bounded below and discrete, i.e. $\sigma = \{\lambda_i : i \in \mathbb{N}_0\}$, $-\infty < \lambda_0 < \lambda_1 < \lambda_2 < \cdots$ The boundary condition applied to this series of regular problems are referred to as *inherited* boundary condition. Near a LP endpoint the inherited boundary condition is the *Dirichlet* condition, cf. [Zet05, Definition 10.8.1].

---

[1]Here the series of truncated intervals is (a_r, b_r), with $a < a_r < b_r < b$, $r \in \mathbb{N}$ and $a_r \to a$, $b_r \to b$ as $r \to \infty$.

If a is a regular endpoint with a *Dirichlet* boundary condition then $\alpha_1 = 0$ and eq. (D.3) holds. It follows that eq. (D.3) also holds if a is LP if σ is bounded below and discrete. Similarly, eq. (D.4) holds if b is LP σ is bounded below and discrete.

Thus it remains to investigate what the additional requirements are so that σ is bounded below and discrete in case of a LP endpoint. It shows that σ is bounded below if eq. (3.18) is non-oscillatory at a for some real λ_a and at b for some real λ_b when $p > 0$ for $x \in (a, b)$; this follows from Proposition 10.4.4. together with Theorem 10.5.1 in[Zet05].

An endpoint is called *oscillatory* if it is an accumulation point of zeros of a nontrivial solution. This only happens at a singular endpoint and then all solutions of the differential equation have infinitely many zeros in any right- respectively left-neighborhood of the endpoint, see [Zet05; BEZ01]. Note that for LP endpoints it depends on λ whether it is oscillatory or not, where for LC endpoints[2] this classification is independent of λ. There are several criteria to determine whether an endpoint is oscillatory or not, as Zettl states in his monograph:

> Many sufficient conditions are known for each of these classes (oscillatory and non-oscillatory), there are also some necessary and sufficient conditions known but there are no necessary and sufficient conditions known which can be checked for all equations. Improving known sufficient conditions and looking for checkable necessary and sufficient ones is today, 170 years after the appearance of the seminal paper of Sturm, still a very active field of research [Zet05, p. 133].

However, the endpoint a is non-oscillatory if and only if there exists a principal solution at a, [Zet05, Theorem 6.2.1]. So if endpoint a is LP and there exist a principal solution at a for some λ_a and endpoint b is either regular or LC, it follows that σ is bounded below. Similarly, σ is bounded below if endpoint b is LP and there exist a principal solution at b for some λ_b and endpoint a is either regular or LC, or in case of both endpoints are LP, if there exist a principal solution at a for some λ_a and a principal solution at b for some λ_b.

The eigenvalue spectrum σ may have a discrete part σ_d containing all isolated eigenvalues and continuous part σ_e, which also called the *essential* spectrum. The starting point of the continuous eigenvalue spectrum $\sigma_0 = \inf \sigma_e$ is as well the "oscillation point" of the equation. This means that for $\lambda > \sigma_0$ the equation is oscillatory and

---

[2]The LC classification is usually further subdivided into two sub-cases: limit-circle non-oscillatory (LCNO) and limit-circle oscillatory (LCO), see e.g. [Zet05]. Within the main part of this work we did not introduce these sub-cases and we tacitly assume that a LC endpoint is non-oscillatory.

for $\lambda < \sigma_0$ the equation is non-oscillatory. Hence, if the equation is non-oscillatory for all λ, i.e. $\sigma_0 = \infty$, the continuous spectrum is empty and the eigenvalues are discrete, i.e. $\sigma = \sigma_d$.

If endpoint a is LP and there exists a principal solution at a for all λ and endpoint b is either regular or LC, then the series of eigenvalues is discrete and bounded below and thus eq. (D.3) holds, as shown above. Similarly eq. (D.4) holds if endpoint b is LP and there exists a principal solution at b for all λ and endpoint b is either regular or LC. If both endpoints are LP, there exists a principal solution at a for all λ, and there exists a principal solution at b for all λ, then eqs. (D.3) and (D.4) hold.

Appendix E

Square integrability of Ferrers functions at the singularities

We investigate here which solutions of eq. (3.5) are square integrable on an interval containing one or both of the singularities at ± 1 depending on the values of the parameters ν, μ. Therefore we first proof the following theorem:

Theorem 1 *Let $f(x)$ be a bounded, continuous, real-valued function on the interval $x \in [a, b)$ with a singularity at $x = b$, and let $g(x)$ be a function that is asymptotic equivalent to $f(x)$ for $x \to b$, then $\int_a^b |f(x)|^2 dx < \infty$ if and only if $\int_c^b |g(x)|^2 dx < \infty$ for any $c \in [a, b)$.*

Proof. We assume that $f(x)$ is a bounded, continuous function on the interval $x \in [a, b)$ with a singularity at $x = b$. Furthermore we assume that $g(x)$ is asymptotically equivalent to $f(x)$ for $x \to b$, i.e.

$$f(x) \sim g(x) \Leftrightarrow \lim_{x \to b} \frac{f(x)}{g(x)} = 1.$$

As $\lim_{x \to b} f(x)^r = \left(\lim_{x \to b} f(x) \right)^r$ for any real number r provided that $\lim_{x \to b} f(x) \neq 0$, it follows that

$$\lim_{x \to b} \frac{f^2(x)}{g^2(x)} = 1.$$

From the formal definition of the limit we know that,

$$\left| \frac{f^2(x)}{g^2(x)} - 1 \right| < \epsilon,$$

121

for $0 < |x - b| < \delta$ where $\delta > 0$ and $\epsilon > 0$ are real numbers. Considering the sign of the term in the absolute value an rearranging the terms, the last inequality is identical to

$$(1 - \epsilon)g^2(x) < f^2(x) < (1 + \epsilon)g^2(x). \tag{E.1}$$

Without loss of generality, we assume that δ is small enough that $\epsilon < 1$ holds and there is a $c \in [a, b]$ such that $b - \delta < c < b$. As $f(x)$ is bounded and continuous for $x \in [a, b)$, it is obvious the integral $\int_a^b |f(x)|^2 dx = \int_a^c |f(x)|^2 dx + \int_c^b |f(x)|^2 dx$ converges if $\int_c^b |f(x)|^2 dx$ converges. Due to eq. (E.1) it follows from the integral comparison test that $\int_c^b |f(x)|^2 dx$ converges if and only if $\int_c^b |g(x)|^2 dx$ converges.

Behavior at singularities. The behavior of Ferrers functions at singularity $x = 1$ as $x \to 1$ from below is, see [DLMF, §14.8.(i); Olv74, p.186]

$$\mathsf{P}_\nu^\mu(x) \sim \frac{1}{\Gamma(1 - \mu)} \left(\frac{2}{1 - x}\right)^{\mu/2}, \qquad \mu \neq 1, 2, 3, \ldots, \tag{E.2}$$

$$\mathsf{P}_\nu^m(x) \sim (-1)^m \frac{(\nu - m + 1)_{2m}}{m!} \left(\frac{1 - x}{2}\right)^{m/2}, \quad m = 1, 2, 3, \ldots,$$
$$\nu \neq m - 1, m - 2, \ldots, -m, \tag{E.3}$$

$$\mathsf{Q}_\nu^\mu(x) \sim \frac{1}{2} \cos(\mu\pi) \, \Gamma(\mu) \left(\frac{2}{1 - x}\right)^{\mu/2}, \qquad \mu > 0,$$
$$\mu \neq \tfrac{1}{2}, \tfrac{3}{2}, \tfrac{5}{2}, \ldots, \tag{E.4}$$

$$\mathsf{Q}_\nu^\mu(x) \sim (-1)^{\mu+(1/2)} \frac{\pi \, \Gamma(\nu + \mu + 1)}{2 \, \Gamma(\mu + 1) \, \Gamma(\nu - \mu + 1)} \left(\frac{1 - x}{2}\right)^{\mu/2}, \qquad \mu = \tfrac{1}{2}, \tfrac{3}{2}, \tfrac{5}{2}, \ldots,$$
$$\nu \pm \mu \neq -1, -2, -3, \ldots, \tag{E.5}$$

$$\mathsf{Q}_\nu^{-\mu}(x) \sim \frac{\Gamma(\mu) \, \Gamma(\nu - \mu + 1)}{2 \, \Gamma(\nu + \mu + 1)} \left(\frac{2}{1 - x}\right)^{\mu/2}, \qquad \mu > 0$$
$$\nu \pm \mu \neq -1, -2, -3, \ldots \tag{E.6}$$

$$\mathsf{Q}_\nu(x) \sim \frac{1}{2}\ln\left(\frac{2}{1-x}\right), \qquad\qquad \nu \neq -1,-2,-3,\ldots \qquad\text{(E.7)}$$

Square integrability. Let us first consider an interval $[a,1]$ including the singularity at $x=1$. It follows from the first fundamental theorem of calculus that $\int_c^1 (1-x)^r dx < \infty$ for $r > -1$, since the indefinite integral yields

$$\int (1-x)^r dx = \begin{cases} -\frac{(1-x)^{r+1}}{r+1} & \text{for } r \in \mathbb{R}\backslash -1 \\ -\ln(1-x) & \text{for } r = -1 \end{cases}.$$

Keeping this in mind and applying theorem 1 to eqs. (E.2) to (E.6) it shows that

$$\int_a^1 |\,\mathsf{P}_\nu^\mu(x)\,|^2 dx < \infty \qquad \text{for } \mu < 1, \qquad\qquad\qquad\qquad \text{(E.8)}$$

$$\int_a^1 |\,\mathsf{P}_\nu^m(x)\,|^2 dx < \infty \qquad \text{for } m = 1,2,3,\ldots, \quad \nu \neq m-1, m-2, \ldots, -m, \quad \text{(E.9)}$$

$$\int_a^1 |\,\mathsf{Q}_\nu^\mu(x)\,|^2 dx < \infty \qquad \text{for } 0 < \mu < 1, \quad \mu \neq \tfrac{1}{2}, \qquad\qquad \text{(E.10)}$$

$$\int_a^1 |\,\mathsf{Q}_\nu^\mu(x)\,|^2 dx < \infty \qquad \text{for } \mu = \tfrac{1}{2}, \tfrac{3}{2}, \tfrac{5}{2}, \ldots, \quad \nu \pm \mu \neq -1,-2,-3,\ldots, \quad \text{(E.11)}$$

$$\int_a^1 |\,\mathsf{Q}_\nu^{-\mu}(x)\,|^2 dx < \infty \qquad \text{for } 0 < \mu < 1, \quad \nu \pm \mu \neq -1,-2,-3,\ldots \qquad \text{(E.12)}$$

Similarly, with the indefinite integral

$$\int \ln^2\left(\frac{2}{1-x}\right) dx = (x-1)\left(\ln^2\left(\frac{2}{1-x}\right) + 2\ln\left(\frac{2}{1-x}\right) + 2\right),$$

and the limit

$$\lim_{x\to 1}(x-1)\left(\ln^2\left(\frac{2}{1-x}\right) + 2\ln\left(\frac{2}{1-x}\right) + 2\right) = 0,$$

it shows that applying theorem 1 to eq. (E.7) yields

$$\int_a^1 |\,\mathsf{Q}_\nu(x)\,|^2 dx < \infty \qquad\qquad \text{for } \nu \neq -1,-2,-3,\ldots \qquad \text{(E.13)}$$

Restricting the parameter values by $m \geq 0$ and $\nu \geq -\frac{1}{2}$, cf. eqs. (3.7) and (3.8), it follows from eq. (E.8) that $\mathsf{P}_\nu^{-\mu}(x)$ is always square integrable. Furthermore, $\mathsf{P}_\nu^{-\mu}(x)$ and $\mathsf{P}_\nu^\mu(x)$ are linearly dependent for $\mu \in \mathbb{Z}$. For $\mu = \pm\frac{1}{2}, \pm\frac{3}{2}, \pm\frac{5}{2}, \ldots$ $\mathsf{P}_\nu^{-\mu}(x)$ and $\mathsf{Q}_\nu^\mu(x)$ are linearly dependent. This follows from their Wronskians, cf. [DLMF, §14.2(iv)]. Thus, if the endpoint a is LP, cf. table 3.2b, and hence $\mu \geq 1$, all square integrable solution on $[a,1]$ are scalar multiples of $\mathsf{P}_\nu^{-\mu}(x)$. Clearly, for $0 \leq \mu < 1$, i.e. a is LC, it follows from eqs. (E.8) to (E.12), eq. (E.13) and their Wronskians that there are two

linearly independent solutions which are square integrable on $[a, 1]$. This complies with the properties of LP and LC endpoints, see section 3.2.

Let us now consider an interval $[-1, b]$ containing the singularity at $x = -1$. The functions $\mathsf{P}_\nu^\mu(-x)$, $\mathsf{Q}_\nu^\mu(-x)$ are further solutions of eq. (3.5), cf. [DLMF, §14.2(ii)]. Obviously, integrating the square of these functions on $[-1, b]$ yields the same parameter restrictions as for integrating the square of $\mathsf{P}_\nu^\mu(x)$, $\mathsf{Q}_\nu^\mu(x)$ over $[a, 1]$, as shown above. Similarly as for the interval $[a, 1]$, it shows that $\mathsf{P}_\nu^{-\mu}(x)$ is the only linearly independent solution that is square integrable on $[-1, b]$ for $\mu \geq 1$,i.e. if b is LP.

Let us now consider the interval $[-1, 1]$ containing a singularity at both endpoints. From the Wronskian of $\mathsf{P}_\nu^\mu(x)$ and $\mathsf{P}_\nu^\mu(-x)$ it shows that these solutions are linearly dependent when $\mu - \nu = 0, -1, -2, \ldots$ The solution $\mathsf{P}_{\mu+l}^\mu(x)$, with $l = 0, 1, 2, 3, \ldots$, is square integrable on $[-1, 1]$ as it is square integrable on $[a, 1]$, $-1 < a < 1$, due to eq. (E.8), and it is linearly dependent to $\mathsf{P}_{\mu+l}^\mu(-x)$, which is square integrable on $[-1, b]$, $-1 < b < 1$. Furthermore, if the endpoints ± 1 are LP, i.e. $\mu \geq 1$, all square integrable solution on $[-1, 1]$ are scalar multiples of $\mathsf{P}_{\mu+l}^\mu(x)$.

Appendix F

Expression of the energy vector in terms of spherical harmonics coefficients

Expressing the energy vector $\boldsymbol{r}_\mathrm{E}$, cf. eq. (5.36), in terms of its x, y, and z component yields,

$$
\boldsymbol{r}_\mathrm{E} = \frac{1}{E} \begin{bmatrix} \int_{\mathbb{S}^2} \sin(\theta)\cos(\phi)|f(\boldsymbol{\theta})|^2 d\boldsymbol{\theta} \\ \int_{\mathbb{S}^2} \sin(\theta)\sin(\phi)|f(\boldsymbol{\theta})|^2 d\boldsymbol{\theta} \\ \int_{\mathbb{S}^2} \cos(\theta)|f(\boldsymbol{\theta})|^2 d\boldsymbol{\theta} \end{bmatrix} . \tag{F.1}
$$

The spherical harmonics coefficients of the squared source distribution are,

$$
f_{nm} = \int_{\mathbb{S}^2} |f(\boldsymbol{\theta})|^2 Y_n^m(\boldsymbol{\theta}) d\boldsymbol{\theta} \tag{F.2}
$$

where by the explicit expression of the spherical harmonics of order $n = 1$ is,

$$
Y_{1,1}(\boldsymbol{\theta}) = \sqrt{\frac{3}{4\pi}} \sin(\theta)\cos(\phi), \tag{F.3}
$$

$$
Y_{1,-1}(\boldsymbol{\theta}) = -\sqrt{\frac{3}{4\pi}} \sin(\theta)\sin(\phi), \tag{F.4}
$$

$$
Y_{1,0}(\boldsymbol{\theta}) = \sqrt{\frac{3}{4\pi}} \cos(\theta). \tag{F.5}
$$

Comparing this to the integrals in eq. (F.1) reveals that the components of $\boldsymbol{r}_\mathrm{E}$ can be expressed in terms of the first order spherical harmonics coefficients of $|f(\boldsymbol{\theta})|^2$:

$$\boldsymbol{r}_\mathrm{E} = \frac{1}{E}\sqrt{\frac{4\pi}{3}}\begin{bmatrix} f_{1,1} \\ -f_{1,-1} \\ f_{1,0} \end{bmatrix}. \tag{F.6}$$

Assuming a spatially band-limited source distribution, i.e.

$$f(\boldsymbol{\theta}) = \sum_{n=0}^{N}\sum_{m=-n}^{n}\phi_{nm}Y_n^m(\boldsymbol{\theta}), \tag{F.7}$$

its squared absolute value yields

$$|f(\boldsymbol{\theta})|^2 = f(\boldsymbol{\theta})\bar{f}(\boldsymbol{\theta}) = \sum_{n'=0}^{N}\sum_{m'=-n'}^{n'}\sum_{n''=0}^{N}\sum_{m''=-n''}^{n''}\phi_{n'm'}\bar{\phi}_{n''m''}Y_{n'}^{m'}(\boldsymbol{\theta})Y_{n''}^{m''}(\boldsymbol{\theta}), \tag{F.8}$$

where the bar denotes the complex-conjugate. Inserting this in eq. (F.2) yields

$$f_{nm} = \sum_{n'=0}^{N}\sum_{m'=-n'}^{n}\sum_{n''=0}^{N}\sum_{m''=-n''}^{n''}\phi_{n'm'}\bar{\phi}_{n''m''}G_{nn'n''}^{mm'm''}, \tag{F.9}$$

whereby $G_{nn'n''}^{mm'm''}$ denotes the integral over three spherical harmonics and is referred to as Gaunt coefficient,

$$G_{nn'n''}^{mm'm''} := \int_{\mathbb{S}^2} Y_n^m(\boldsymbol{\theta})Y_{n'}^{m'}(\boldsymbol{\theta})Y_{n''}^{m''}(\boldsymbol{\theta})d\boldsymbol{\theta}. \tag{F.10}$$

Equation (F.9) can be equivalently expressed by the matrix product,

$$f_{nm} = \boldsymbol{\phi}_\mathrm{N}^\mathrm{H}\,\boldsymbol{G}_{nm,\mathrm{N}}\,\boldsymbol{\phi}_\mathrm{N}. \tag{F.11}$$

whereby $\boldsymbol{\phi}_\mathrm{N} = [\phi_{00},\ldots,\phi_{nm},\ldots,\phi_{\mathrm{NN}}]^\mathrm{T}$ is a vector containing the spherical harmonics coefficients of the source distribution, the superscript $^\mathrm{H}$ denotes Hermitian transpose, and $\boldsymbol{G}_{nm,\mathrm{N}}$ is a matrix containing Gaunt coefficients $G_{n,n',n''}^{m,m',m''}$,

$$\boldsymbol{G}_{nm,\mathrm{N}} = \begin{bmatrix} G_{n,0,0}^{m,0,0}, & \cdots, & G_{n,0,\mathrm{N}}^{m,0,\mathrm{N}} \\ \vdots & \ddots & \vdots \\ G_{n,\mathrm{N},0}^{m,\mathrm{N},0}, & \cdots, & G_{n,\mathrm{N},\mathrm{N}}^{m,\mathrm{N},\mathrm{N}} \end{bmatrix}. \tag{F.12}$$

Inserting eq. (F.11) in eq. (F.6) and with $E = \int_{\mathbb{S}^2}|f(\boldsymbol{\theta})|^2d\boldsymbol{\theta} = \boldsymbol{\phi}_\mathrm{N}^\mathrm{H}\boldsymbol{\phi}_\mathrm{N}$ resulting from

the Parseval's relation, the energy vector for a source distribution $f(\boldsymbol{\theta})$ is expressed in terms of its spherical harmonics coefficients by

$$
\boldsymbol{r}_{\mathrm{E}} = \frac{\sqrt{4\pi}}{\sqrt{3}\,\boldsymbol{\phi}_{\mathrm{N}}^{\mathrm{H}}\boldsymbol{\phi}_{\mathrm{N}}}
\begin{bmatrix}
\boldsymbol{\phi}_{\mathrm{N}}^{\mathrm{H}}\,\boldsymbol{G}_{1,1,\mathrm{N}}\,\boldsymbol{\phi}_{\mathrm{N}} \\
-\boldsymbol{\phi}_{\mathrm{N}}^{\mathrm{H}}\,\boldsymbol{G}_{1,-1,\mathrm{N}}\,\boldsymbol{\phi}_{\mathrm{N}} \\
\boldsymbol{\phi}_{\mathrm{N}}^{\mathrm{H}}\,\boldsymbol{G}_{1,0,\mathrm{N}}\,\boldsymbol{\phi}_{\mathrm{N}}
\end{bmatrix}. \tag{F.13}
$$

Bibliography

[AlG08]   M. A. Al-Gwaiz, *Sturm-Liouville Theory and its Applications*. Berlin: Springer, 2008.

[Bau86]   H. F. Bauer, "Tables of the roots of the associated Legendre function with respect to the degree", *Mathematics of computation*, vol. 46, no. 174, pp. 601–602, 1986.

[BEZ01]   P. B. Bailey, W. N. Everitt, and A. Zettl, "Algorithm 810: The SLEIGN2 Sturm-Liouville code", *ACM Transactions on Mathematical Software (TOMS)*, vol. 27, no. 2, pp. 143–192, 2001.

[BHL10]   E. Benjamin, A. Heller, and R. Lee, "Design of Ambisonic decoders for irregular arrays of loudspeakers by non-linear optimization", in *Papers of the 129th AES Convention*, San Francisco, 2010.

[BPF11]   R. Baumgartner, H. Pomberger, and M. Frank, "Practical implementation of radial filters for ambisonic recordings", in *Proceedings of the International Conference on Spatial Audio, ICSA*, Detmold, 2011.

[BPSW11]   B. Bernschütz, C. Pörschmann, S. Spors, and S. Weinzierl, "Soft-Limiting der modalen Amplitudenverstärkung bei sphärischen Mikrofonarrays im Plane Wave Decomposition Verfahren", in *Fortschritte der Akustik, DAGA, Düsseldorf*, 2011.

[BSMM07]   I. N. Bronshtein, K. A. Semendyayev, G. Musiol, and H. Mühlig, *Handbook of Mathematics*, 5th ed. Springer-Verlag, 2007.

[CH24]   R. Courant and D. Hilbert, *Methoden der mathematischen Physik*. Berlin: Springer, 1924.

[CK13]   D. Colton and R. Kress, *Inverse Acoustic and Electromagnetic Scattering Theory.* New York: Springer, 2013.

[CL55]   E. A. Coddington and N. Levinson, *Theory of Ordinary Differential Equations.* New Delhi: Tata McGraw-Hill, 1955.

[CWY11]   X. Chen, R. Womersley, and J. Ye, "Minimizing the condition number of a gram matrix", *SIAM Journal on Optimization*, vol. 21, no. 1, p. 127, 2011.

[Dav03]   M. F. Davis, "History of spatial coding", *Journal of the Audio Engineering Society*, vol. 51, no. 6, pp. 554–569, 2003.

[DLMF]   *NIST Digital Library of Mathematical Functions*, URL: `http://dlmf.nist.gov/`, Release 1.0.16 of 2017-09-18, F. W. J. Olver, A. B. Olde Daalhuis, D. W. Lozier, B. I. Schneider, R. F. Boisvert, C. W. Clark, B. R. Miller and B. V. Saunders, eds.

[EJZ14]   N. Epain, C. Jin, and F. Zotter, "Ambisonic decoding with constant angular spread", *Acta Acustica united with Acustica*, vol. 100, no. 5, pp. 928–936, 2014.

[EMO+53]   A. Erdélyi, W. Magnus, F. Oberhettinger, F. Tricomi, *et al.*, *Higher Transcendental Functions*, A. Erdélyi, Ed. New York: McGraw-Hill, 1953, vol. 1.

[Eve05]   W. Everitt, "A catalogue of Sturm-Liouville differential equations", in *Sturm-Liouville Theory: Past and Present.* Birkhäuser Verlag, 2005, pp. 271–331.

[Far00]   A. Farina, "Simultaneous measurement of impulse response and distortion with a swept-sine technique", in *Papers of the 108th AES Convention*, Paris, 2000.

[Fel75]   P. Fellgett, "Ambisonics. part one: General system description", *Studio Sound*, vol. 17, no. 8, pp. 20–22, 1975.

[Fra14]   M. Frank, "Localization using different amplitude-panning methods in the frontal horizontal plane", in *Proceedings of the EAA Joint Symposium on Auralization and Ambisonics*, Berlin, 2014.

[Fri36]   K. Friedrichs, "Über die ausgezeichnete Randbedingung in der Spektraltheorie der halbbeschränkten gewöhnlichen Differentialoperatoren zweiter Ordnung", *Mathematische Annalen*, vol. 112, no. 1, pp. 1–23, 1936.

[Gau29]   J. Gaunt, "The triplets of helium", *Philosophical Transactions of the Royal Society of London. Series A, Containing Papers of a Mathematical or Physical Character*, vol. 228, pp. 151–196, 1929.

[Ger73]   M. A. Gerzon, "Periphony: With-height sound reproduction", *Journal of the Audio Engineering Society*, vol. 21, no. 1, pp. 2–10, 1973.

[Ger92]   ——, "General metatheory of auditory localisation", in *Papers of the 92nd AES Convention*, Vienna, 1992.

[GV96]   G. H. Golub and C. F. Van Loan, *Matrix Computations*, 3rd ed. Baltimore: Johns Hopkins University Press, 1996.

[Hai85]   G. Haines, "Spherical cap harmonic analysis", *Journal of Geophysical Research*, vol. 90, no. B3, pp. 2583–2591, 1985.

[HC97]   C. Hwang and S. Chen, "Fully normalized spherical cap harmonics: Application to the analysis of sea-level data from TOPEX/POSEIDON and ERS-1", *Geophysical Journal International*, vol. 129, no. 2, pp. 450–460, 1997.

[JT65]   M. Junger and W. Thompson Jr, "Fresnel-zone and plane-wave impedances on very large pistons", *The Journal of the Acoustical Society of America*, vol. 38, p. 1059, 1965.

[Kel15]   B.-D. Keller, "Development of a sound projection prototype", Master's Thesis, University of Music and Performing Arts Graz, 2015. [Online]. Available: `http://phaidra.kug.ac.at/o:12802`.

[Köß11]   T. Kößler, "Microphone array on a spherical cap for three dimensional recordings of the wave field", Master's thesis, University of Music and Performing Arts Graz, 2011. [Online]. Available: `http://phaidra.kug.ac.at/detail_object/o:2312`.

[KR09]   A. Koretz and B. Rafaely, "Dolph–Chebyshev beampattern design for spherical arrays", *IEEE Transactions on Signal Processing*, vol. 57, no. 6, pp. 2417–2420, 2009.

[Kre99]   E. Kreyszig, *Advanced Engineering Mathematics*, 10th ed. John Wiley & Sons, 1999.

[KZ15]   B.-D. Keller and F. Zotter, "A new prototype for sound projection", in *Fortschritte der Akustik, DAGA, Nürnberg*, 2015.

[LD05]   Z. Li and R. Duraiswami, "Hemispherical microphone arrays for sound capture and beamforming", in *Proceedings of the IEEE Workshop on Applications of Signal Processing to Audio and Acoustics*, 2005, pp. 106–109.

[Lös14]   S. Lösler, "MIMO-Rekursivfilter für Kugelarrays", Master's Thesis, University of Music and Performing Arts Graz, 2014. [Online]. Available: `http://phaidra.kug.ac.at/o:8462`.

[LS75]   A. G. Law and M. Sledd, "Normalizing orthogonal polynomials by using their recurrence coefficients", *Proceedings of the American Mathematical Society*, vol. 48, no. 2, pp. 505–507, 1975.

[ME02]   J. Meyer and G. Elko, "A highly scalable spherical microphone array based on an orthonormal decomposition of the soundfield", in *Proceedings of the IEEE International Conference on Acoustics, Speech, and Signal Processing (ICASSP)*, 2002.

[Mec09]   F. Mechel, "Kanal-Mündungen, Teil II: Rund-Kanäle", *Acta acustica united with Acustica*, vol. 95, no. 2, pp. 203–233, 2009.

[Mey00]   C. Meyer, *Matrix Analysis and Applied Linear Algebra Book and Solutions Manual.* Siam, 2000, vol. 2.

[MF53]   P. Morse and H. Feshbach, *Methods of Theoretical Physics*. McGraw-Hill, 1953.

[Mös09]   M. Möser, *Technische Akustik*, 6th ed. Springer, 2009.

[MOS66]   W. Magnus, F. Oberhettinger, and R. P. Soni, *Formulas and Theorems for the Special Functions of Mathematical Physics*, 3rd ed. Berlin: Springer, 1966.

[MP95]   M. Marletta and J. D. Pryce, "LCNO Sturm-Liouville problems: Computational difficulties and examples", *Numerische Mathematik*, vol. 69, no. 3, pp. 303–320, 1995.

[MW10]   D. Moore and J. Wakefield, "A design tool to produce optimized Ambisonic decoders", in *Procceedings of the Audio Engineering Society Conference: 40th International Conference: Spatial Audio: Sense the Sound of Space*, 2010.

[Nai68]   M. A. Naimark, *Linear Differential Operators - Part II*. George G. Harrap & Co, 1968.

[Olv74]   F. W. J. Olver, *Asymptotics and Special Functions*. Academic Press, 1974.

[Pau13]   F. Pausch, "A rigid double cone microphone array prototype", Master's Thesis, University of Music and Performing Arts Graz, 2013. [Online]. Available: `http://phaidra.kug.ac.at/o:11147`.

[PB87]   T. W. Parks and C. S. Burrus, *Digital Filter Design*. Wiley-Interscience, 1987.

[Ple09]   P. Plessas, "Rigid sphere microphone arrays for spatial recording and holography", Master's Thesis, University of Musik and Performing Arts, 2009. [Online]. Available: `http://phaidra.kug.ac.at/o:11130`.

[Pom08]   H. Pomberger, "Angular and radial directivity control for spherical loudspeaker arrays", Master's Thesis, University of Music and Performing Arts, 2008. [Online]. Available: `http://phaidra.kug.ac.at/o:11036`.

[PP14]   H. Pomberger and F. Pausch, "Design and evaluation of a spherical segment array with double cone", *Acta Acustica united with Acustica*, vol. 100, no. 5, pp. 921–927, 2014.

[PSB+16]   H. Pomberger, A. Sontacchi, M. Brandner, M. Resch, S. Brandl, and R. Höldrich, "Free-field pressure-based sound power measurement procedure with low spatial-sampling-and-near-field-induced uncertainty", in *Proceedings of INTER-NOISE*, 2016.

[Pul97]   V. Pulkki, "Virtual sound source positioning using vector base amplitude panning", *Journal of the Audio Engineering Society*, vol. 45, no. 6, pp. 456–466, 1997.

[PZ17]   H. Pomberger and F. Zotter, "Converting hemispherical microphone array recordings", in *Fortschritte der Akustik, DAGA*, Kiel, 2017.

[PZS09]   H. Pomberger, F. Zotter, and A. Sontacchi, "An Ambisonics format for flexible playback layouts", in *Proceedings of the 1st Ambisonics Symposium*, Graz, 2009.

[Rab72]   A. Rabenstein, *Introduction to Ordinary Differential Equations*, 2nd ed. Academic Press, 1972.

[Raf04]   B. Rafaely, "Plane-wave decomposition of the sound field on a sphere by spherical convolution", *The Journal of the Acoustical Society of America*, vol. 116, no. 4, pp. 2149–2157, 2004.

[Raf05]   B. Rafaely, "Analysis and design of spherical microphone arrays", *IEEE Transactions on Speech and Audio Processing*, vol. 13, no. 1, pp. 135–143, 2005.

[Rel50]   F. Rellich, "Halbbeschränkte gewöhnliche Differentialoperatoren zweiter Ordnung", *Mathematische Annalen*, vol. 122, no. 5, pp. 343–368, 1950.

[RWB07]   B. Rafaely, B. Weiss, and E. Bachmat, "Spatial aliasing in spherical microphone arrays", *Signal Processing, IEEE Transactions on*, vol. 55, no. 3, pp. 1003–1010, 2007.

[Séb98] D. Sébilleau, "On the computation of the integrated products of three spherical harmonics", *Journal of Physics A: Mathematical and General*, vol. 31, no. 34, p. 7157, 1998.

[Smy50] W. R. Smythe, *Static and Dynamic Electricity*, 2nd ed. McGraw-Hill, 1950.

[Som49] A. Sommerfeld, *Partial Differential Equations in Physics*. Academic Press, 1949, vol. 1.

[SYS+10] H. Sun, S. Yan, U. P. Svensson, A. Solvang, and J. L. Nielsen, "Achievable maximum-directivity beamforming for spherical microphone arrays with random array errors", in *Proceedings of the 18th European Signal Processing Conference*, IEEE, Aalborg, 2010, pp. 1929–1933.

[SYS11] H. Sun, S. Yan, and U. P. Svensson, "Robust minimum sidelobe beamforming for spherical microphone arrays", *IEEE Transactions on Audio, Speech, and Language Processing*, vol. 19, no. 4, pp. 1045–1051, 2011.

[Van07] J. Van Diejen, "Remarks on the zeros of the associated Legendre functions with integral degree", *Acta Applicandae Mathematicae*, vol. 99, no. 3, pp. 293–299, 2007.

[Vis17] *VisiSonics Digital Array Microphones (VDAM)*, URL: `http://visisonics.com`. (visited on 08/31/2017).

[WA01] D. B. Ward and T. D. Abhayapala, "Reproduction of a plane-wave sound field using an array of loudspeakers", *IEEE Transactions on Speech and Audio Processing*, vol. 9, no. 6, pp. 697–707, 2001.

[WA03] H. Weber and G. Arfken, *Essential Mathematical Methods for Physicists*. Academic Press, 2003.

[Wik17] *Coordinate surfaces for spherical coordinates*, URL: `http://upload.wikimedia.org/wikipedia/commons/a/ad/Spherical_coordinate_surfaces.png`. (visited on 09/21/2017).

[Wil99] E. Williams, *Fourier Acoustics*. Academic Press, 1999.

[YZ13]   J. J. Ye and J. Zhou, "Minimizing the condition number to construct design points for polynomial regression models", *SIAM Journal on Optimization*, vol. 23, no. 1, pp. 666–686, 2013.

[Zet05]   A. Zettl, *Sturm-Liouville Theory*. American Mathematical Society, 2005.

[ZF12]   F. Zotter and M. Frank, "All-round Ambisonic panning and decoding", *Journal of the Audio Engineering Society*, vol. 60, no. 10, pp. 807–820, 2012.

[ZFP13]   F. Zotter, M. Frank, and H. Pomberger, "Comparison of energy-preserving and all-round ambisonic decoders", in *Fortschritte der Akustik, AIA-DAGA*, Meran, 2013.

[Zot09a]   F. Zotter, "Analysis and Synthesis of Sound-Radiation with Spherical Arrays", PhD thesis, University of Music and Performing Arts Graz, 2009. [Online]. Available: `http://phaidra.kug.ac.at/o:5619`.

[Zot09b]   ——, "Sampling strategies for acoustic holography/holophony on the sphere", in *Fortschritte der Akustik, NAG-DAGA*, Rotterdam, 2009.

[ZP12]   F. Zotter and H. Pomberger, "Spherical Slepian functions for approximation of spherical measurement data", in *Fortschritte der Akustik, DAGA*, Darmstadt, 2012.

[ZPF09]   F. Zotter, H. Pomberger, and M. Frank, "An alternative Ambisonics formulation: Modal source strength matching and the effect of spatial aliasing", in *Papers of the 126th AES Convention*, Munich, 2009.

[ZPN12]   F. Zotter, H. Pomberger, and M. Noisternig, "Energy-preserving Ambisonic decoding", *Acta Acustica united with Acustica*, vol. 98, no. 1, pp. 37–47, 2012.